BASIC PROPERTIES AND APPLICATIONS OF THE PARTICLE MODEL IN THE PLASMA SIMULATION(Dissertation_全文)

AUTHOR(S):

Abe, Hirotada

BASIC PROPERTIES AND APPLICATIONS OF THE PARTICLE MODEL IN THE PLASMA SIMULATION

Hirotada Abe

June 1976

Department of Electronics

Kyoto University, Kyoto, Japan

BASIC PROPERTIES AND APPLICATIONS OF THE PARTICLE MODEL IN THE PLASMA SIMULATION

Hirotada Abe

June 1976

Department of Electronics

Kyoto University, Kyoto, Japan

CONTENTS

CHAPTER 3 GRID EFFECTS ON THE PLASMA SIMULATION BY THE FINITE-SIZED PARTICLE · · · · · · · · · 29

3.1 Introduction · · · · · · · · ·

ABSTRACT

This thesis is devoted to the analyses of the basic, physical and computational properties of the plasma simulation using the particle model (sometimes called the "particle simulation") and to applications of it to the studies of two types of the plasma confinements: (1) the HIPAC and (2) an open ended system with the r. f. plugging.

At the beginning of Chapter 1, it is explained that the plasma simulations have played an indispensable role in plasma physics and the particle simulation is an important branch of plasma simulations. Next, the computational problems concerning the particle simulation are explained, and some of them studied in this thesis are mentioned. Furthermore, simple histories and some problems are mentioned concerning the HIPAC and the open ended system with the r. f. plugging.

In Chapter 2, the basic equations of the system composed of the finite-sized particle which is the basic conception of the particle simulation are explained. Here, the collisional effects in the 2-species plasmas of the finite-sized particles are studied by the numerical calculation. The calculation shows the enhancement of the collisional effects in a test cloud with the ion sound wave velocity, which cannot be found in the electron plasma of the finite-sized particles.

In Chapter 3, it is explained how the basic equations of the system explained in Chapter 2 are approximated by the use of the electronic, digital computers. Next it is pointed out that the conservation law of total energy is violated by the spatial grids which are introduced when the basic equations are approximated by the computers. Here, a scaling law concerning the accuracy of the conservation of total energy is derived. As a result, it depends on the number of particles in the Debye sphere, the number of spatial grids in the system, model, and so on. This scaling law is confirmed experimentally.

In Chapter 4, the particle simulation is applied in order to study the HIPAC which contains the unneutral electron clouds by the toroidal magnetic field and conducting toroidal vessels. The simulation results indicate that the HIPAC is promising for the containment of the electron clouds.

In Chapter 5, the r. f. plugging and heating of plasmas in the open ended system are studied by the use of the particle simulation. The results of simulation show that ion is well

heated up by applying the r. f. electric field with a frequency of ion cyclotron resonance and that the energy containment time is improved slightly.

At the beginning of Chapter 6, the main results of this thesis are summarized. Next, the problems left in this thesis and the future developments of investigations of the author and his colleagues are mentioned.

CHAPTER 1

INTRODUCTION

1.1 Situation of computer simulation in plasma physics

With the recent progress of electronic digital computers and computational techniques, computer simulations in plasma physics have been developed to be an important weapon for understanding plasma physics and become to compare with experiments and theories. New knowledges which have been discovered in the experimental and theoretical works have been reproduced and verified in the computer simulations, showing various detailed physical quantities, which have been difficult to measure in experiments. New phenomena have been discovered in computer simulations, too. Now it can be said that computer simulations have an indispensable role to play in plasma physics than in any other branch of physics. As pointed out [1], the reasons are the followings:

(1) The dynamical equations of plasma physics are simple to write down, because they are essentially the Maxwell equations for electromagnetic variables and classical equations of motion for the mechanical variables.

(2) These dynamical equations are impossible to solve analytically, because they are highly nonlinear and involve infinite numbers of degrees of freedom.

(3) The gross macroscopic behavior of a plasma exhibits a wealth of regularities and collective modes of motion which are often recognizable from numerical data, though they are difficult or impossible to prove analytically in a satisfying way.

In addition to these three points, we should indicate the one more important reason:

(4) In experiments, microscopic behaviors of plasma such as particle orbits in phase space are difficult to measure, but very easy in the computer simulation. This has brought about the deeper understanding for the plasma physics and impressed us for an aspect of the plasma as the many-particle system.

The applications of numerical analysis to plasma physics divide themselves rather naturally into two substantially different formulations: they are called the fluid simulation and the particle simulation. In the fluid simulation, the differential equations that describe the plasma state are solved by computers for appropriate boundary and initial conditions. In the particle simulation, the dynamics of discrete charged mass (in one, two, or three dimensions) are followed by solving the individual particle equations of motion. The fields are regularly recalculated from the particle positions and velocities, and the system evolves selfconsistently. This thesis is concerned with the particle simulation.

By the use of one of the fluid simulations in which the MHD equation is adopted to describe the plasma state, realistic calculations on the dynamics of cylindrical plasma devices showed good agreement with experiments for the θ-pinch [2]. These fluid simulations are developing today.

The particle simulation was first used to investigate the basic properties of electrostatic effects such as plasma oscillations, the kinetics, and the two-stream instability in the one-dimensional model [3–7]. Concerning the two-stream instability, the simulation results were compared between runs with three models (the 1-, 2-, and 3-dimensional electrostatic model) [8]. In all runs, the field energy rose unstably until saturation, at first exponentially at the rate of the fastest linear mode and the particle distribution in phase space showed the formation, coalescing, and long-time persistence of BGK modes or phase space eddies. However, these eddies coalesced considerably faster in runs with the 3- and 2-dimensional models than in those with the 1-dimensional models. Although the existence of the phase space eddies had been predicted in a theory [9], they were not observed in experiments because of the difficulty of measurements.

More recently, particle simulations have been used to study the transport of plasma across a fixed external magnetic field B [10]. It is well known that for plasma in local thermal equilibrium the diffusion coefficient is proportional to $1/B^2$ (the classical diffusion). However, experiments have often shown a much larger anomalous diffusion, whose empirical coefficient is proportional to $1/B$ (the Bohm diffusion [11]). The simulations have shown that there is a classical region, a Bohm region, and an intermediate region between these two where the diffusion rate is almost independent of B and suggested that the origin of the enhanced diffusion is due to the convective cells which are thermally excited. On the basis of the simulation results, a theory is constructed [10]. The theory was also confirmed by the experiments [12].

The simulations mentioned above have treated the infinite space where the periodic bound-

ary condition is assumed. On the other hand, there has been other type of simulation treating the confined plasmas in which the finite boundary condition is assumed. The electrostatic and magnetostatic simulations have been used to study the plasma confinement in a stellerator [13] and to study the instabilities of the rotational, tearing, mirror, and fire hose modes in the θ-pinch [14], respectively. Recently the fully electromagnetic, relativistic particle simulations of large scale [15] have been carried out to study the behaviors of the relativistic electron layer in the Astron. Throughout this study, there existed the feedbacks among the computational, theoretical, and experimental groups. As an example, considerable theoretical works were later done on a behavior of the electron layer, but this was not even recognized as a problem until it was uncovered by the simulation results.

As mentioned above, the particle simulations have been used not only for the basic problems treating the uniform space with the periodic boundary but also for those of the plasma confinements, which are studied in this thesis and presented in Chapters 4 and 5.

1.2 An origin of the finite-sized particle model

If we were possible to use an ideal computer with the infinitely large memory and fast computing speed, we would easily reproduce all of the electric and magnetic interactions of real plasmas using the particle simulation. Even in the up-to-date or the future computer, however, a complete simulation would run into the obvious difficulty of processing anywhere near the number of ions and electrons in the plasma. Hence, we use a reduced number of particles each with a larger charge and mass than the real particle; this results in increasing the fluctuations about the mean value (for example, of density, $n^{1/2}$) or the particle noise (quite accurately called "shot noise"). The shot noise can easily be so large as to mask the desired simulation.

Computationally, we can reduce the effects of the shot noise by increasing the number of particles. These improvements have been made in one-dimensional simulations, are being pushed in two dimensions, and are presently impracticably in three. When we perform the particle simulation actually, we are usually stuck with the physics of, and noise due to, too few particles; hence, analysis of the properties of the shot noise and developments of suitable means for noise reductions have been pushed forward energetically.

Physically, electrons and ions are point particles for most of plasma physics. Some interparticle interactions occur at short range in short times, producing effects at short wavelengths and high frequencies; fortunately, the important effects are the collective, long range,

interactions which produce wavelengths much larger than interparticle spacings and frequencies with periods much longer than particle crossing times. Such physics suggests introducing some form of smoothing of the forces at short range. From the above computational and physical requirements, the concept of the use of the 'finite-sized particle' was introduced and advocated by Birdsall and Fuss [16], and Dawson *et al.* [17].

1.3 Basic properties of the finite-sized particle plasma

Their approach to smoothing the interactions is to alter the structure of the real particles. These extended particles have a spread-out charge distribution and move rigidly without rotation or internal change but pass freely through one another. It seems natural to call these particles "finite-sized particles" or "clouds" [16, 17, 18]. The interaction of the system of the finite-sized particles is a straightforward generalization of the point particle interaction; in fact, certain divergences in the kinetic theory and in classical electromagnetic theory are removed [19, 20]. Namely, the charge density of a finite-sized particle whose center is at the origin is changed from $e\delta(x)$ to $eS(x)$ where e is the total charge. The function S is called the "shape factor" [19, 20].

On the basis of the above considerations, Birdsall, Langdon, and Okuda [19, 20] have examined several basic properties of a plasma consisting of finite-sized particles whose interactions are smooth at small separations. They found that, when the cloud size R (a measure of spreading-out of the cloud) was less than the Debye length, λ_D, longitudinal waves and Debye shieldings were nearly the same as for a real plasma, while collisional phenomena and short-wavelength fluctuations were much reduced. Their observations are not unexpected and support the trend towards use of simulation models having such artificially smoothed interactions. When the cloud size R is increased above the Debye length, λ_D, collisions and fluctuations rapidly disappear, but the plasma properties are much modified. In Chapter 2, we review the general theory for a model of finite-sized particles and present analysis of the collisional effects in the 2-species cloud plasma.

1.4 A brief history of numerical computations in the particle simulation

It has been a problem how we calculate the interparticle forces in the finite-sized particle plasma, using the digital computers. At the present time, two methods are known: One is a direct method without spatial grids and the other is an indirect method with spatial grids. In the indirect method, grids are set up in x-space, field quantities are defined only at the grid

points, and the interparticle forces are interpolated using the field quantities near the particle. This method is adopted throughout this thesis and is explained in detail in Chapter 3. Although it is known at the present time that the direct method without spatial grids is, in general, computationally more expensive and more complicate, Dawson *et al.* [17] devised a faster method of calculating the interparticle forces directly. In the sheet model [4], which is the earliest of the one-dimensional particle model and is considered to be a kind of the finite-sized particle models of the infinitesimally small cloud size (sometimes called "zero-sized particle"), the interparticle forces have been calculated directly, too. Even if we try extensive improvements in the direct method, however, the features of the present digital computer would help towards the development of the indirect method.

In the earliest simulations, the indirect methods used to relate particle quantities to grid quantities were chosen more or less on the basis of computational simplicity. For example, the density of particles at a grid point was taken to be the number of particles in the cell, divided by the cell volume, about the grid point; this was done in the 'fluids particle-in-cell (PIC) method' by Harlow and Evans [21] and Harlow [22]. This 'nearest-grid-point (NGP) assignment', applied to plasmas, achieved some smoothing such as eliminating forces between two charges of opposite sign in the same cell [23], but made for a jump in density and force as a particle passed a cell-boundary. The next step was to weight the particle density and force by linear interpolation to the grid points nearest the particle, as done in the 'cloud-in-cell (CIC) method' and the "collisionless particle-in-cell method' (simply called "collisionless PIC" or "PIC") [8]. Although these two methods are computationally equivalent (therefore, sometimes called "CIC-PIC"), CIC was devised in order to calculate the cloud (finite-sized particle) plasma [16], while PIC was an adaptation of the area weighting of velocities in fluids PIC to plasma density and force calculations. These interpolations removed the jump in density and force of NGP and lead to appreciable reduction in the grid noise [16].

1.5 The effects of the use of the spatial grids

In the optimized simulation model from the physical and commercial points of view, the use of spatial grids becomes inevitable, while a difficulty is the nonphysical interactions of particles with the spatial grids, which enhance the noise (called "grid noise"). Langdon has pointed out that these interactions induce a numerical instability [24] when the grid separation Δ becomes larger by a factor of about 10 than the Debye length λ_D. Okuda [25] confirmed this fact experimentally. Hockney [26] showed that the grid noise violated the conservation

law of total energy and heated up the plasma in the long time nonphysically. From a large number of simulation runs, he obtained a dependence on parameters concerning the heating and found a linear increase of total energy with time, which suggested that the heating was dominated by the stochastic process. Namely, the grid noise is considered to be an external random force; therefore, the energy flows in or out of the system, and the total energy of the system fluctuates in the short time and increases linearly with time in the long time due to the presence of the random force. Note that the shot noise never violates the conservation law of total energy because it is physical. Lewis *et al.* [27] pointed out that the fluctuation of total energy was greater than the increased energy in the case of the small grid noise and found a dependence on parameters concerning the fluctuation of total energy experimentally.

An energy check is generally used to monitor simulations. When the observed total energy changes by amounts small compared to other energies of importance, the simulation results suggest that the most of the exchange of energy between fields and particles has taken with a satisfactory accuracy. A good energy check, therefore, gives the credibility to the simulation. Nevertheless, the mechanism of the error of total energy had remained to be ambiguous. Works of Hockney and Lewis *et al.* contain only experimental results, and theoretical works which explain their results have been required. Abe, Miyamoto, and Itatani [28] have studied the effects of the grid noise on the total energy analytically by invoking the stochastic theory and have obtained a scaling law of the fluctuation of total energy, which depends on the number of spatial grids in the system, the number of particles in the Debye sphere, the model and so on. This scaling law is consistent with the empirical law obtained by Lewis *et al.* [27]. By measuring the fluctuation of total energy more accurately in actual simulations than Lewis *et al.*, a good agreement between theoretical and experimental results has been obtained by Abe *et al.* [28]. The analysis is also applied to an explanation and estimation of the heating or the linear increase of total energy with time observed by Hockney [26]. Chapter 3 contains the details of these results.

1.6 Application of the particle simulation to the HIPAC

It was firstly suggested by Janes [29] that unneutralized clouds of electrons could be confined by the toroidal magnetic field, which was produced within a conducting toroidal chamber. The induction of this magnetic field has been to inject and produce an electron plasma in the chamber (inductive charging [30, 31]). This device is sometimes called the "heavy ion plasma accelerator" or "HIPAC" [30], because it was devised in order to perform

experiments involving nuclear and energetic atomic reactions between heavy ions. In outline, the HIPAC utilizes the potential well due to a cloud of electrons in the conducting chamber. Its well serves the dual function of accelerating and trapping heavy ions that may be introduced, while the electrons of the cloud produce high degree of stripping of these ions. Since the ion energy is proportional to the charge state as well as to the well depth, a well depth of 20 million volts would create center-of-mass energies sufficient to overcome the Coulomb barrier for collisions between nuclei of all species. For the heavy elements ($Z \geqq 20$) this condition is difficult to be matched by any presently existing device. Well depth such as this appears to be accessible in the apparatus of the relatively modest dimensions and cost, because an extrapolation on present achievements suggests the possibility. If they can indeed be reached, a considerable range of experiments involving nuclear reactions between heavy elements becomes accessible. Thus, for example, collisions between like or unlike nuclei of atomic number in the medium range 30–50 should give rise to the inverse of the nuclear-fission process.

At first Janes presented experimental evidences indicating that a stable dense cloud of electrons with an associated negative electrostatic potential well could be produced inductively in cylindrical geometries [29]. Because the applications explained above require the toroidal geometry, Daugherty and Levy [32] presented the theoretical evidence that the selfconsistent azimuthally symmetric toroidal equilibria were possible for electron clouds without the necessity for a rotational transform [36]. The dioctron instability [33, 34], magnetron instability [34], and two stream ion-electron resonance instability [34], inherent in these systems, have been analyzed. These results have shown that the HIPAC is promising. On the basis of these works, the initial experiment [31] on the injection and containment of electron clouds in an azimuthally symmetric, toroidal apparatus was perfomed in order to exhibit the possibility of the applications. Mohri *et al.* [37] also obtained a quiescent equilibrium of the toroidal system by the use of a relativistic-electron-beam-source and showed the possibility of the applications proposed by Rostoker [38].

From a practical point of view, however, a defect of these machines is that the maximum density is restricted by the equilibrium and stability conditions. It has been suggested by Janes *et al.* [30] that the ratio $q = \omega_p^2 / \omega_c^2$, where ω_c and ω_p are the electron gyro- and plasma frequency respectively, should be roughly between 0.001 and 0.05. Accordingly, it is a problem how large q can be actually. We performed the simulations concerning the HIPAC and realized the quiescent equilibrium with $q = 0.08$, which was larger by a factor of 4 than that obtained experimentally in the toroidal apparatus [31]. In addition, we measured the

various physical quantities, which were impossible to measure in experiments, and compared them with the equilibrium theory. The details are presented in Chapter 4.

1.7 Application of the particle simulation to the r. f. confinement of plasmas in the magnetic field

From the technological point of view, it is pointed out that the open systems have several advantages over the closed ones in the magnetic confinement systems of plasmas. However, their large end loss inherent in open systems should be decreased or recovered for the open system to become superior to the closed systems. In these situations, a number of attempts have been made in order to improve the energy confinement in the open system.

Extensive investigations on the reduction of the end loss by the application of the r. f. electric field whose frequency is near the ion cyclotron frequency at the leakage hole of the open systems have been carried out by Watson and Kuo-Petravic [39], and Miyake *et al.* [40]. Also, very interesting results of containment with an electron resonance field have been shown by Consoli [41]. The machine with the electron resonance field, however, will be difficult to be used as a fusion reactor which has a magnetic field strength of about *100 k Gauss,* where the electron cyclotron frequency is about *300 G Hertz.* It will be difficult to make a uniform distribution of the r. f. power over a resonant surface of a large reactor. Another difficulty lies in the realization of a high-power generator with such a frequency.

The use of the ion cyclotron resonance removes these difficulties and results in the favourable ion heating. In addition, it is expected that the r. f. field could be coupled easily to ions in the line end region, because the thickness of the plasma in the line end is nearly equal to the ion Larmor diameter even if the plasma density is high. Actually, Miyake *et al.* [40] obtained some encouraging results as for the reduction of the plasma loss from the line end, although the problems are still unsolved concerning the loss from the spindle end.

As an example of the open system which has the only line ends, Moir [42] has proposed "Open Ended Toroidal Quadrupole", which consists of the eight separate circular coils plus the toroidal field coil. The important features of this configuration are (1) a high mirror ratio is possible, (2) the field lines are always favourably curved, (3) it does not have any spindle ends but only line ends, and (4) the configuration is azimuthally symmetric. These features are considered to be advantageous for the r. f. confinement of plasmas. Abe, Kawai, Yamada, and Itatani [43] performed the computer simulations in these systems and pointed out a possibility of the improvement in the energy confinement by the application of the r. f. electric field with

the ion cyclotron frequency.

In the treatment of Abe *et al.* [43], however, the r. f. electric field has been applied in a simplified way, and collisions have been introduced only for ions on the basis of a model of large angle scattering. Takizuka, Abe, Momota, and Namba [44] improved the above simulation model and developed more realistic model. The r. f. electric field is applied through the electrodes, and collisional effects are introduced both for ions and electrons. Further, a collision model is improved by the use of a modification of the Langevin equation [45] so as to include the small angle scattering. In Chapter 5, their simulation techniques and results are discussed.

REFERENCES

1. edited by B. Alder, S. Fernbach, and M. Rotenberg: *"Methods in Computational Physics"* Vol.9, Academic Press, New York and London (1970).
2. K. Hain and A. C. Kolb: Nucl. Fusion Suppl., Part 2 (1962) 561.
3. O. Buneman: Phys. Rev. 115 (1959) 503.
4. J. M. Dawson: Phys. Fluids 5 (1962) 445.
5. J. M. Dawson: Nucl. Fusion, Suppl., Part 3, (1962) 1033.
6. C. Smith and J. M. Dawson: Princeton University Plasma Physics Laboratory, Report Matt-151 (1963).
7. O. C. Eldridge and M. Feix: Phys. Fluids 5 (1962) 1307.
8. R. L. Morse and C. W. Nielson: Phys. Fluids 12 (1969) 2418; Phys. Rev. Letters 23 (1969) 1087.
9. I. B. Bernstein, J. M. Green, and M. D. Kruskal: Phys. Rev. 108 (1957) 546.
10. H. Okuda and J. M. Dawson: Phys. Fluids 16 (1973) 408.
11. D. Bohm: in *"The Characteristics of Electrical Discharges in Magnetic Fields"*, edited by A. Guthrie and R. Wakerling, McGraw-Hill, New York (1949) 201.
12. T. Tamano, R. Prater, and T. Ohkawa: Phys. Rev. Letters 30 (1973) 431.
13. C. G. Smith and A. S. Bishop: in *"Conference on Plasma Physics and Controlled Thermonuclear Fusion Research"* CN-24/D-9, Novosivirsk (1968)
14. D. O. Dickman, R, L. Morse, and C. W. Nielson: Phys. Fluids 12 (1969) 1708.

15. J. A. Byers, J. P. Holdren, J. Killeen, A. B. Langdon, A. A. Mirin, M. E. Rensink, and C. G. Tull: Phys. Fluids 17 (1974) 2061.
16. C. K. Birdsall and D. Fuss: J. Computational Phys. 3 (1969) 494.
17. J. M. Dawson, C. G. Hsi, and R. Shanny: *"Paper AI Conference Numerical Simulation Plasma."* Los Alamos Scientific Lab., LASL Report LA-3990 (1968).
18. A. A. Vlasov: *"Many-Particle Theory and Its Application to Plasma"* Gordon and Breach, New York (1961).
19. A. B. Langdon and C. K. Birdsall: Phys. Fluids 13 (1970) 2115.
20. H. Okuda and C. K. Birdsall: Phys. Fluids 13 (1970) 2123.
21. F. H. Harlow and W. M. Evans: Los Alamos Scientific Lab., LASL Report LA-2139.
22. F. H. Harlow: J. Assoc. Comp. Mach. 3-4 (1956–7) 137.
23. R. W. Hockney: Phys. Fluids 9 (1966) 1826.
24. A. B. Langdon: J. Computational Phys. 6 (1970) 247.
25. H. Okuda: J. Computational Phys. 10 (1972) 475.
26. R. W. Hockney: J. Computational Phys. 8 (1971) 19.
27. H. R. Lewis, A. Sykes, and J. A. Wesson: J. Computational Phys. 10 (1972) 85.
28. H. Abe, J. Miyamoto, and R. Itatani: J. Computational Phys. 19 (1975) 134.
29. G. S. Janes: Phys. Rev. Letters 15 (1965) 135.
30. G. S. Janes, R. H. Levy, H. A. Bethe, and B. T. Feld: Phys. Rev. 145 (1966) 925.
31. J. D. Daugherty, J. E. Eninger, and G. S. Janes: Phys. Fluids 12 (1969) 2967.
32. J. D. Daugherty and R. H. Levy: Phys. Fluids 10 (1967) 155.
33. R. H. Levy: Phys. Fluids 8 (1965) 1288.
34. O. Buneman, R. H. Levy, and L. M. Linson: J. Appl. Phys. 37 (1966) 3203.
35. R. H. Levy and R. W. Hockney: Phys. Fluids 11 (1968) 766.
36. L. Spitzer, Jr.: Phys. Fluids 1 (1958) 253.
37. A. Mohri, M. Masuzaki, T. Tsuzuki, and K. Ikuta: Phys. Rev. Letters 34 (1975) 574.
38. N. Rostoker: Particle Accel. 5 (1973) 93.
39. C. J. H. Watson and L. G. Kuo-Petravic: Phys. Rev. Letters 20 (1968) 1231.
40. S. Miyake, T. Sato, K. Takayama, T. Watari, S. Hiroe, T. Watanabe, and K. Husimi: J. Phys. Soc. Japan 31 (1971) 265.
41. T. Consoli: *"Proc. Third Intern. Conf. on Plasma Physics and Controlled Nuclear Fusion Research"* Vol.1, 2, IAEA, Vienna, (1969) 361.
42. R. W. Moir: Center d'Etude Nucleaires, Paris, Euratom Report EUR-CEA-FC 496 (1968)

43. H. Abe, K. Kawai, T. Yamada, and R. Itatani: J. Phys. Soc. Japan 33 (1972) 216.
44. T. Takizuka, H. Abe, H. Momota, and C. Namba: Plasma Phys. 17 (1975) 887.
45. S. Chandrasekhar: *"Review of Modern Physics"* Vol.15, Dover, New York (1954).

CHAPTER 2

COLLISIONAL EFFECTS IN A PLASMA OF THE FINITE-SIZED PARTICLES OF THE 2-SPECIES

2.1 INTRODUCTION

A fatal difficulty of the particle simulation of plasma exists in the high level of fluctuations at both short and long wavelengths, which can easily be so large as to mask the desired simulation, because the limitation of ability of the electronic computer forces us to use a reduced number of particles each with a larger charge and mass as compared with the laboratory plasma. By the use of the finite-sized particle model or the cloud model [1, 2] in which the Coulomb interparticle forces of small separation are automatically smoothed out, we can successfully reduce the short-wavelength fluctuations and collision phenomena, simulating the long-wavelength and collective interactions of plasma exactly. Then the present digital computer can simulate the collisionless plasma and reproduce the various collective phenomena not only in the 1-dimensional system, but also in the 2- or 3-dimensional system. Langdon and Birdsall [1], and Okuda and Birdsall [2] studied the properties of the uniform, stable, unmagnetized single-species cloud plasma and clarified the differences between them and the point particle plasmas. They have shown that the collisional evolution for the cloud plasmas can be governed by the Balescu-Gurnsey-Lenard (We abbreviate it BGL in the following) kinetic equation [3, 4, 5] in spite of a reduced number of particles because the clouds can overlap freely each other due to the smoothing-out of the interparticle forces of small separation. Their prediction can be verified by the observation of the orbits of test particles in phase space in the thermal equilibrium cloud plasmas, which can be simulated by the use of the CIC-PIC model [6, 7] or the dipole approximation scheme [8] with the appropriate higher-mode-cutoff scheme [9]. Actually, Okuda [10], and Matsuda and Okuda[11] verified the predictions of the BGL kinetic equation in a satisfactory way, measuring the fluctuation spectra of electric

fields, and diffusions and drags in velocity space.

Considering only static shielding effects of plasma [1, 2] which change the interaction forces of colliding particles from the Coulomb force of isolated particles, Langdon and Birdsall [1] estimated a collision frequency as a rough measure of the collisional effects of the cloud plasma and derived the Fokker-Planck equation as an approximate kinetic equation. Okuda and Birdsall [2] estimated the collisional effects more precisely than Langdon and Birdsall [1], and calculated them numerically by considering not only the static shielding effects but the dynamical shielding effects. As a result they pointed out that the collisional effects on a test cloud, which had a larger cloud size and faster velocity than the Debye length and the thermal velocity respectively, were drastically enhanced. In their work, however, they assumed that ion was the uniform background for charge neutralization and neglected the effects of ion on the collision in the multispecies plasma. Judging from the origin of enhancement of collisions discussed in Reference 2, we may expect that the dynamical shielding effects of ion cannot be neglected for the cloud with the velocity near to or smaller than the ion thermal or sound velocity.

In this Chapter, we study the collisional effects of the 2-species cloud plasma by transforming the form of the original BGL kinetic equation to a form like the Landau equation [12]. Namely, we define a scalar quantity χ as a measure of the collisional effects of a test particle with the arbitrary velocity. This quantity χ is adjusted to be reduced to the usual Coulomb logarithm ($\ln\Lambda$) [13, 14] independent of velocity of the test clouds, when the cloud size R decreases to the impact parameter [13].

In Section 2.2, we review the dynamical equations of the plasma composed of the finite-sized particles and characteristic differences of the dispersion in the longitudinal mode between the point particle plasma and the cloud plasma. In Section 2.3, we define the quantity χ and, in Section 2.4, we discuss the collisional effects of the 2-species cloud plasmas in both isothermal and nonisothermal cases.

2.2 THE DYNAMICAL EQUATIONS OF THE FINITE-SIZED PARTICLE (CLOUD) PLASMA

As explained in Section 1.3, the charge density of a cloud whose center is at the origin is changed from $e\delta(x)$ to $eS(x)$, where e is the total charge and S is the shape factor. If ρ_p and $\boldsymbol{J}_p$ are the charge and current densities of a system of point charges, therefore, the densities ρ_c and $\boldsymbol{J}_c$ for a system of clouds, whose centers coincide with the point particles, are

$$\begin{pmatrix} \rho_c(x,t) \\ J_c(x,t) \end{pmatrix} = \int dx' S(x-x') \begin{pmatrix} \rho_p(x',t) \\ J_p(x',t) \end{pmatrix} \tag{2.1}$$

These cloud densities are to be used in the Maxwell equations to find the fields E and B. The Lorentz force on a cloud with center position x and velocity v, and the equations of motion of it are

$$F(x,v,t) = e \int dx' S(x-x') \cdot (E(x',t) + v \times B(x',t)) , \tag{2.2a}$$

$$\frac{dx}{dt} = v , \qquad m \frac{dv}{dt} = F , \tag{2.2b}$$

where m is the mass of the cloud.

The relations of (2.1) and (2.2a) are convolutions and, therefore, take on a very simple form when Fourier transformed:

$$\begin{pmatrix} \rho_c(k,t) \\ J_c(k,t) \end{pmatrix} = S(k) \begin{pmatrix} \rho_p(k,t) \\ J_p(k,t) \end{pmatrix} , \tag{2.3}$$

$$F(k,v,t) = e S(-k) (E(k,t) + v \times B(k,t)) ,$$

where

$$S(k) = \int dx S(x) \exp(-ik \cdot x) .$$

These transform convention is such that in the point particle limit $R \to 0$ or short wavelength limit $k \to \infty$, $S(k) \to 1$. When the size of the cloud is denoted by R, $S(k)$ becomes small for $|k| \gtrsim R^{-1}$.

Using Eq. (2.3) and a little care we can now re-do most plasma theory with few changes by the replacement of the charge e by $eS(k)$. For example, the dispersion relations for a uniform Vlasov gas of clouds are unchanged except that the plasma frequency squared, ω_p^2, must be everywhere multiplied by $S^2(k)$. This result could be viewed as a k dependent plasma frequency or, density when adapting linear stability analyses, etc., to cloud plasmas. Here we show the expressions of the longitudinal dielectric function for a cloud plasma,

$$\epsilon(\boldsymbol{k}, \omega) = 1 + S^2(\boldsymbol{k}) \frac{\omega_p^2}{k^2} \int \boldsymbol{k} \cdot \frac{\partial f_0}{\partial v} \frac{dv}{\omega - \boldsymbol{k} \cdot v}, \tag{2.4}$$

where we assume a single-species plasma for simplicity in this Section and the standard symbol definition. Space-time dependence $\exp(i\boldsymbol{k} \cdot \boldsymbol{x} - i\omega t)$ is assumed, and the usual remarks about analyticity apply. For a Maxwellian velocity distribution with the thermal velocity $v_t = [(1/3 \cdot v)_{av}^2]^{1/2}$, the dielectric function becomes

$$\epsilon(k, \omega) = 1 - \frac{1}{2} \left(\frac{S\omega_p}{kv_t}\right)^2 Z'\left(\frac{\omega}{\sqrt{2}\, kv_t}\right), \tag{2.5}$$

where Z is the plasma dispersion function of Fried and Conte [15].

The dispersion relation for longitudinal waves is $\epsilon = 0$. When $kv_t/S\omega_p = k\lambda_D/S \ll 1$, we can use the large argument asymptotic expansion for Z' and find an approximate solution for ω which shows weak Landau damping of the oscillations

$$(\mathrm{Re}\ \omega)^2 \simeq S^2(k)\ \omega_p^2 + 3k^2 v_t^2, \tag{2.6a}$$

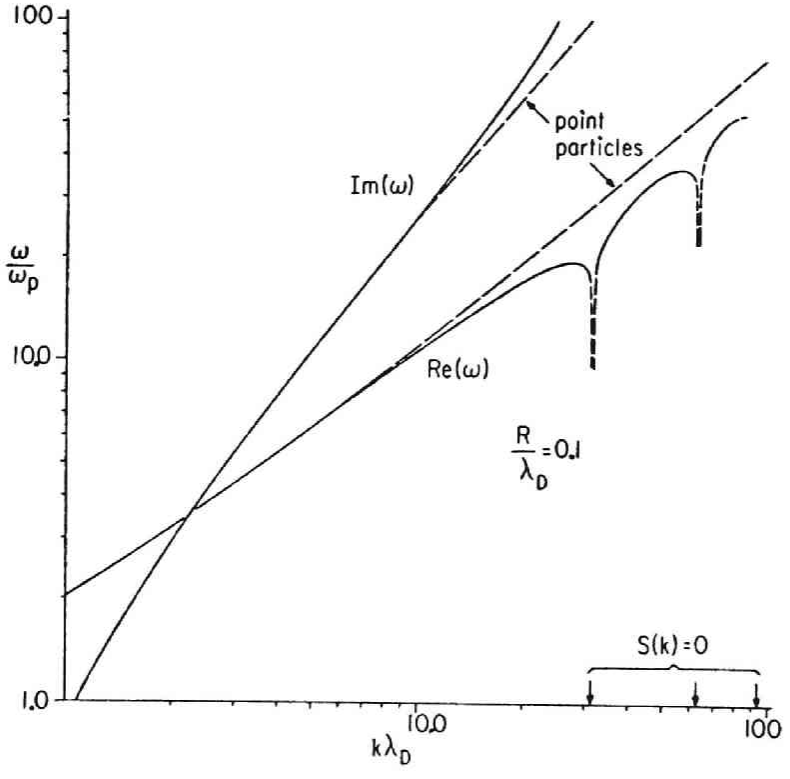

Fig. 2.1 Dispersion relation roots for small clouds. (After Landgon and Birdsall [1]).

$$\mathrm{Im}\,\omega \simeq -\left(\frac{\pi}{8}\right)^{1/2} S\,\omega_p \left(\frac{S}{k\lambda_D}\right)^3 \exp\left[-\frac{1}{2}\left(\frac{S}{k\lambda_D}\right)^2\right]. \tag{2.6b}$$

With small clouds $(R < \lambda_D)$ and weak damping we have $kR < k\lambda_D \ll 1$ so that $S \simeq 1$. Thus, the weakly damped oscillations are little affected with small clouds, as we would hope (See Fig. 2.1).

For large clouds $(R \gtrsim \lambda_D)$ and weak damping, Re ω can be very different from the point-particle result when $kR \gtrsim 1$ (Fig. 2.2).

When $k\lambda_D/S \gtrsim 1$, the oscillations are strongly damped. Thus, in a cloud plasma the onset of damping as k increases occurs when $k\lambda_D \simeq 1$ or when kR is large enough. For some cloud shapes, such as cubes, $S \to 0$ for finite k. Where this happens the asymptotic solutions for strong damping show that Im $\omega \to -\infty$, Re $\omega \to 0$, which can be seen in Fig. 2.2. Of course, when S is very small the electric interaction is disabled and the clouds free stream, and the time evolution differs from $\exp(-i\omega t)$.

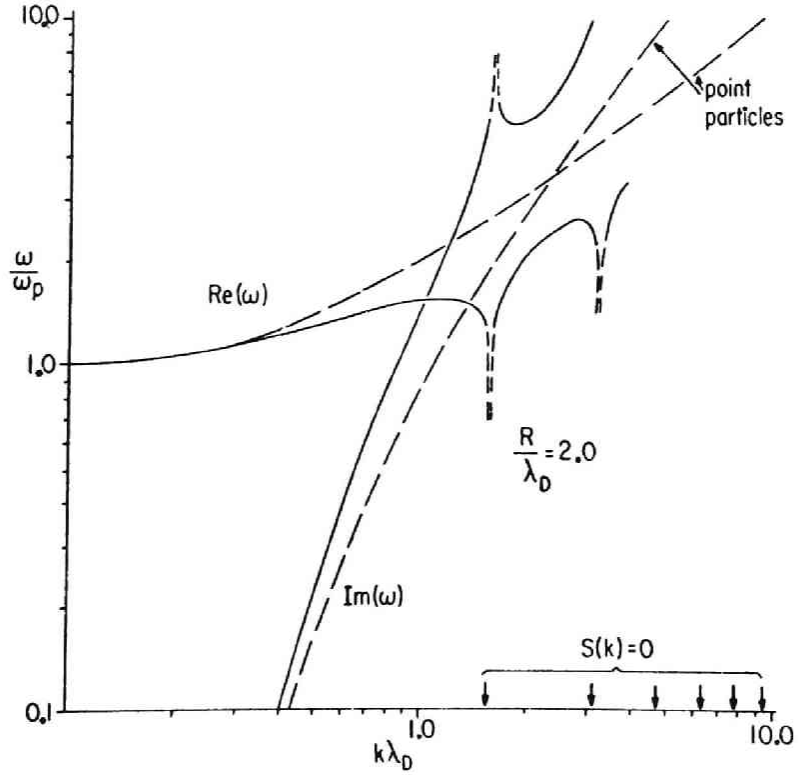

Fig. 2.2 Dispersion relation roots for large clouds. (After Langdon and Birdsall [1]).

2.3 A KINETIC EQUATION FOR A FINITE-SIZED PARTICLE PLASMA OF 2-SPECIES

The BGL kinetic equation of a uniform, stable, unmagnetized 2-species cloud plasma is given by the straightforward extension of that in the case of the single-species cloud plasma [1, 2]. For simplicity, ion is assumed to be single-charged. The kinetic equation for a test cloud distribution function of species α in the M-dimensional system $(M=2,\ 3)$ is

$$\frac{\partial f_\alpha}{\partial t} = \sum_{\beta=e,i} \frac{\pi}{(2\pi)^M} \frac{\omega_{p\alpha}^2 \omega_{p\beta}^2}{n} \frac{\partial}{\partial v_{\alpha i}} \int dv_\beta U_{ij} \left(\frac{m_\beta}{m_\alpha} f_\beta \frac{\partial f_\alpha}{\partial v_{\alpha j}} - f_\alpha \frac{\partial f_\beta}{\partial v_{\beta j}} \right), \tag{2.7}$$

$$U_{ij} = \int dk \frac{|S(k)|^4 k_i k_j \delta(k \cdot u)}{k^4 |\epsilon(k,\ k \cdot v_\alpha)|^2}, \tag{2.8}$$

where u is equal to $v_\alpha - v_\beta$, n is the density, subscripts α and β denote a species (i : ion and e : electron), the summation over repeated subscripts i, j is assumed, and m_α and $\omega_{p\alpha}$ are the mass and the plasma angular frequency for species α, respectively. Note that m_α and e_α are the reduced mass and charge of a particle per unit length for the 2-dimensional case $(M=2)$. When $S(k)=1$, Eqs. (2.7) and (2.8) are reduced to the results for the point particle plasma. For convenience, we assume the Maxwellian as the velocity distribution, when we calculate the dielectric functions, as follows;

$$\epsilon(k, \omega) = 1 + \frac{|S(k)|^2}{k^2 \lambda_D^2} \{ X(\omega) + i Y(\omega) \}, \tag{2.9}$$

$$\left.\begin{aligned} X(\omega) &= -\sum_{\beta=e,i} \frac{\lambda_D^2}{2\lambda_{D\beta}^2} \mathrm{Re}\left(Z'\left(\frac{\omega}{\sqrt{2} k v_{t\beta}} \right) \right), \\ Y(\omega) &= -\sum_{\beta=e,i} \frac{\lambda_D^2}{2\lambda_{D\beta}^2} \mathrm{Im}\left(Z'\left(\frac{\omega}{\sqrt{2} k v_{t\beta}} \right) \right), \end{aligned}\right\} \tag{2.10}$$

where $v_{t\beta}$ is the thermal velocity, $v_{t\beta} = (\kappa T_\beta / m_\beta)^{1/2}$, and the Debye length λ_D is defined as

$$\frac{1}{\lambda_D^2} = \sum_{\beta=e,i} \frac{1}{\lambda_{D\beta}^2} = \sum_{\beta=e,i} \frac{\omega_{p\beta}^2}{v_{t\beta}^2}. \tag{2.11}$$

In the following, we adopt the sharp-cutoff cloud [1, 2] as a shape factor, because it is the simplest in k-space and convenient to express the BGL kinetic equation as analytically as possible. The sharp-cutoff cloud is represented as follows;

$$S(k) = 1 \quad \text{for} \quad |k| \leqq \frac{1}{R} = k_R, \qquad S(k) = 0 \quad \text{for} \quad |k| > \frac{1}{R} \quad , \tag{2.12}$$

where R is the characteristic radius of the cloud.

When we calculate U_{ij}, we transform the coordinates of k-space from the cartesian coordinates to the cylindrical coordinates (k_ρ, k_θ, k_z) for the 3-dimensional case and obtain the results, analytically integrated over k_ρ and k_z. Substituting them into Eq. (2.7) yields

$$\frac{\partial f_\alpha}{\partial t} = \sum_{\beta=e,i} \frac{\pi^{M-1}}{(2\pi)^M} \lambda_{De}^{3-M} \frac{\omega_{p\alpha}^2 \omega_{p\beta}^2}{n} \frac{\partial}{\partial v_{\alpha i}} \int dv_\beta \chi^{(M)}(w)$$

$$\times \left(\frac{\delta_{ij}}{u} - \frac{u_i u_j}{u^3} \right) \left(\frac{m_\beta}{m_\alpha} f_\beta \frac{\partial f_\alpha}{\partial v_{\alpha j}} - f_\alpha \frac{\partial f_\beta}{\partial v_{\beta j}} \right), \tag{2.13}$$

$$\chi^{(3)}(w) = \frac{2}{\pi} \int_0^{\pi/2} \left[\frac{1}{4} \ln \frac{\{(k_R \lambda_D)^2 + X(w\cos\psi)\}^2 + \{Y(w\cos\psi)\}^2}{\{X(w\cos\psi)\}^2 + \{Y(w\cos\psi)\}^2} \right.$$

$$\left. - \frac{X(w\cos\psi)}{2|Y(w\cos\psi)|} \left\{ \tan^{-1} \frac{(k_R \lambda_D)^2 + X(w\cos\psi)}{|Y(w\cos\psi)|} - \tan^{-1} \frac{X(w\cos\psi)}{|Y(w\cos\psi)|} \right\} \right] d\psi, \tag{2.14}$$

$$\chi^{(2)}(w) = \left\{ \int_0^{k_R \lambda_D} dx \frac{2x^2}{\{x^2 + X(w)\}^2 + \{Y(w)\}^2} \right\} \frac{\lambda_D}{\lambda_{De}} \quad , \tag{2.15}$$

$$w = v_\alpha \cos\theta_\alpha \ , \tag{2.16}$$

where $\cos\theta_\alpha = v_\alpha \cdot u / (|v_\alpha| \cdot |u|)$. Note that the term in the square bracket of Eq. (2.14) is reduced to the term in the curly bracket of Eq. (10.43) in Reference 14 in the case of point particles.

When we neglect the dynamical shielding effect or we set v_α equal to zero, as Langdon and Birdsall [1] have done for the electron plasma, we obtain the following as an order estimation of $\chi^{(M)}(w)$,

$$\chi^{(M)}(w) \simeq \chi^{(M)}(0) = L^{(M)}(k_R\lambda_D)\left(\frac{\lambda_D}{\lambda_{De}}\right)^{3-M} \quad \text{for } w < v_{ti}, \tag{2.17a}$$

$$\chi^{(M)}(w) \simeq L^{(M)}(k_R\lambda_{De}) \quad \text{for } w \simeq v_{te}, \tag{2.17b}$$

$$L^{(3)}(x) \equiv \frac{1}{2}\left\{\ln(1+x^2) - \frac{x^2}{x^2+1}\right\}, \tag{2.18}$$

$$L^{(2)}(x) \equiv \tan^{-1}x - \frac{x}{x^2+1}. \tag{2.19}$$

In the 3-dimensional case $(M=3)$, the first term of $L^{(3)}(k_R\lambda_D)$ diverges, if the cloud size R becomes infinitesimally small or k_R becomes infinite. In this case corresponding to the point particle, however, we should consider the breakdown of the BGL kinetic equation due to the presence of close encounter. The effective value of k_R can be estimated as the inverse of the average distance of the closest approach between two colliding particles and the first term of $L^{(3)}$ represents the major effects as long as $n\lambda_D^3 \gg 1$. Then we get the standard point-particle results for the 3-dimensional case:

$$L^{(3)}(k_R\lambda_D) = \ln\Lambda,\ \Lambda = 4\pi N_D = 4\pi n\lambda_D^3 \quad \text{if} \quad k_R = \frac{4\pi\epsilon_0\kappa T}{e^2}. \tag{2.20}$$

For the electron plasma, in which the ion is background for charge neutralization, we can obtain the BGL kinetic equation by omitting the terms referring to the ion in summation over the subscript β in the preceding equations, for example, by substituting λ_{De} for λ_D.

2.4 NUMERICAL RESULTS AND PROPERTIES OF $\chi^{(M)}$

The numerical factor $\chi^{(M)}$ depends on $w = v_\alpha\cos\theta_\alpha$ and the cloud size R, and shows the measure of the magnitude of the collisional effect in the case of the cloud plasma. In other words, study of the properties of $\chi^{(M)}$ informs us of a rough estimation of the collisional effect for the cloud plasma. It is usually convenient to normalize the physical quantities in terms of the quantities associated with the electrons (for example T_e, m_e, ω_{pe}, and λ_{De}). These normalizations allow us to make a direct comparison of the collisional effects in the 2-species plasma with those in the electron plasma obtained in References 1 and 2. Therefore, we choose the mass ratio m_i/m_e and the temperature ratio T_i/T_e as parameters. We show the

values of $\chi^{(M)}$ vs w in Fig. 2.3 (3-dimensional, isothermal case), Fig. 2.4 (3-dimensional, non-isothermal case), Fig. 2.5 (2-dimensional, isothermal case), and Fig. 2.6 (2-dimensional, noniso-thermal case). These results are integrated numerically by the use of Simpson's formula. For the 3-dimensional cases, we choose a value of $K_R\lambda_{De} = 100$, which nearly corresponds to the point-particle plasma. We show the values concerning the electron plasma by the broken lines. Therefore, the broken lines shown in Figs. 2.3 and 2.5 have the same values as in Figs. 2.4 and 2.6, respectively.

2.4–1 The case of $T_i = T_e$ *(3-dimension)*

Figure 2.3 shows $\chi^{(3)}$ vs w in the isothermal plasma. When w is much larger than v_{ti}, or the ion is considered to be the background for the charge neutralization, the value of $\chi^{(3)}$ is independent of the mass ratio m_i/m_e and equal to the values in the electron plasma indicated by the broken line.

The value of $\chi^{(3)}$ is kept an almost constant value equal to $L^{(3)}/(k_R\lambda_{De})$ in the region of $v_{ti} \ll w \lesssim v_{te}$, and rapidly increases with w in the region of $w > v_{te}$ to attain to the same order as the value in the case of the point particle. Note that the collisional effects are successfully reduced for the particle with a velocity smaller than v_{te} as the cloud size R increases. These behaviors agree with those in the diffusion coefficients and friction coefficient which Okuda and Birdsall [2] obtained in the case of the electron plasma. Namely, $\chi^{(3)}$ is almost constant in $v_{ti} \ll w \lesssim v_{te}$, because it is determined by the static shielding effect of the electrons, and increases in $w > v_{te}$, because the dynamical shielding effect or the emission of waves with a wavelength of $\lambda \sim 2\pi v_\alpha/\omega_{pe}$ enhances the value of $\chi^{(3)}$. In the point particle plasma, this enhancement is negligible as compared with the contribution of the short wavelength fluctuations to the collisional effects, while in the cloud plasma it cannot be neglected because the contribution of the short wavelength fluctuation is truncated for the wave numbers of $k > 1/R$ and much reduced.

In the region of $w < v_{ti}$, the ions can participate with the electrons in the shielding of the electric field of the short wavelength. In this region, therefore, the static shielding effect is larger, and the Debye length determining the magnitude of $\chi^{(3)}$ is smaller by a factor of $\lambda_D/\lambda_{De} = (1 + (\lambda_{De}/\lambda_{Di})^2)^{-1/2}$ than that in $w > v_{ti}$. The value of $\chi^{(3)}$ is kept a constant value equal to $L^{(3)}/(k_R\lambda_D)$ in $w < v_{ti}$, independently of the mass ratio. As w becomes larger than v_{ti}, the static shielding effect of ion vanishes because of the larger mass of ion, and the value

of $\chi^{(3)}$ increases to the value of $L^{(3)}/(k_R \lambda_{De})$.

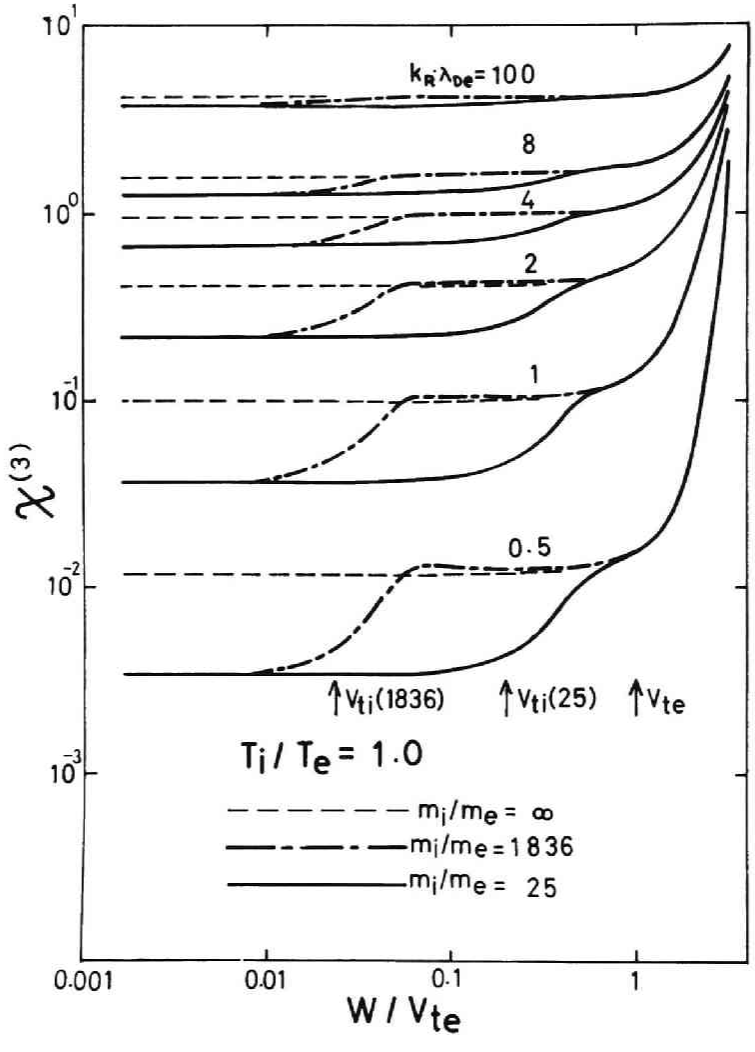

Fig. 2.3 The numerical factors $\chi^{(3)}$ vs the velocity w, defined by Eq. (2.14) for the 3-dimensional, isothermal cases. The broken lines, and solid and chain lines correspond to the single species or electron clouds $(m_i/m_e = \infty)$, and to the 2-species cloud plasmas of $m_i/m_e = 25$ and $m_i/m_e = 1836$, respectively. The broken lines tend to the solid and chain lines, as w becomes larger than v_{te}. The top curves refer to the sufficiently small clouds comparable to the point particles and depend slightly on w. In this and the following three figures, arrows indicate the positions of $w = v_{ti}$, C_s in the case of $m_i/m_e = 25$ and 1836.

2.4–2 The case of $T_i \neq T_e$ *(3-dimension)*

Figure 2.4 shows $\chi^{(3)}$ vs w in the case of $T_i/T_e = 0.1$. In the region of $w < v_{ti}$, $\chi^{(3)}$ is equal to $L^{(3)}(K_R \lambda_D)$ as well as in the isothermal case. In this region, the value of $\chi^{(3)}$ is smaller than in the case of $T_i = T_e$, because λ_D are $0.7\ \lambda_{De}$ and $0.3\ \lambda_{De}$ in the case of $T_i = T_e$ and $T_i = 0.1\ T_e$, respectively. In the region of $w > v_{te}$, $\chi^{(3)}$ is equal to that of the isothermal case, or of the case of the electron plasma. A feature of this case is that the

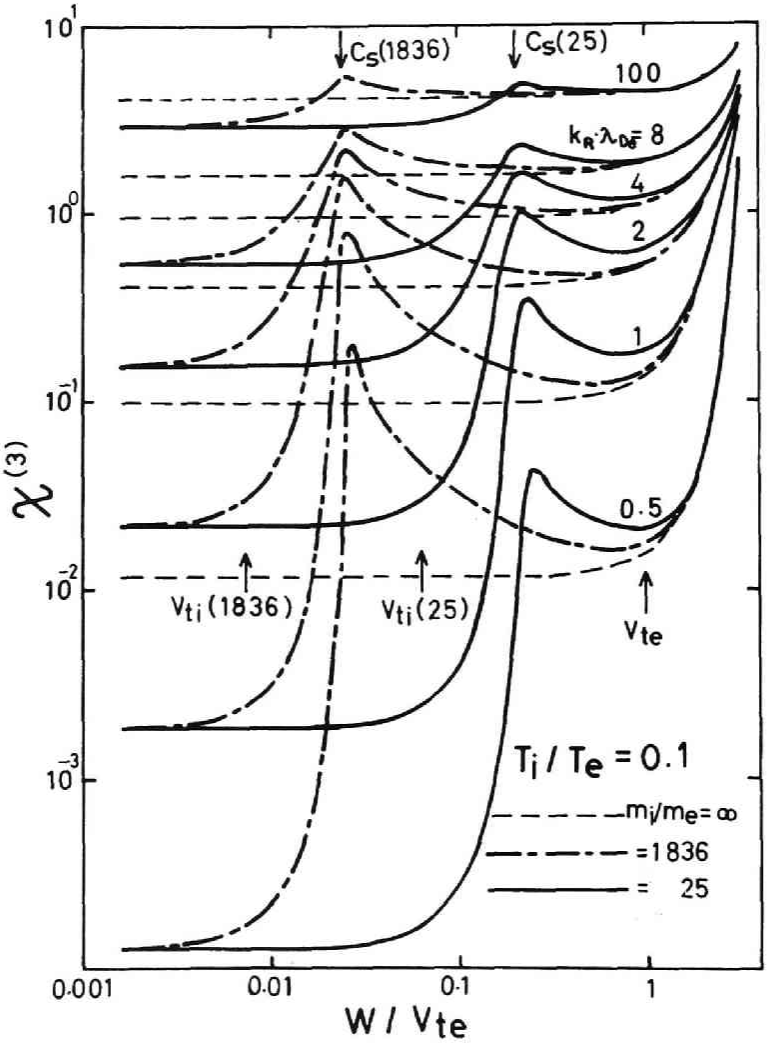

Fig. 2.4 The numerical factor $\chi^{(3)}$ for the 3-dimensional, nonisothermal cases $(T_i/T_e = 0.1)$. These values of $\chi^{(3)}$ depend strongly on w and have sharp peaks near the ion sound velocity C_s.

value of $\chi^{(3)}$ has a sharp peak near the value of w equal to the ion sound velocity C_s because of the emission of the ion sound wave, of which wavelength is equal to $2\pi C_s/\omega_{pi}$. This is similar to the result that $\chi^{(3)}$ is enhanced in $w > v_{te}$ because of the emission of the plasma wave. In the case of the smaller mass ratio, this peak value decreases slightly. The positions of the peak in w increase slightly, as the cloud R is larger.

2.4–3 The 2-dimensional cases

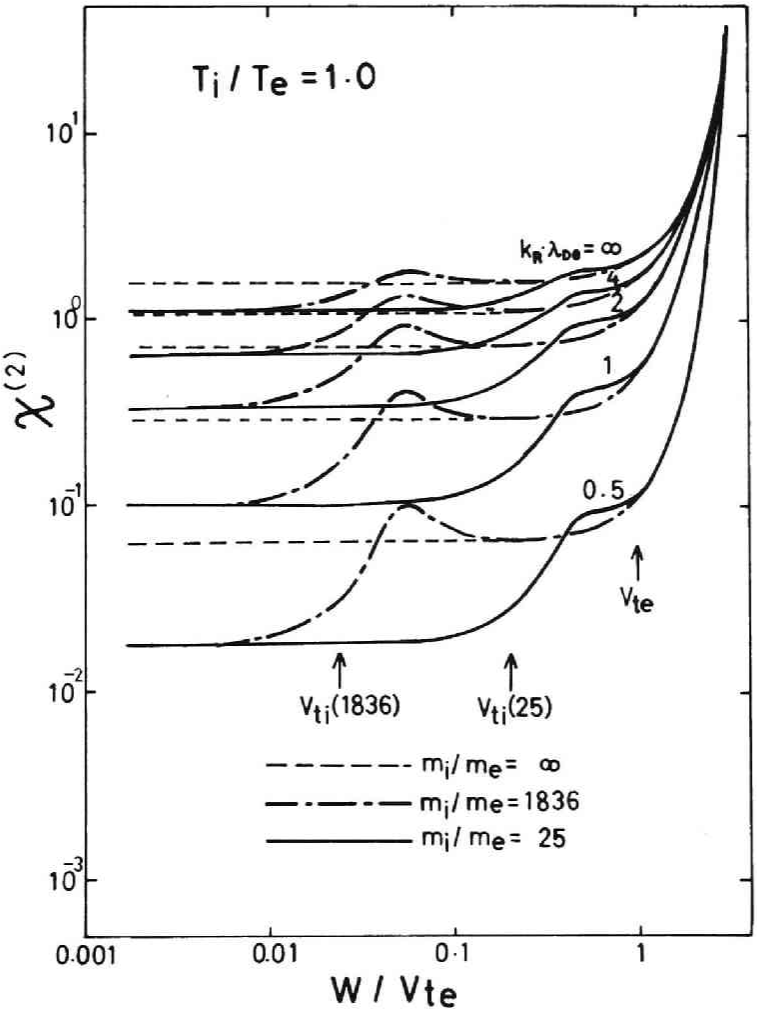

Fig. 2.5 The numerical factors $\chi^{(2)}$ vs w defined by Eq. (2.15) for the 2-dimensional, isothermal cases. Dependences of $\chi^{(2)}$ on w are similar to the 3-dimensional cases (See Fig. 2.3). In the region of $w \gg v_{te}$, however, $\chi^{(2)}$ increases more steeply than $\chi^{(3)}$, and is not constant in the case of the point particle.

In the 2-dimensional cases, Figs. 2.5 and 2.6 show the values of $\chi^{(2)}$ vs w in the case of $T_i = T_e$ and $T_i = 0.1\ T_e$, respectively. These characteristic features resemble the 3-dimensional cases. Namely, the values of $\chi^{(2)}$ in the regions of $w < v_{ti}$ and C_s (or v_{ti}) $< w < v_{te}$ are equal to $\lambda_D/\lambda_{De}\, L^{(2)}(k_R \lambda_D)$ and $L^{(2)}(k_R \lambda_{De})$ respectively, and are enhanced in $w > v_{te}$ because of the emission of the plasma wave. In the nonisothermal case, the enhancement caused by the emission of the ion sound wave is observed also. Because the function $L^{(2)}(x)$ depends on x more gently than $L^{(3)}(x)$, the dependence of $\chi^{(2)}$ on the cloud size R is weaker than that

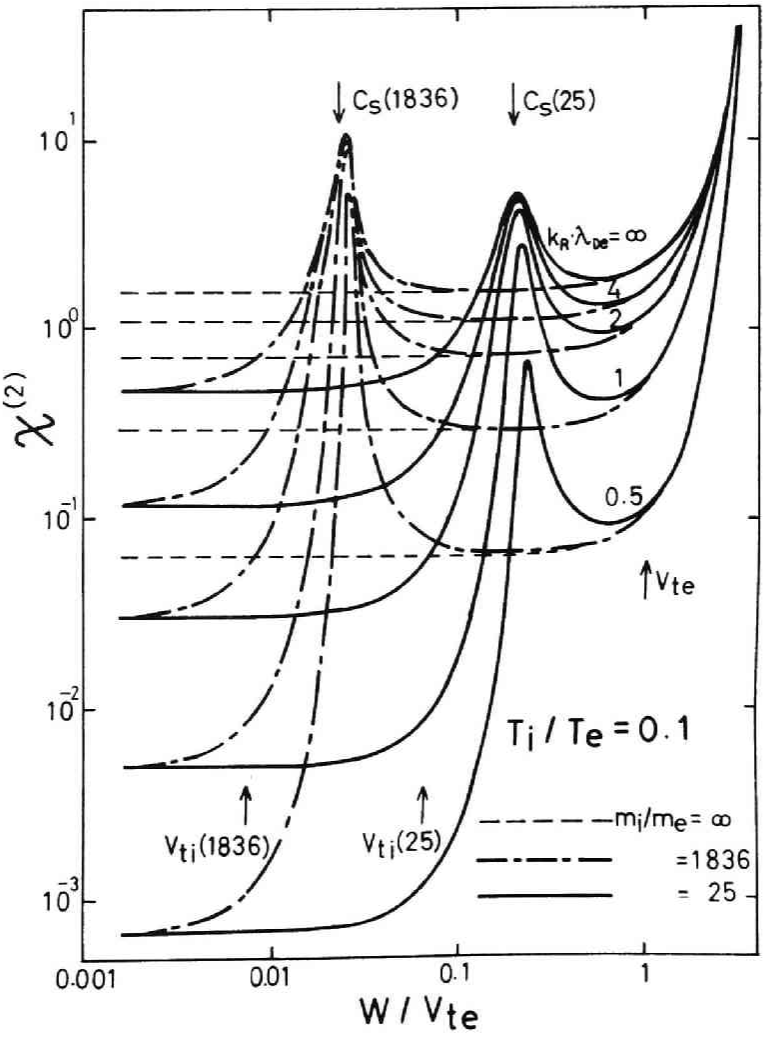

Fig. 2.6 The numerical factors $\chi^{(2)}$ vs w for the 2-dimensional, nonisothermal cases ($T_i/T_e = 0.1$). The peaks in $w \simeq C_s$ are much sharper than those of the 3-dimensional cases (See Fig. 2.4).

of $\chi^{(3)}$. On the other hand, $\chi^{(2)}$ is not constant in w, even if the cloud size R becomes infinitesimally small.

2.5 CONCLUSIONS

The properties of the cloud plasma, which is a physical model considered in the particle simulation, differ from those of the real plasma in the phenomena of the collisions and the fluctuations. Especially, the Landau equation which expresses the evolution of the system due to the collisional effects is no longer valid, if the cloud size becomes comparable with the Debye length. Accordingly, we study the collisional effects of the 2-species cloud plasma by transforming the BGL kinetic equation for a cloud plasma to a form like the Landau equation. Then we define a quantity $\chi^{(M)}$ as a measure of the collisional effect. It depends on the cloud velocity and the cloud size. When the cloud size is sufficiently small, $\chi^{(M)}$ is reduced to the Coulomb logarithm in the 3-dimensional case. Although we adopt the sharp-cutoff cloud as a representative one for simplicity, our analyses can be applied to the other clouds, for example, the Gaussian cloud. In the case, we can expect that the general behaviors of $\chi^{(M)}$ are not altered.

The velocity dependence of $\chi^{(M)}$ of the 2-species cloud plasma is different from that of the electron cloud plasma in a test cloud with the velocity near to or smaller than the ion thermal velocity or the ion sound wave velocity. Especially, this phenomenon is remarkable in the nonisothermal plasmas. Even in the point particle plasma, it is known that the Landau equation is not accurate in the highly nonisothermal case ($T_e \gtrsim 1000\ T_i$) [16]. In the cloud plasma, however, the value of $\chi^{(M)}$ is strongly influenced by the excitation of the ion sound wave and has the peak near the ion sound wave velocity, although the temperature ratio is considerably low ($T_e \simeq 10\ T_i$). Therefore, we should pay attention to this effect, when we simulate the 2-species plasma with the particle model.

In the simulations in which the collisional effect is one of the mechanisms dominating the phenomenon, therefore, it is not appropriate to use the collisional effects inherent in the cloud plasma. From the computational point of view, it is better to use a collision model such as the Monte-Calro method in which the effects of the binary collision are added to the sufficiently collisionless cloud plasma. One of the complete models, which can express the whole natures of the binary collision, has been developed by the author and his coworker [17].

REFERENCES

1. A. B. Langdon and C. K. Birdsall: Phys. Fluids 13 (1970) 2115.
2. H. Okuda and C. K. Birdsall: Phys. Fluids 13 (1970) 2123.
3. R. Balescu: Phys. Fluids 3 (1960) 52.
4. A. Lenard: Ann. Phys. (N. Y.) 3 (1960) 390.
5. R. L. Gurnsey: Phys. Fluids 5 (1962) 322.
6. C. K. Birdsall and D. Fuss: J. Computational Phys. 3 (1969) 494.
7. R. L. Morse and C. W. Nielson: Phys. Fluids 12 (1969) 2418.
8. W. L. Kruer, J. M. Dawson, and B. Rosen: J. Computational Phys. 13 (1973) 114.
9. H. Abe, J. Miyamoto, and R. Itatani: J. Computational Phys. 19 (1975) 134.
10. H. Okuda: Phys. Fluids 15 (1972) 1268.
11. Y. Matsuda and H. Okuda: Phys. Fluids 18 (1975) 1740.
12. L. D. Landau: Zh. Eksp. Teor. Fiz. 7 (1937) 203.
13. B. A. Trubnikov: in *"Reviews of Plasma Physics"* Vol. 1, edited by A. M. A. Leontvich, Consultant Bureau, New York (1965).
14. S. Ichimaru: *"Basic principles of Plasma Physics"* W. A. Benjamin Inc., Massachusettes (1973).
15. B. D. Fried and S. D. Conte: *"The Plasma Dispersion Function"* Academic, New York (1961)
16. V. P. Silin and L. M. Gorbunov: Soviet Phys. Doklady 7 (1963) 751.
17. T. Takizuka and H. Abe: Kakuyugo Kenkyu Vol. 34/Supplement No. 1 (in Japanese) (1975) 83.; Submitted to J. Computational Phys.

CHAPTER 3

GRID EFFECTS ON THE PLASMA SIMULATION BY THE FINITE-SIZED PARTICLE

3.1 INTRODUCTION

About the so-called usual models, in which the total momentum is conserved, it is well known that the total energy is not conserved due to the nonuniformity of space caused by spatial grids. From a large number of runs, Hockney has derived empirical laws of the error of total energy [1, 14]. Assuming a linear increase in time, he defined the heating time τ_H, during which the total energy increases by 25%. The conception of the heating time is useful in the case of sufficiently large error (an example is presented in Reference [1, Fig. 4]), or has a meaning for long periods of time. In the usual simulations, however, the heating time cannot be measured, because the energy increment is much smaller than the energy fluctuation, which is the same kind of numerical error as the energy increment. Accordingly, the measurement of the fluctuation in total energy is useful for monitoring simulations.

In this Chapter, we evaluate the fluctuation of total energy on simple assumptions and make a comparison between these estimations and the numerical results in the usual models. Here we explain the differences between the energy increment and the energy fluctuation along the outline of Hockney's consideration [1, P. 24], because we consider that these two quantities are dominated by the same stochastic process. We define K_g as the difference between the initial total energy H_0, and $\bar{K}_g$ as the energy increment, which is obtained by averaging the fluctuation of K_g during a sufficiently long period of time. Then the energy increment in time t, which is due to the presence of the unphysical grid force δF, is

$$\bar{K}_g = \frac{N_p m}{2} \{ \Delta v^2 \} = \frac{N_p}{2m} \{ \int_0^t \delta F \, dt \}^2 = \frac{1}{2m} < \delta F^2 > t \tau_c \ , \tag{3.1}$$

where $<\delta F^2>$ is a random force fluctuation of square magnitude, τ_c is a correlation time, m is the particle mass, and N_p is the number of particles. The standard deviation of K_g, $\sigma\{K_g\}$, is considered as follows:

$$\sigma\{K_g\} = \sigma\{N_p m\ (v \cdot \Delta v)\} = \{N_p{}^2 (\int_0^t v \cdot \delta F\ dt)^2\}^{1/2}$$

$$= \{v_{th}^2\ N_p (\int_0^t \delta F\ dt)^2\}^{1/2} = v_{th} <\delta F^2>^{1/2} (t\tau_c)^{1/2} , \qquad (3.2)$$

where v_{th} is the thermal velocity of the particle.

In order to evaluate the fluctuation in total energy both theoretically and experimentally, the following way is more convenient. Using the total energy

$$H = H_0 + K_g ,$$

we express the above consideration in a differential form:

$$dH / dt = A(t) \cdot H ,$$

where $A(t)$ is the fluctuated function of t. Its mean value is zero, and so the standard deviation $\sigma\{A(t)\}$ and the correlation time τ_c of $A(t)$ are characteristic quantities. Namely, the evaluation of $\sigma\{K_g\}$ in t is reduced to computation of $\sigma\{A(t)\}$ and τ_c.

Lewis *et al.* also investigated the fluctuation in total energy concerning a periodic, one-dimensional electron plasma [6, 11]. Using a definition of error of total energy:

$$\Delta H = (H_{max} - H_{min}) / (H_{max} + H_{min}) ,$$

they experimentally obtained a relation concerning it:

$$\Delta H \propto 1 / (n_s \lambda_D) ,$$

where n_s is the electron density and λ_D is the Debye length.

Our interests are focused on the problem of how much the spatial interpolation of each model influences the fluctuation of total energy. For convenience, we utilize the Fourier transform in order to solve the Poisson equation, and adopt the sharp-cutoff cloud [4] as the gridless shape factor throughout this work.

In Section 3.2, we derive $\sigma\{A(t)\}$, applying the one-dimensional periodic system of plasma as a test problem. In Section 3.3, we measure $\sigma\{A(t)\}$ in actual simulations and compare it with the above estimation. As to the correlation time τ_c, we discuss it qualitatively. Experimentally, we calculate the autocorrelation function and measure the correlation time. The results verify the above discussion.

3.2 THE FLUCTUATION IN TOTAL ENERGY

3.2-1 The basic equations of the gridless finite-sized particle plasma

We consider a periodic one-dimensional system which is composed of two species of N ions and N electrons. Each species has the equal magnitude of the charge and the system is neutral. The mass and charge densities per unit area of the ith particle are m_i and e_i, respectively. Following References [4, 5], we adopt $S(x)$ as the shape factor of the clouds (finite-sized particles). Then the kinetic equations of the particles are

$$dx_i / dt = v_i , \qquad m_i dv_i / dt = F_i , \tag{3.4}$$

$$F_i = e_i \int_0^L S(x - x_i)\, E(x)\, dx , \tag{3.5}$$

where L is a period. The electrostatic field is given by

$$E = - d\phi / dx, \qquad d^2\phi / dx^2 = - 1 / \epsilon_0 \sum_{i=1}^{2N} e_i S(x - x_i) \tag{3.6}$$

The total energy H, which is an invariant of the system, is the sum of the kinetic energy K and the field energy W,

$$H = K + W = \sum_{i=1}^{2N} \left\{ \frac{1}{2} m_i v_i^2 + \frac{1}{2} e_i \int_0^L \phi(x)\, S(x - x_i)\, dx \right\} . \tag{3.7}$$

The shape factor $S(x)$ can be expanded to the Fourier series from the periodic condition and is an even function of x due to the symmetry of space,

$$S(x) = \frac{1}{L} \sum_{m=0}^{M_c} S_m \cos 2\pi m x / L , \tag{3.8}$$

where the coefficient S_m should be satisfied with the normalizing condition and M_c corresponds to the maximum mode number in the system.

3.2-2 Interpolation of the shape factor

When we solve the above equation using the digital computer, we commonly introduce the spatial grids in order to save the computer time. We obtain the field quantities at the grid points and with them interpolate the quantities at other points. The shape factor $S(x-x_i)$ for the particle position x_i is approximated to a function $S_g(x, x_i)$, which is a linear combi-

nation of $S(x-x_{i0\pm l})$, where $x_{i0\pm l}$ are n nearest grid points of x_i ($l=0, \ldots, n/2$ for $n=even$ or $(n-1)/2$ for $n=odd$). The total energy H cannot, however, be conserved in the usual models, because S_g loses the property of the spatial uniformity owing to this approximation. This is the essential cause of the numerical error, if the particles per one Debye length are few. Accordingly, the choice of S_g has been an important problem. Here we analyze the properties of the approximated shape factor S_g of CIC-PIC ($n=2$) [2, 3], method 2/2 ($n=3$) [6], and modified SUDS ($n=3$) [7] in order to estimate the errors of the conserved quantities.

The system is assumed to have $2M$ grids. Then the grid distance Δ and the normalized grid distance Δ_0 are

$$\Delta = L / 2M, \qquad \Delta_0 = \pi / M. \tag{3.9}$$

Generally M is equal to or greater than M_c. The case of $M > M_c$ is equivalent to the higher-mode-cutoff method [8].

Next we define x_{i0} as $x_i = x_{i0} + \delta_i$, where δ_i is measured from the grid points,

$$x_{i0} = [\, x_i / \Delta \,] \times \Delta \qquad \text{for } n = even, \tag{3.10a}$$

$$x_{i0} = [\, x_i / \Delta + 0.5 \,] \times \Delta \qquad \text{for } n = odd, \tag{3.10b}$$

where the square brackets denote the Gauss symbol. Then the approximated shape factor $S_g^{(n)}$ is written in the forms:

Interpolation with the values at two grid points

$$S_g^{(2)}(x, x_i) = (1 - \delta_i / \Delta) \cdot S(x - x_{i0}) + (\delta_i / \Delta) \cdot S(x - x_{i0+1}), \tag{3.11}$$

Interpolation with the values at three grid points

$$S_g^{(3)}(x, x_i) = w_{-1} S(x - x_{i0-1}) + w_0 S(x - x_{i0}) + w_{+1} S(x - x_{i0+1}), \tag{3.12}$$

where w_i is a weight of the interpolation, which is the polynomial of δ_i. The slight modification of the above equation is necessary at the end points of the system, by considering the periodic condition.

As a method of determining w_i, we attempt to set S_g well approximated to S in the lower modes, which dominate the collective motions of the plasma. In other words, we determine w_i so that the difference $S - S_g^{(3)}$ is $O(\Delta^3)$ except for $\delta_i = \pm\Delta/2$. In this case, however, the weight function of this method has discontinuities similar to the dipole approximation [7]. As is pointed out [7, 12], these discontinuities enhance the error of total energy. In actual simulations we verified that the error in this method is larger than in CIC-PIC, except for $M_c < 1/4\ M$ (strong higher-mode cutoff). Accordingly, we obtain w_i from the condition that

the differences $S-S_g^{(3)}$ is $O(\Delta^2)$ as in CIC-PIC and that the weight function is continuous (Appendix 3.A) as follows.

$$\{w_{-1}, w_0, w_{+1}\} = \{-(1-2\gamma)(\delta_i/\Delta)^2 - (\delta_i/\Delta)/2 + (1-\gamma)/2,$$

$$(2-4\gamma)(\delta_i/\Delta)^2 + \gamma, -(1-2\gamma)(\delta_i/\Delta)^2 + (\delta_i/\Delta)/2 + (1-\gamma)/2\}, \quad (3.13)$$

where γ is an arbitrary constant, the magnitude of which considerably varies the properties of the model. The following two values have the distinguishing features:

$\gamma = 0.50$: Quadric terms vanish to be reduced to a linear interpolation. It is equivalent to modified SUDS.

$\gamma = 0.75$: The weight function is continuous to the first derivative. It is equivalent to method 2/2.

These shape factors S_g are satisfied with the conditions required for the shape factor, except for the uniformity of space.

3.2–3 Interparticle forces and momentum conservations

Lewis *et al.* derive the interparticle force for each of their models and prove the momentum conservation for the CIC-PIC (method 1/1) [6]. Here we represent the interparticle force in the case of systems where all variable quantities are expanded to the Fourier series or an eigenfunction of the system.

The force $F_j^{(n)}$ acting on the jth particle can be expressed in the form

$$F_j^{(n)} = \sum_{i=1}^{2N} F_{j,i}^{(n)} = \frac{e_j}{4\pi\epsilon_0} \sum_{i=1}^{2N} e_i \sum_{m=1}^{M_c} \frac{S_m^2}{m} \{ f_{s,m}^{(n)}(\delta_i, \delta_j) \sin mk\Delta_0 + f_{c,m}^{(n)}(\delta_i, \delta_j) \cos mk\Delta_0 \}, \quad (3.14)$$

where

$$k = (x_{j0} - x_{i0})/\Delta, \quad (3.15)$$

$f_{s,m}^{(n)}$ *Symmetrical polynomials of* δ_i *and* δ_j,

$f_{c,m}^{(n)}$ *Alternating polynomials of* δ_i *and* δ_j.

As in the results of Lewis *et al.*, the self-force $F_{i,i}^{(n)}$ vanishes and the total momentum is con-

served exactly because $F_{i,j}^{(n)} = -F_{j,i}^{(n)}$

The concrete expressions of $f_{s,m}^{(n)}$ and $f_{c,m}^{(n)}$ are obtained by replacing S with S_g in Eqs. (3.5) and (3.6) as follows:

$$f_{s,m}^{(2)} = \{ 1 - (\delta_i + \delta_j)/\Delta + 2\delta_i\delta_j/\Delta^2 \} (1 - \cos m\Delta_0) + \cos m\Delta_0 \quad , \tag{3.16a}$$

$$f_{c,m}^{(2)} = \{ (\delta_j - \delta_i)/\Delta \} \sin m\Delta_0 \quad , \tag{3.16b}$$

$$\begin{aligned} f_{s,m}^{(3)} &= (1-2\gamma)^2 (6 - 8\cos m\Delta_0 + 2\cos 2m\Delta_0)\, \delta_i^2 \delta_j^2 / \Delta^4 \\ &+ (1-2\gamma) \{ (3\gamma - 1) - 2(2\gamma - 1)\cos m\Delta_0 + (\gamma - 1)\cos 2m\Delta_0 \} (\delta_i^2 + \delta_j^2)/\Delta^2 \\ &+ 0.5(3\gamma^2 - 2\gamma + 1) + 2\gamma(1-\gamma)\cos m\Delta_0 + 0.5(1-\gamma)^2 \cos 2m\Delta_0 \\ &+ 0.5(1 - \cos 2m\Delta_0)\, \delta_i\delta_j/\Delta^2 \quad , \end{aligned} \tag{3.16c}$$

$$\begin{aligned} f_{c,m}^{(3)} &= (\delta_j - \delta_i)/\Delta \times \{ (4\gamma - 2)(\sin m\Delta_0 - 0.5 \sin 2m\Delta_0)\, \delta_i\delta_j/\Delta^2 \\ &+ \gamma \sin m\Delta_0 - 0.5(\gamma - 1)\sin 2m\Delta_0 \} \end{aligned} \tag{3.16d}$$

3.2–4 An evaluation of the fluctuation in total energy

For the usual models in which the total momentum is exactly conserved, the error of total energy is inevitable, even if the time integral is calculated exactly. Here we consider the properties of the error of total energy and estimate the magnitude of it. An origin of the error is that the approximated shape factor S_g loses the uniformity of space or does not depend only on $x - x_i$. In other words, it is considered that the spatial grids exert the unphysical forces on the particle in the system [8]. We assume this unphysical grid force $\delta F_j^{(n)}$ as the difference between the force F_j^* acting on the shape factor S^*, which has the uniformity of space, and the force $F_j^{(n)}$ acting on the approximated shape factor $S_g^{(n)}$:

$$\begin{aligned} \delta F_j^{(n)} = F_j^{(n)} - F_j^* = \frac{e_j}{4\pi\epsilon_0} \sum_{i=1}^{2N} e_i \sum_{m=1}^{M_c} \frac{S_m^2}{m} \Big[\\ \{ f_{s,m}^{(n)}(\delta_i, \delta_j) - \kappa_m^{(n)} \cos \frac{2\pi m}{L} (\delta_j - \delta_i) \} \sin mk\Delta_0 \\ + \{ f_{c,m}^{(n)}(\delta_i, \delta_j) - \kappa_m^{(n)} \sin \frac{2\pi m}{L} (\delta_j - \delta_i) \} \cos mk\Delta_0 \Big] \quad , \end{aligned} \tag{3.17}$$

where F_j^* is not equal to the force F_j acting on the shape factor S generally, because S_g approximates S well in the lower modes but not in the higher modes at all. Accordingly, $\kappa_m^{(n)}$ are correction factors caused by the interpolation, which converge to unity as m decreases. The unphysical energy K_g which flows in or out the system is given by

$$dK_g^{(n)} / dt = \sum_{j=1}^{2N} v_j \, \delta F_j^{(n)} \ , \tag{3.18}$$

where we assume that time is continuous. The effects of the finite time step are discussed in Section 3.3. Although $F_j^{(n)}$ is determined by the kinetic equation which obeys the law of causality, $\delta F_j^{(n)}$ can be considered as a random noise which is almost independent of the history of the system. So the unphysical kinetic energy K_g is evaluated statistically on some assumptions.

In the case of the sufficiently small error, the mean value of dK_g/dt is equal to zero and so the standard deviation, $\sigma\{ dK_g/dt \}$, and the correlation time, τ_c, are the quantities required for the evaluation of K_g, where τ_c is a characteristic time during which dK_g/dt varies. Then K_g is obtained statistically at time t. If the error is sufficiently small and t is not long, the random noise theory [13] shows that the mean value of K_g equals zero and the standard deviation $\sigma\{ K_g \}$ is

$$\sigma\{ K_g \} \simeq \sigma\{ dK_g / dt \} \, (t\tau_c)^{1/2}. \tag{3.19}$$

Next we evaluate $\sigma\{ dK_g/dt \}$ on the following assumptions.

(a) The particles are distributed at random.

(b) The correlation between the unphysical force $\delta F_j^{(n)}$ and the particle velocity v_j does not exist.

(c) The correlations between δ_i, δ_j, and $k\{ = (x_{j0} - x_{i0}) / \Delta \}$ do not exist.

These assumptions do not involve the effects of the properties of the plasma such as the Debye shielding, the particle-bunching by the potential fluctuations, and so on. Although these effects influence the evaluation of $\sigma\{ dK_g^{(n)} / dt \}$, these assumptions are almost correct in the limit of the small fluctuation energy. On the above assumptions, probabilities $p(\delta_i)$ and $q(k)$ are calculated as follows (Appendix 3.B):

$$p(\delta_i) = 1 / \Delta \ , \qquad q(k) = (M - |k|) / M^2 \tag{3.20}$$

Next we define the fluctuating kinetic energy $K_{g,l}^{(n)}$ which is sampled at time t_l. Then the square of the standard deviation $\sigma\{ dK_g^{(n)} / dt \}$ is

$$\sigma^2\{ dK_g^{(n)} / dt \} = \frac{1}{l_s} \sum_{l=1}^{l_s} (dK_{g,l}^{(n)} / dt)^2$$

$$= \frac{1}{l_s} \sum_{l=1}^{l_s} \{ \sum_{j=1}^{2N} v_j^2 (\delta F_j^{(n)})^2 + \sum_{i \neq j}^{2N} v_i v_j \, \delta F_i^{(n)} \delta F_j^{(n)} \}_l \ , \tag{3.21}$$

where l_s is the number of the samples, which are assumed sufficiently large. In the following we eliminate the subscript l and the notation $(1/l_s) \sum_{l=1}^{l_s}$ in order to avoid complicated expressions. Assumption (b) suggests that the second term of Eq. (3.21) vanishes. Accordingly we get an approximation

$$\sigma^2 \{ dK_g^{(n)} / dt \} = \sum_{j=1}^{2N} v_j^2 (\delta F_j^{(n)})^2 = \langle v_j^2 \rangle \sum_{j=1}^{2N} (\delta F_j^{(n)})^2 \ , \tag{3.22}$$

where the angle brackets show the average for the particles. Namely, we conclude that $\sigma^2 \{ dK_g^{(n)} / dt \}$ is a product of the random force fluctuation of square magnitude, $\sum_{j=1}^{2N} (\delta F_j^{(n)})^2$, and the average of the square of velocity $\langle v_j^2 \rangle$, as discussed in Section 3.1. The detailed derivation of $\sum_{j=1}^{2N} (\delta F_j^{(n)})^2$ is shown in Appendix 3.C.

Using the subscripts i and e to denote quantities associated with the ion and electron, we obtain

$$\sigma \{ \frac{dK_g^{(n)}}{Kdt} \} = \frac{1}{\sqrt{\pi}} \omega_p^2 \frac{1}{\sqrt{M}} \frac{1}{N/L} \frac{(\langle v_i^2 \rangle + \langle v_e^2 \rangle)^{1/2}}{\frac{m_i}{\mu} \langle v_i^2 \rangle + \frac{m_e}{\mu} \langle v_e^2 \rangle} \cdot \eta^{(n)} (\frac{M_c}{M}) \ , \tag{3.23}$$

where

$$\omega_p^2 = \frac{e^2 N}{\epsilon_0 \mu L} = (1/m_i + 1/m_e) \frac{Ne^2}{\epsilon_0 L} \ , \tag{3.24}$$

$$\eta^{(2)} (M_c / M) = [\int_0^{\frac{M_c}{M}\pi} dx \ (\frac{S_{x/\Delta}^4}{4x^2}) \{ \kappa_{x/\Delta}^2 + \frac{4}{9} + \frac{4}{9} \cos x + \frac{1}{9} \cos^2 x - \frac{8 \kappa_{x/\Delta}}{x^4} (1 - \cos x)^2 \}]^{1/2} \ , \tag{3.25}$$

where $S_{x/\Delta}$ and $\kappa_{x/\Delta}$ are the smooth functions of x, which are equal to S_m and $\kappa_m^{(n)}$, when $x/\Delta = m$, respectively. The proportional coefficient $\eta^{(3)}$ is too complex to be presented here, although it can be calculated analytically. Therefore, we show the numerical results later. In order to clarify the scaling law about the fluctuation in total energy, we neglect the terms for the ion:

$$\sigma \{ \frac{dK_g^{(n)}}{K \, d(\omega_p t)} \} \simeq \frac{1}{\sqrt{\pi}} \frac{1}{\sqrt{M}} \frac{1}{n_s \lambda_D} \cdot \eta^{(n)} (\frac{M_c}{M}) \ . \tag{3.26}$$

From the experimental results, Lewis *et al.* indicated that the fluctuation is approximately proportional to $(n_s \lambda_D)^{-1}$ for $\Delta / \lambda_D = 1$ [6]. Our evaluation supports their empirical law.

Generally it is proportional to $[(2M)^{1/2} \cdot n_s \cdot \lambda_D]^{-1}$ for all usual models. The coefficient $\eta^{(n)}$ involves the unknown factor $\kappa_m^{(n)}$, which depends on each model.

3.2–5 Determination of the unphysical grid force or $\kappa_m^{(n)}$

The gridded systems with the shape factor $S_g^{(n)}$ are similar to the gridless systems with the shape factor S^* about the physical properties, whether they have the uniformity of space or not. Therefore, we study the fluctuation spectrum of the electric field. In the gridless system, the fluctuation spectrum of the thermal equilibrium state, $<\epsilon_0 E_m{}^2>$ [4, 5] is

$$<\epsilon_0 E_m{}^2> = \frac{m_e <v_e{}^2>}{L} \frac{(S_m^*/2)^2}{(S_m^*/2)^2 + (k_m \lambda_D)^2} , \tag{3.27}$$

where $k_m = 2\pi m / L$ and $\lambda_D^2 = 1/2 \cdot \epsilon_0 m_e <v_e^2> / n_s e^2 = 1/2 \cdot \epsilon_0 m_i <v_i^2> / n_s e^2$. In the gridded system, the problem is more difficult [10]. When the Debye shielding effect can be neglected or the particles are distributed at random in space, however, we calculate it as well as the evaluation of $\sigma\{dK_g^{(n)}/dt\}$ as follows.

$$<\epsilon_0 E_m{}^2> = \frac{2}{L} \frac{\mu \omega_p{}^2}{k_m{}^2} \xi_m^{(n)} (S_m/2)^2 , \tag{3.28}$$

where

$$\xi_m^{(2)} = 2/3 + 1/3 \cos m\Delta_0 , \tag{3.29a}$$

$$\xi_m^{(3)} = (2-4\gamma)^2 (1-\cos m\Delta_0)^2 / 12 + (2-4\gamma)(1-\cos m\Delta_0) \times \{\gamma + (1-\gamma)\cos m\Delta_0\}/2 + \{\gamma + (1-\gamma)\cos m\Delta_0\}^2 + \sin^2 m\Delta_0 / 12 . \tag{3.29b}$$

When λ_D is sufficiently large, Eq. (3.27) can be set equal to Eq. (3.28). As a result, we conclude the following:

$$\kappa_m^{(n)} = \{\xi_m^{(n)}\}^{1/2} . \tag{3.30}$$

In Fig. 3.1, we show $\eta^{(n)}(x)$, which is calculated from Eqs. (3.25) and (3.30).

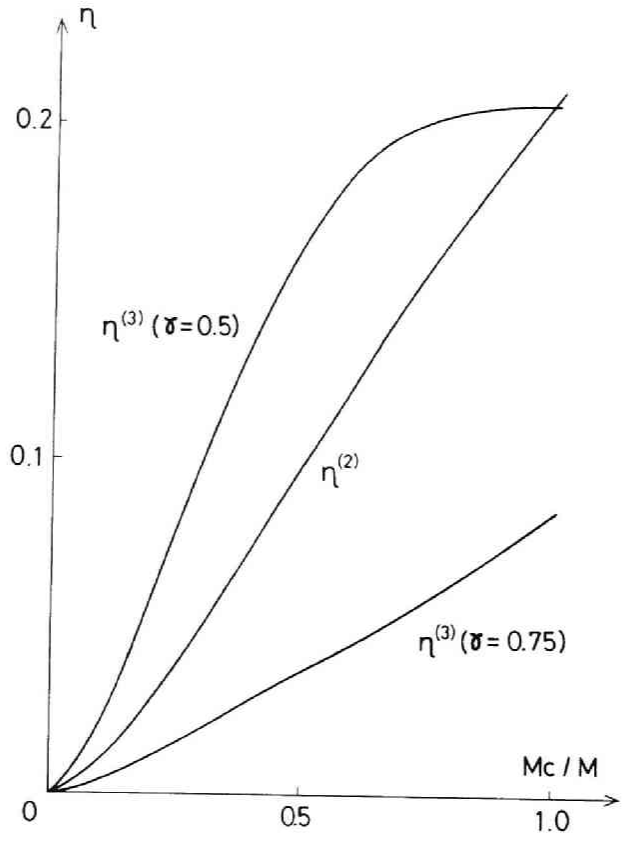

Fig. 3.1 $\eta^{(n)}$ vs M_c/M.

3.3 NUMERICAL RESULTS

We carried out numerical simulations of the system explained in Section 3.2 in order to verify the scaling law. Namely we measure the standard deviation $\sigma\{dH/Hdt\}$ and the correlation time τ_c, and compare the estimated value $\sigma\{dK_g/Kdt\}$ with the measured value $\sigma\{dH/Hdt\}$. These two values are expected to be approximately equal because the potential energy W is sufficiently smaller than the kinetic energy K. The algorithm for advancing particles is the standard time-centered leapfrog scheme and Eq. (3.6) is integrated by using the Fast Fourier Transform algorithm [9]. The total energy H is calculated by the use of the equation which is modified by replacing S by $S_g^{(n)}$ in Eq. (3.7). As the initial state of plasma, the electron-ion pairs are put uniformly in space and the particle velocities are selected independently from Maxwellian distributions. In spite of the special distribution of space at the

initial state, it is confirmed that $\sigma\{dH/Hdt\}$ measured per 40 steps is kept constant within a factor of 3 throughout each run. In order to avoid the spoilage of the estimation Eq. (3.23) caused by the round-off errors, all data are treated with the double precision (1 word = 72 bits). Note that the errors of total energy owing to the spatial interpolations are much greater even in the usual simulations calculated with the single precision than those owing to the round-off errors.

3.3–1 Comparison of the numerical results with the obtained scaling law

We change the differential equation, Eq. (3.3), into the difference equation

$$(H_{n+1} - H_n)/\Delta t = H_n A_n \ , \tag{3.31}$$

where H_n is the total energy at the nth step $(t = n \cdot \Delta t)$. Accordingly, we compute the statistical values about N_d data of the following h_n,

$$h_n = A_n \cdot \Delta t = H_{n+1}/H_n - 1 \qquad (n = 1, 2, 3, \ldots, N_d) \tag{3.32}$$

Then the standard deviation σ is calculated as

$$\sigma^2 = (1/N_d) \sum_{i=1}^{N_d} \{ h_i - (1/N_d) \sum_{j=1}^{N_d} h_j \}^2 \tag{3.33}$$

Using σ, we calculate the empirical value η_{emp} as follows,

$$\eta_{emp} = \frac{\sqrt{\pi}\,\sigma}{\omega_p{}^2 \Delta t} \frac{\sqrt{M} \cdot N}{L} \frac{(m_i/\mu) < v_i{}^2 > + (m_e/\mu) < v_e{}^2 >}{(< v_i{}^2 > + < v_e{}^2 >)^{1/2}} \ . \tag{3.34}$$

In the case of finite Δt, the autocorrelation function, $R(k \cdot \Delta t)$, is defined as

$$R(k \cdot \Delta t) = \frac{1}{N_d - k} \sum_{i=1}^{N_d - k} h_i \cdot h_{i+k} \qquad (k = 0, 1, 2, 3, \ldots) \ , \tag{3.35}$$

and the correlation time τ_c is calculated by assuming the Markoffian process [13].

As the simulation parameters, the following values are chosen:

$S_1 = 1$, $S_m = 2\,(m \geqq 1)$; $2M = 32 \sim 512$; $N = 160$, 320, and 640; $\lambda_D (L/2\pi)^{-1} = 0.05$, and 0.2; $< v_i{}^2 > / < v_e{}^2 > = 0.01$; $m_i/m_e = 25$; $\omega_p \cdot \Delta t = 0.2$, 0.1, 0.05, and 0.04; and $N_d \simeq 500$.

Figure 2 shows that η_{emp} keeps constant within a factor of 2, when σ varies between 10^{-2} and 10^{-4}. Therefore, it is experimentally confirmed that the scaling law, Eq. (3.23), holds good about the parameters $2M$, N, Δt, and $< v_e{}^2 >$.

Notice that Eq. (3.23) is obtained under the condition that time is continuous. So the

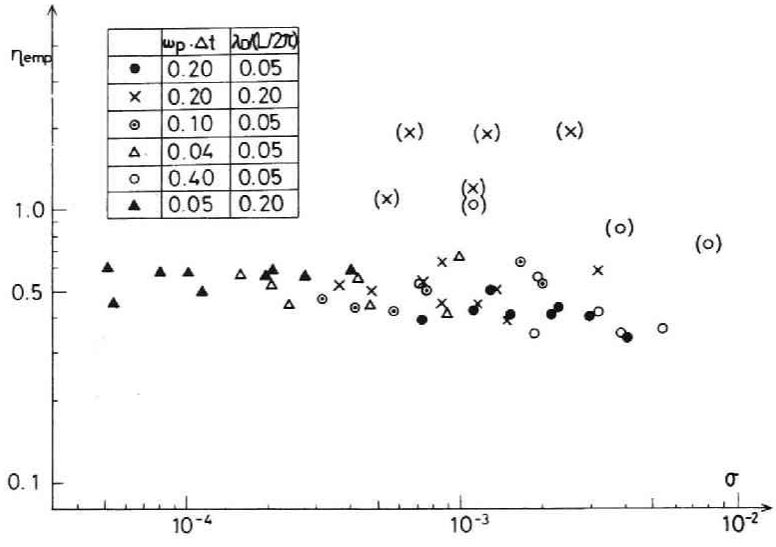

Fig. 3.2 η_{emp} vs σ for various parameters in CIC-PIC ($M_c = M$). The round brackets represent runs with the parameters: $\Delta t \cdot v_{th} > \Delta$, in which η_{emp} is greatly enhanced.

next condition that the fine variation of space is calculated smoothly in time should be required:

$$<v_e^2>^{1/2} \cdot \Delta t < \Delta. \tag{3.36}$$

Actually, if the above condition is not satisfied, η_{emp} is enhanced, as shown in Fig. 3.2. However, by setting Δt shorter or Δ longer and satisfying Eq. (3.32), η_{emp} can be reduced to the usual values.

Table 3.1 shows η_{emp} for each model in the case of $M_c/M = 1$ and $1/2$. The coefficient η_{emp} is reduced by 50% for CIC-PIC and method 2/2 but is reduced only 10% for modified SUDS, when the higher modes are cut off: $M_c/M = 1/2$.

TABLE 3.1 Comparisons between the Theoretical and Empirical Values of η

	$M_c/M = 1$		$M_c/M = 1/2$	
model	η_{emp}	η_{emp}/η	η_{emp}	η_{emp}/η
CIC-PIC	0.50	2.4	0.29	2.9
modified SUDS	0.26	1.3	0.23	1.4
method 2/2	0.14	1.6	0.06	1.6

3.3–2 A consideration about the correlation time and its measurements

As mentioned above, we replace the differential equations, Eq. (3.4), by difference equations in actual simulations. This means that the unphysical grid force $\delta F_j^{(n)}$ is kept constatnt during a time step Δt and the right-hand side of Eq. (3.18) is a step function of t. Accordingly, the correlation time τ_c is larger than Δt. If Δt is sufficiently large and the particle positions in one grid interval are randomized during one time step, τ_c is nearly equal to Δt. On the contrary, if Δt is sufficiently small and time is considered almost continuous, τ_c is expected to be proportional to Δ / v_{th} and is a characteristic time during which the particle distribution in one grid interval changes continuously.

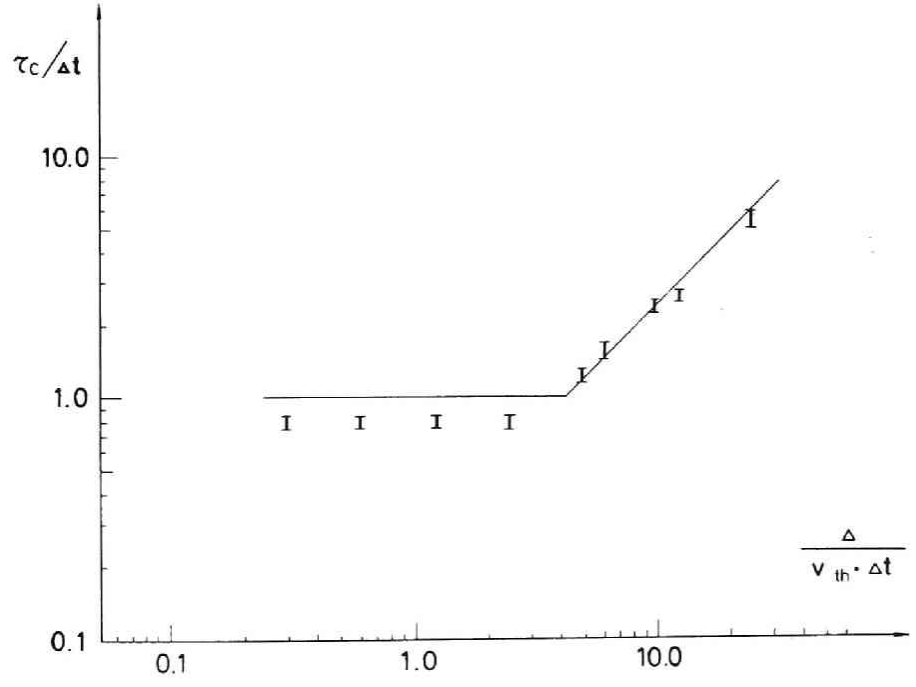

Fig. 3.3 $\tau_c / \Delta t$ vs $\Delta / (v_{th}\ \Delta t)$ in CIC-PIC. The simulation parameters of these runs have the same parameters as those in Fig. 3.2.

These features for the correlation time are presented in Fig. 3.3. It shows the dependence of $\tau_c / \Delta t$ on $\Delta / (\Delta t \cdot v_{th})$, which indicates how many time steps a thermal electron takes to pass one grid interval. If $\Delta / (\Delta t \cdot v_{th})$ is sufficiently small, τ_c is equal to Δt and is independent of the other parameters. When $\Delta / (\Delta t \cdot v_{th})$ is larger than 3, it increases linearly in $\Delta / (\Delta t \cdot v_{th})$. Namely, τ_c becomes independent of Δt and nearly equal to $1/4 \cdot \Delta / v_{th}$. From

the above results and Eq. (3.32), the optimum time step should be satisfied with the condition

$$0.3\ \Delta/v_{th} < \Delta t < \Delta/v_{th}$$

These results are consistent with Hockney's in [1, Eq. (12)] in the case of the Debye length larger than half of the grid distance, although his evaluation is concerned with the heating time.

3.4 DISCUSSIONS AND CONCLUSIONS

In Section 3.2, we introduced assumptions (a), (b), and (c) in order to evaluate the energy fluctuation statistically. In these assumptions the dynamical shielding effects of plasma are neglected. If the Debye length is sufficiently large, it is clear that these effects can be neglected. Judging from the properties of the fluctuation spectrum [see Eqs. (3.27) and (3.28)], we can expect that our scaling law will give the correct results, if Eq. (3.36) and the following condition are satisfied:

$$2\pi M_c > L\lambda_D^{-1} \tag{3.37}$$

Actually, we observed that the accuracy of the scaling law is rather poor when M_c is reduced to a parameter of $2\pi M_c \simeq 0.5 \cdot L\lambda_D^{-1}$

Concerning method 2/2 and modified SUDS, η_{emp} agrees with $\eta^{(3)}$ within a factor of 1.6. Especially, it is well explained that η_{emp} for $M_c/M = 1/2$ becomes smaller by only 10% than that for $M_c/M = 1$. However, η_{emp} in CIC-PIC is larger by a factor of 2.4 or 2.9 than $\eta^{(2)}$. We could not find the cause within the accuracy of this work. In order to improve the accuracy of the scaling law and the coefficient η, we should consider the dynamical effects of plasma and the error associated with the spatial interpolation of the scalar potential. If we adopt the empirical value for η, however, we believe that our scaling law holds within a factor of 2.

We discuss some applications of our work for other problems. It is well known that Eqs. (3.6) are solved by transforming them into difference equations. In this case our evaluation can be applied after slight modifications.

The scaling law about the heating time τ_c is calculated in the case of $2\pi M_c > L\lambda_D^{-1}$, because the random force fluctuation of square magnitude, $<\delta F^2>$, is obtained. From the definition of the heating time [1, 14] and Eq. (3. C−4), we obtain

$$\tau_H \propto \frac{1}{\eta^2 \tau_c \omega_p^2} \cdot \frac{\lambda_D}{\Delta} \cdot n_s \lambda_D \tag{3.38}$$

The above equation is consistent with the result which is reduced in the case of the one-dimensional system from the empirical result of Hockney *et al.* [1, 14] obtained in the case of the two-dimensional system.

Extensions to the two- or three-dimensional problem are possible for the usual models. Our considerations concerning the interpolation of the shape factor are generally applicable to the system with the more complex boundary conditions and curved spatial grids of the two- and three-dimensions.

Appendix 3.A: The determination of weights *(n=3)*

When $M_c \ll M$, the functions $S(x-x_{i0-1})$, $S(x-x_{i0})$, and $S(x-x_{i0+1})$ can be approximated by the Taylor expansion in the neighbourhood of $x-x_i$. From Eq. (3.12), we obtain

$$S_g^{(3)}(x, x_i) = (w_{-1} + w_0 + w_{+1}) \cdot S(x - x_i) - \{(\Delta + \delta_i) w_{-1} + \delta_i w_0 + (-\Delta + \delta_i) w_{+1}\} \cdot S'(x - x_i) + O(\Delta^2) , \quad (3.A-1)$$

where $S'(x)$ is $dS(x)/dx$. Therefore, we get

$$\left.\begin{aligned} w_{-1} + w_0 + w_{+1} &= 0 , \\ (\Delta + \delta_i) w_{-1} + \delta_i w_0 + (-\Delta + \delta_i) w_{+1} &= 0 \end{aligned}\right\} \quad (3.A-2)$$

In addition to the above conditions, we adopt the following condition that the weight function is continuous at $\delta_i = \pm \Delta/2$,

$$\left.\begin{aligned} w_{-1}(\delta_i = -\Delta/2) &= w_0 (\delta_i = +\Delta/2) , \\ w_{+1}(\delta_i = +\Delta/2) &= w_0 (\delta_i = -\Delta/2) . \end{aligned}\right\} \quad (3.A-3)$$

Assuming w_i as a quadric polynomial of δ_i and solving Eqs. (3.A–2) and (3.A–3), we obtain Eq. (3.13), which involves the arbitrary constant γ.

When M_c is nearly equal to M, we extend the above definition and use these weights. So one should take notice that $S_g^{(n)}$ never becomes the approximation of S in higher modes.

Appendix 3.B: The probability of the grid differences of pair-particles, *q(k)*

The section of length L is divided to $2M$ cells. Assume that these cells are numbered from 1 to $2M$ and that the particles are distributed uniformly in each cell. In order to simplify the consideration, we assume that the number of particles in a cell is infinite. When a pair of particles are taken at random, one particle is extracted from the i-th cell, and the other from j-th cell. Then we determine k as $k=j-i$ for a set of the pair particles (i,j). Sets (i,j), in which k equals $k_1 (>0)$, are restricted to the following $M-k_1$ cases:

$$(M, M-k_1),\ (M-1, M-k_1-1),\ (M-2, M-k_1-2), \ldots,\ (k_1+1, 1)\ .$$

Considering that the probability $q(k)$ is an even function of k, we obtain

$$q(k) = (M - |k|)/M^2\ . \tag{3.B-1}$$

Appendix 3.C: The derivation of $\sum_{j=1}^{2N} (\delta F_j^{(n)})^2$

We rewrite Eq. (3.17) for simplicity in the form

$$\delta F_j^{(n)} = \frac{e_j}{4\pi\epsilon_0} \sum_{i=1}^{2N} e_i \sum_{m=1}^{M_c} (g_{s,m}^{(n)} \sin mk\Delta_0 + g_{c,m}^{(n)} \cos mk\Delta_0)\ , \tag{3.C-1}$$

where

$$g_{s,m}^{(n)}(\delta_i, \delta_j) = \frac{S_m^2}{m} \{ f_{s,m}^{(n)}(\delta_i, \delta_j) - \kappa_m^{(n)} \cos \frac{2\pi m}{L} (\delta_j - \delta_i) \}\ ,$$

$$g_{c,m}^{(n)}(\delta_i, \delta_j) = \frac{S_m^2}{m} \{ f_{c,m}^{(n)}(\delta_i, \delta_j) - \kappa_m^{(n)} \sin \frac{2\pi m}{L} (\delta_j - \delta_i) \}$$

Like the derivation of Eq. (3.22), averaging over the samples lets the cross terms cancel and yields $\sum_{j=1}^{2N} (\delta F_j^{(n)})^2$ in the form

$$\sum_{j=1}^{2N} (\delta F_j^{(n)})^2 = \sum_{j=1}^{2N} (\frac{e_j}{4\pi\epsilon_0})^2 \sum_{i=1}^{2N} e_i^2 \sum_{m=1}^{M_c} (g_{s,m}^{(n)} \sin mk\Delta_0 + g_{c,m}^{(n)} \cos mk\Delta_0)^2\ . \tag{3.C-2}$$

Considering assumption (c), we introduce the probabilities $P(\delta_i)$ and $q(k)$ [Eq. (3.20)], and replace the summation of i, j, and k by integrations:

$$\sum_{j=1}^{2N} (\delta F_j^{(n)})^2 = (\frac{2Ne^2}{4\pi\epsilon_0})^2 \sum_{m=1}^{M_c} (\mathcal{G}_{s,m}^2 + \mathcal{G}_{c,m}^2)/2, \tag{3.C-3}$$

where the notation $\tilde{g}^2$ denotes the integration

$$\int_a^b \int_a^b g^2 p(\delta_i) p(\delta_j)\, d\delta_i d\delta_j \ ,$$

$$\left[\begin{array}{lll} a = 0 \ , & b = \Delta & \text{for } n = even ; \\ a = -\Delta/2 \ , & b = \Delta/2 & \text{for } n = odd \ . \end{array} \right]$$

Replacing the summation of m by an integration yeilds the numerical factor $\eta^{(n)}$ of Eq. (3.23), and the random force fluctuation of square magnitude is obtained as follows;

$$\sum_{j=1}^{2N} (\delta F_j^{(n)})^2 = \frac{1}{\pi} \frac{\mu^2 L^2}{2M} \omega_p{}^4 \cdot \{ \eta^{(n)} (\frac{M_c}{M}) \}^2 \ . \qquad (3.C\text{–}4)$$

REFERENCES

1. R. W. Hockney: J. Computational Phys. 8 (1971) 19.
2. R. L. Morse and C. W. Nielson: Phys. Fluids 12 (1969) 2418.
3. C. K. Birdsall and D. Fuss: J. Computational Phys. 3 (1969) 494.
4. A. B. Langdon and C. K. Birdsall: Phys. Fluids 13 (1970) 2115.
5. H. Okuda and C. K. Birdsall: Phys. Fluids 13 (1970) 2123.
6. H. R. Lewis, A. Sykes, and J. A. Wesson: J. Computational Phys. 10 (1972) 85.
7. W. L. Kruer, J. M. Dawson, and B. Rosen: J. Computational Phys. 13 (1973) 114.
8. A. B. Langdon: J. Computational Phys. 6 (1970) 247.
9. R. C. Singleton: Comm. ACM 11 (1968) 773.
10. A. B. Langdon: in *"Proceedings of the Fourth Annual Conference on Numerical simulations of Plasmas"* U. S. Government Printing Office, Washington, D. C. 20402, Stock No. 08510059.
11. D. I. Brown, S. J. Gitomer, and H. R. Lewis: J. Computational Phys. 14 (1974) 193.
12. A. B. Langdon: J. Computational Phys. 12 (1973) 247.
13. S. Chandrasekhar: *"Reviews of Modern Physics"* Vol. 15, Dover, New York (1954).
14. R. W. Hockney, S. P. Goel, and J. W. Eastwood: J. Computational Phys. 14 (1974) 148.

CHAPTER 4

COMPUTER SIMULATION OF CONTAINMENT OF ELECTRON CLOUDS IN A TOROIDAL MAGNETIC FIELD

1. INTRODUCTION

Many works have been performed experimentally [1–4] and theoretically [5–9] for the problem of how long unneutralized clouds of electrons can be quiescently confined by the toroidal magnetic field. From a practical point of view, it is unfavourable for devising a new application that these apparatuses should be low-density machines ($q = \omega_p^2 / \omega_c^2 << 1$) due to the equilibrium and stability conditions [2, 5, 7]. In the toroidal systems, Daugherty and Levy [5] theoretically derived the necessary conditions, with which the density profile in the equilibrium should be satisfied in the case of small q ($\simeq 0.001$), and obtained the guiding center orbits of electrons. A theoretical evidence [7] indicates that the magnetron instability would be significant when q is greater than 0.05. Taking these physical and technical conditions into consideration, Janes *et al.* [2] inferred that q would be restricted from 0.001 to 0.05.

The experiments are restricted by the techniques concerning various diagnostics and plasma productions, although many experimental attempts [3, 4] are made. For example, the direct measurement of electrostatic potentials by voltage probes [3] has become impossible in the electron densities over 4×10^9 cm^{-3}. It has been also an important experimental problem to produce a quiescent plasma with the maximum of q, which is limited due to the presence of the equilibrium and stability conditions. By means of the inductive charging scheme, with which the electron clouds in the quiescent equilibrium can be produced, Daugherty *et al.* [3] achieved the value of $q \lesssim 0.02$ in the uncompressed density. Although they have predicted a possibility of improvement of raising q, however, they could not exceed this value from the limitation of ability of the electron injection system rather than from the equilibrium and

stability conditions. Mohri *et al.* [4] produced a quiescent plasma with the relativistic-electron-beam source (Phoebus–I) by applying an appropriate vertical magnetic field. In this scheme, also, when they tried to raise the beam current or the electron density by increasing the vertical field, a fluctuation appeared in spite of sufficiently small q. Though these extensive works have been done, a problem of how large the ratio q can be in the toroidal systems still remains.

In view of the lack of the more complete experimental study of the confinement, it appears to be worthwhile to apply the methods of the computer simulation. As the simulation model, CIC [10] is adopted in this work. The principal aims of the present work have been to study the following problems:

(1) an evidence of the equilibrium theory developed by Daugherty and Levy [5]: The electrostatic potentials measured in the simulation runs are compared with the theoretical values.

(2) How large the ratio q can be for the quiescent equilibrium.

(3) The measurements of the potential fluctuations, the kinetic energy of the electrons, and the particle decay time.

(4) a study of effects due to the differences of initial conditions of plasmas.

A model and numerical techniques are presented in Section 4.2, and the equilibrium theory developed by Daugherty and Levy [5] is applied to this model in Section 4.3. In Section 4.4, we present the results of numerical runs with characteristic parameters and compare them with the results obtained in Section 4.3.

4.2 THE MODEL AND NUMERICAL TECHNIQUES

The model in this paper is intended to be representative of some of the apparatuses [3, 4] which have been actually constructed and studied experimentally. It consists of a perfectly conducting toroidal vessel, of minor radius a and major radius R, having a toroidal magnetic field; and containing a nonneutral cloud of electrons and ions. We assume that the effect of current in the plasma on the applied magnetic field is negligible (quasistatic approximation), and that all quantities are azimuthally symmetric.

In order to compute them numerically, we introduce two coordinate systems, which are taken to be curved coordinate systems centered about the minor axis. These curvilinear coordinates $r = (r, \theta, z)$ and $r = (x, y, z)$ are well explained in References [11, 12] and [13], re-

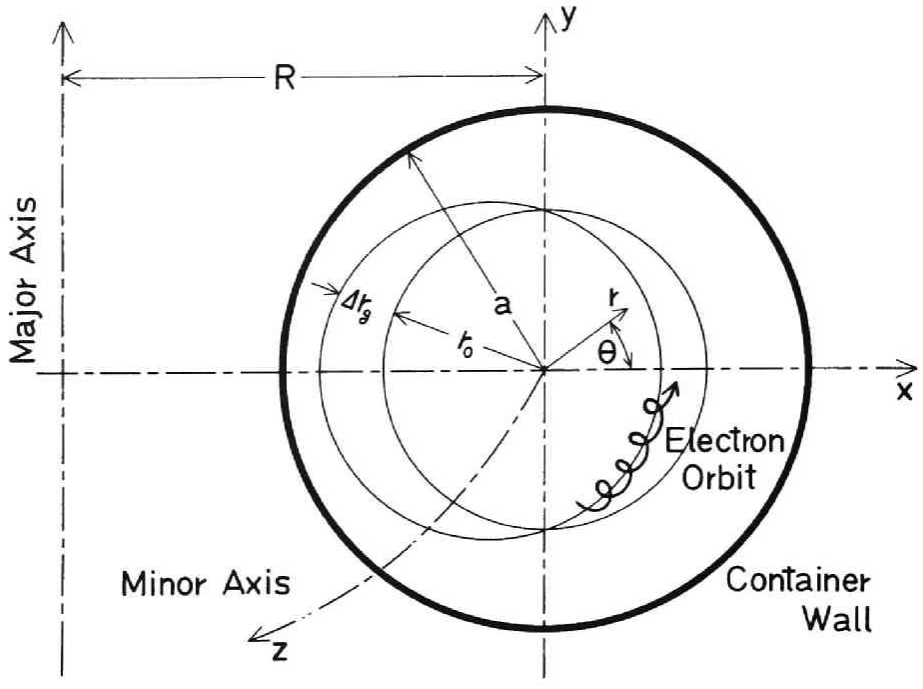

Fig. 4.1 Schematic representation of the cross section of the apparatus considered in this text.

spectively. When the major radius R is set infinite, these coordinates are reduced to the usual cylindrical and cartesian coordinates. We properly use these two coordinate systems from a viewpoint of convenience associated with the numerical computations. Namely, we use (x, y, z) for the motion of the particle and (r, θ, z) for the equation on the electrostatic field, respectively.

The toroidal magnetic field with the magnitude at the major radius of the torus, B_0, is given by

$$\boldsymbol{B} = B_0 \,/\, (1 + x/R) \cdot \hat{z} \tag{4.1}$$

As the motion of a charged particle in this system lets the angular momentum be conserved because of the azimuthal symmetry, the equations of motion of the particle with mass m_α and charge e_α are given by the following equations:

$$m_\alpha \frac{d^2x}{dt^2} = \frac{m_\alpha v_z^2}{R+x} + e_\alpha B_0 \frac{dy/dt}{1+x/R} + e_\alpha E_x \quad , \tag{4.2a}$$

$$m_\alpha \frac{d^2y}{dt^2} = - e_\alpha B_0 \frac{dx/dt}{1 + x/R} + e_\alpha E_y \ , \tag{4.2b}$$

$$P_z = m_\alpha R (1 + x/R) \cdot v_z = const. \ , \tag{4.2c}$$

where the subscript α denotes a species (e: electron or i: ion) and we assume that e_i is equal to $-e_e$. The 1st term of the righthand side in Eq. (4.2a) is a centrifugal force associated with toroidicity. Numerically, Eq. (4.2) is solved by the time-centered, reversible leapfrog scheme [14].

The electrostatic potential ϕ is obtained in a self-consistent manner from the evolving charge distribution through Poisson's equation,

$$\Delta\phi = -1/\epsilon_0 \cdot \rho, \qquad E = -\nabla\phi \ , \tag{4.3a}$$

$$\rho(r, \theta) = \sum_{\alpha}^{e, i} \sum_{j=1}^{N_\alpha} P_\alpha e_\alpha S(r, r_{\alpha j}, \theta, \theta_{\alpha j}) \ , \tag{4.3b}$$

$$\phi = 0 \quad \text{at} \quad r = a, \tag{4.3c}$$

where N_α is the number of particles in the container, P_α is the density, and $S(r, r_j, \theta, \theta_j)$ is the shape factor which gives the charge distribution of a finite-sized particle [15, 16] centered at (r_j, θ_j). As a shape factor, we choose the following:

$$S(r, r_j, \theta, \theta_j) = \frac{1}{a^2 (1 + \epsilon r/a \cdot \cos\theta)\pi} \sum_{l=0}^{l_c} \sum_{n=1}^{n_c} \frac{\gamma_l}{\{J_{l+1}(\lambda_{ln})\}^2} \cdot$$

$$J_l(\lambda_{ln} r/a) \cdot J_l(\lambda_{ln} r_j/a) \cdot \cos l(\theta - \theta_j) \ , \tag{4.4}$$

where $\epsilon = a/R$, $J_l(x)$ are Bessel's functions of the lth order, λ_{ln} are successive positive roots of the equation $J_l(\lambda_{ln}) = 0$ $(\lambda_{l1} < \lambda_{l2} < ...)$ and $\gamma_0 = 1$, $\gamma_1 = \gamma_2 = \cdots\cdots = 2$. When both l_c and n_c become infinite, S is reduced to a δ-function. A few modifications of the method of Smith and Bishop [12] give a procedure to solve the above equations numerically, which is explained by two steps:

(1) A l by n grid, at which the charge density ρ is sampled, is determined to establish a uniform grid in the (r^2, θ) plane so that the cells are of equal weight. Concerning the spatial interpolation of the shape factor S or the numerical computation of the charge distribution at the grid points, we apply the method [17], which is equivalent to CIC-PIC for a one-dimensional system with the periodic boundary condition, to the present case: the two-dimensional system with the curved spatial grids.

(2) The thin tube limit permits the potential to be solved in powers of ϵ [12, 13, 19] and to give the analytical solution of Poisson's equation, which is calculated exactly to the 1st order of ϵ. In order to improve the accuracy of the conservation of total energy, we adopt the strong higher-mode-cutoff method [17] or a parameter of $l >> l_c$ and $n >> n_c$.

The vessel wall at $r = a$ acts as an absorber: particles reaching $r = a$ are removed from the calculation. Some cares must be required in preparing the initial state to avoid the violent variation at the initial stages of run. Namely, the electron velocity is set toward the θ-direction in the cross-sectional plane as the initial one. When we determined the phase of the Larmor gyration at random by way of trial, we observed that the number of the electrons became about half in several time steps. The magnitude of electron velocity is arranged to be Maxwellian and isothermal. The ion velocities are arranged to be at random in the phases of the Larmor gyrations, Maxwellian, and isothermal. The initial density of the electron n_e is set uniform in the 1st order of ϵ as follows;

$$\left.\begin{aligned} n_e &= n_{e0}\,(1 - \epsilon\kappa r/a \cdot \cos\theta) \quad \text{for} \quad r < \xi a, \\ n_e &= 0 \qquad\qquad\qquad\quad \text{for} \quad \xi a < r < a, \end{aligned}\right\} \tag{4.5}$$

where n_{e0} is the average density, and κ and ξ are parameters of the simulation runs. The initial density of the ions is set uniform in the minor cross-sectional plane.

4.3 THEORETICAL ANAYSIS IN THE CASE OF SMALL q

4.3–1 Equilibrium of the basic case, $q = 0$

For the basic case in which q is sufficiently small and ion is absent, Daugherty and Levy [5] derived the necessary conditions of the toroidal equilibrium from the steady-state continuity equation and the guiding center orbit of the electron due to the $E \times B$ drift. They are expressed in the following form:

$$n_e / \{B_0 / (1 + \epsilon r/a \cdot \cos\theta)\}^2 = f(\phi), \qquad \Delta\phi = -n_e e / \epsilon_0 , \tag{4.6}$$

where n_e is the electron density and f is an arbitrary function. When the function f is independent of ϕ, the spatial variation of the charge density n_e is of the order of ϵ. Therefore, the assumption that f is constant is permitted for the case investigated in this Chapter. Namely, the system is in the equilibrium to accuracy of order of ϵ, when κ is set equal to 2 in Eq. (4.5). In addition to Eq. (4.6), we require the boundary condition for ϕ, Eq. (4.3c), in

order to obtain the explicit solution of ϕ. The thin tube limit permits these equations to be solved in powers of the ratio ϵ. Solving the potential with an accuracy of the order of ϵ, we obtain

$$\phi \simeq -\frac{1}{4}\frac{n_{e0}e\,a^2}{\epsilon_0}\{(r/a)^2 - 1\}\{1 - 1.25\cdot\epsilon r/a\cdot\cos\theta\}\,. \tag{4.7}$$

4.3–2 The mean kinetic energy and the Larmor radius of electron

In the system studied in this simualtion, the mean kinetic energy of the electrons in the equilibrium is composed of the initial thermal energy and the kinetic energy supplied by the electrostatic potential. The toroidal effects on the average kinetic energy are of the order of ϵ^2, because the quantities of the order of ϵ cancel out due to the $E \times B$ rotation in the cross-sectional plane. In order to evaluate the average kinetic energy and the Larmor radius of the electrons simply, we introduce the following assumptions:

(1) The toroidal effects are neglected.

(2) The electron density n_e is uniform and the effect due to the presence of ion is negligible.

(3) The initial velocities of the electrons are directed azimuthally in the cross-sectional plane in accordance with the initial conditions of the simulations and are the equal magnitudes due to a simplification of calculations.

(4) The electron Larmor radius is sufficiently small.

After some calculations, we obtain the mean perpendicular kinetic energy, $m_e\overline{v_{e\perp}^2/2}$, and the typical Larmor radius, r_{Le}, which are averaged concerning θ and dependent on the magnitude of the electrostatic field or the average distance from the minor axis, r_0 (as indicated in Fig. 4.1), in the following:

$$m_e\overline{v_{e\perp}^2/2} = \frac{1}{2}m_e\omega_c^2a^2\cdot\{\frac{1}{2}q^2(r_0/a)^2 - \sqrt{2}\,q\zeta r_0/a + 2\zeta^2\}\,, \tag{4.8}$$

$$r_{Le} = \frac{1}{2}a\cdot|qr_0/a - 2\sqrt{2}\,\zeta|\,, \tag{4.9}$$

$$\zeta = \hat{v}_{et}/a\omega_c\,, \tag{4.10}$$

where $\hat{v}_{et}$ is the thermal velocity of the electrons, $\{1/3\cdot v_{eini}^2\}^{1/2}$ Averaging $m_e\overline{v_{e\perp}^2/2}$ over the volume of the vessel yields

$$\frac{1}{2} m_e <v_{e\perp}^2> = m_e \hat{v}_{et}^2 \, (2 + \frac{1}{4} q^2 \zeta^{-2} - 2\sqrt{2}/3q\zeta^{-1})/2 \qquad (4.11)$$

By getting the electric field E from Eq. (4.7), we obtain the $E \times B$ drift velocity v_E in the case of $r_0 \simeq a$

$$v_E = \frac{1}{2} q \omega_c \, [\, r_0 - \frac{1}{2} \epsilon a \cos\theta \cdot \{ 1.25 (3r_0^2/a^2 - 1) - 2r_0^2/a^2 \} \,] \, . \qquad (4.12)$$

4.3–3 Guiding center orbit of the electron

In the case of the finite q, Daugherty and Levy [5] derive the guiding center orbit from the conditions of the conservations of total energy, angular momentum, and adiabatic magnetic moment. We express the guiding center orbit in terms of the displacement Δr_g from the circle of radius r_0, which is concentric with the vessel wall in the cross-sectional plane, as shown in Fig. 4.1. From Eq. (3.2) of Reference [5] and Eqs. (4.7), (4.9), and (4.12), we derive the following:

$$\Delta r_g \simeq \epsilon r_0 \cos\theta \, [\, 0.625 \{ (r_0/a)^2 - 1 \} - \frac{1}{q} \{ 2\zeta^2 + \frac{1}{4} q^2 (r_0/a)^2$$

$$- \sqrt{2}\, q \zeta r_0 / a \} - \frac{2}{q} \zeta^2 - \frac{q}{4} \{ 1.75 (r_0/a)^2 - 1.25 \} \,] \, . \qquad (4.13)$$

Notice that the concentric circle intersects the guiding center orbit or Δr_g vanishes at $\theta = \pi/2$ and $3\pi/2$. The 1st term in the square bracket in Eq. (4.13) is due to that the contour of the electrostatic potential is deviated from the concentric circle, and becomes smaller as r_0 approaches the minor radius of the container wall a. Therefore, the other terms and the Larmor radius r_{Le} cannot be neglected near the container wall, and the electron orbits intersect the container wall partially in the neighbourhood of $\theta = \pi$. This fact suggests that the electrons which are lost to the container wall are more in the inner portion of the toroidal vessel than in the outer portion when the system is in the equilibrium.

4.4 SIMULATION RESULTS

Runs 1–8 were performed with parameters, which are shown in Table 4.1. The ratio q, which is one of the important parameters, is changed for runs 1–4 with a ratio of $\epsilon = 0.3$, and for runs 5 and 6 with $\epsilon = 0.15$, respectively. In order to investigate properties of the equilibrium, the density profiles in runs 1–6 are set deviating from those of the equilibrium

or κ is equal to unity. Namely, we are interested in a question of whether these systems can arrive at the equilibrium or not, or what type of the equilibrium these systems arrive at, even if they are not in the equilibrium at the initial time. On the other hand, the initial conditions of runs 7 and 8 are closer to the equilibrium than the others or κ is equal to 2.

TABLE 4.1 Some parameters for the simulations

a. Parameters concerning the model of simulations

$l = n = 64$, $l_c = 5$, $n_c = 9$, $\omega_c \Delta t = 0.25$ for run 1 and $\omega_c \Delta t = 1.00$ for runs 2–8

b. Parameters concerinng the apparatuses

$a = 3\ cm$, $R = 10\ cm$ or $20\ cm$, $B_0 = 1500\ Gauss$

c. Parameters concerning the initializations of runs

$N_{e0} = 10000$, $N_{i0} = 2000$, $P_i / P_e = 0.1$, $n_{i0} / n_{e0} = 0.02$, $\xi = 0.98$,

$kT_{e0} = 300\ eV$ ($\frac{1}{2} m_e \hat{v}_e^2 = 100\ eV$, $\zeta = 0.0075$), $kT_{i0} = 300\ eV$

$n_{e0}\ (cm^{-3})$	1.0×10^{11}	1.8×10^{10}	9.0×10^{9}	3.0×10^{9}
q	0.45	0.08	0.04	0.014
$\kappa = 1,\ \epsilon = 0.30$	run 1	run 2	run 3	run 4
$\kappa = 1,\ \epsilon = 0.15$		run 5	run 6	
$\kappa = 2,\ \epsilon = 0.30$		run 7	run 8	

4.4–1 The properties of the equilibrium with the stable oscillations

In run 1 with $q = 0.45$, the density profile of the electrons is greatly changed during a short time. Namely, the electrons near the container wall are scraped off in order and disappear to the wall during a time of $\omega_c t \simeq 10$, in which the electron density distribution is deformed from that of the initial state and a vacuum region appears along the container wall. Equations (4.9) and (4.13) indicate that the Larmor radius of the electron r_{Le} near the wall becomes about $0.2a$ in $q = 0.45$ and that the displacement of the guiding center Δr_g is of the order of r_{Le}. Therefore, the appearance of the vacuum region is explained by the fact that the guiding

center of the electron cannot exist in the region of $a - r_{Le} - \Delta r_g < r < a$. In other words, it can be concluded that the initial state of run 1 is not in the equilibrium.

In run 2 with $q = 0.08$, the density profile remains to be almost in the initial state throughout the whole time of run. As shown in Fig. 4.2, however, the decay curve of the

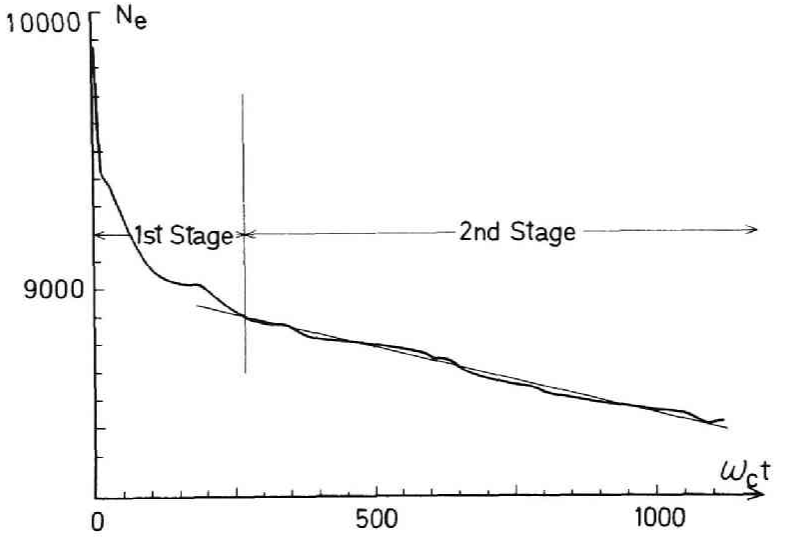

Fig. 4.2 Number of electrons in the container, N_e, vs time. The straight line, which is drawn in the 2nd stage, is used in order to measure the particle decay time τ_d approximately. (run 2)

electrons is divided into two stages of the process due to the effect of the finite Larmor radius, although its effect is much smaller than in run 1. The inclination of the decay curve is larger in the 1st stage than in the 2nd stage. The electrons near the wall, which cannot exist in the equilibrium state, are scraped off at the boundary in the 1st stage.

At the initial state of runs with a parameter of $\kappa = 1$, superfluous electrons exist more in the outer portion of the toroidal tube than in the inner portion, if the system is in the equilibrium expressed by Eq. (4.6). Accordingly, it is natural that the electrons, which are lost at the wall in the 1st stage, are more in the outer portion of the toroidal vessel (near $\theta = 0$) than in the inner portion (near $\theta = \pi$), as shown in Fig. 4.3 (a). When the system lies in the equilibrium or the 2nd stage, Fig. 4.3 (b) shows that the electrons are lost near $\theta = \pi$, as can be predicted from Eq. (4.13). Namely, in the 1st stage, the system arrives at the equi-

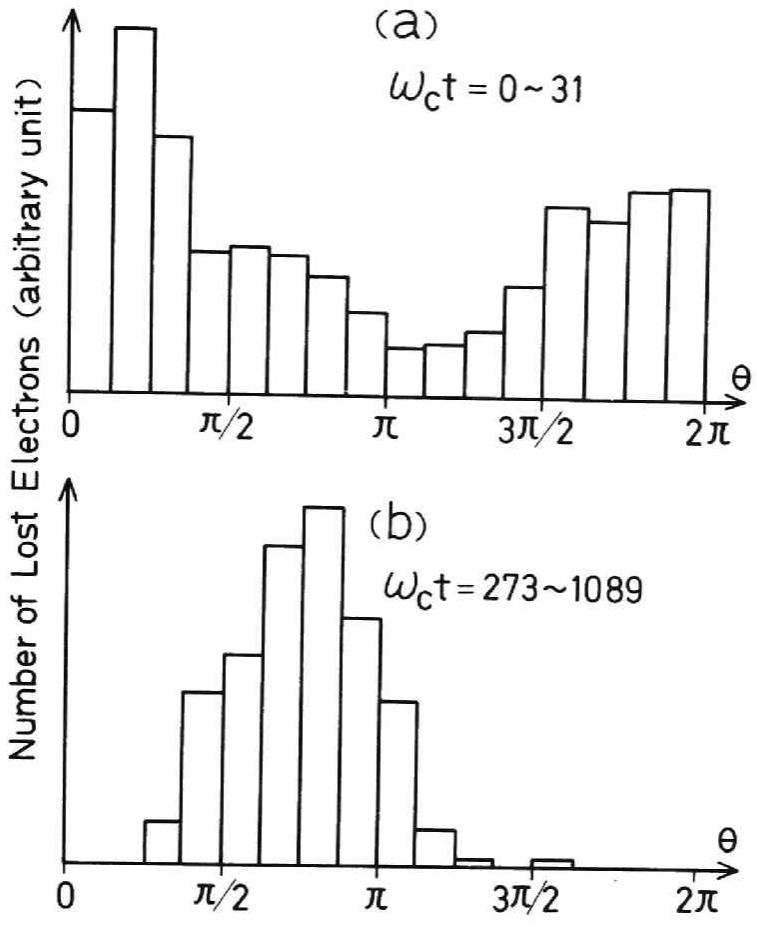

Fig. 4.3 This figure presents how many electrons are lost at the position of the container wall, which is indicated by one of the coordinates θ. (run 2)

librium, in which the density decreases rapidly in the region of width of about r_{Le} near the wall, when q or r_{Le}/a is finite.

In run 4 with sufficiently small q, however, the decay curve seems to change little its properties throughout run and the electrons reach the wall near $\theta = \pi$ from the beginning of run in spite of $\kappa = 1$. In other words, it loses the 1st stage and behaves likely as the 2nd stage of run 2 or the stage of the equilibrium throughout the whole time of run.

4.4–2 An equilibrium with a stable oscillation

As a method, with which we confirm that the 2nd stage of run 2 is truely in the equi-

librium state, we measure the electrostatic potential in the finite q and compare it with that calculated from the theoretical value in $q = 0$, Eq. (4.7). At least, this method is more informative than that of Daugherty *et al.* [3], who observed the image charge by the use of so-called current buttons. Figure 4.4 shows the time variations of the electrostatic potentials

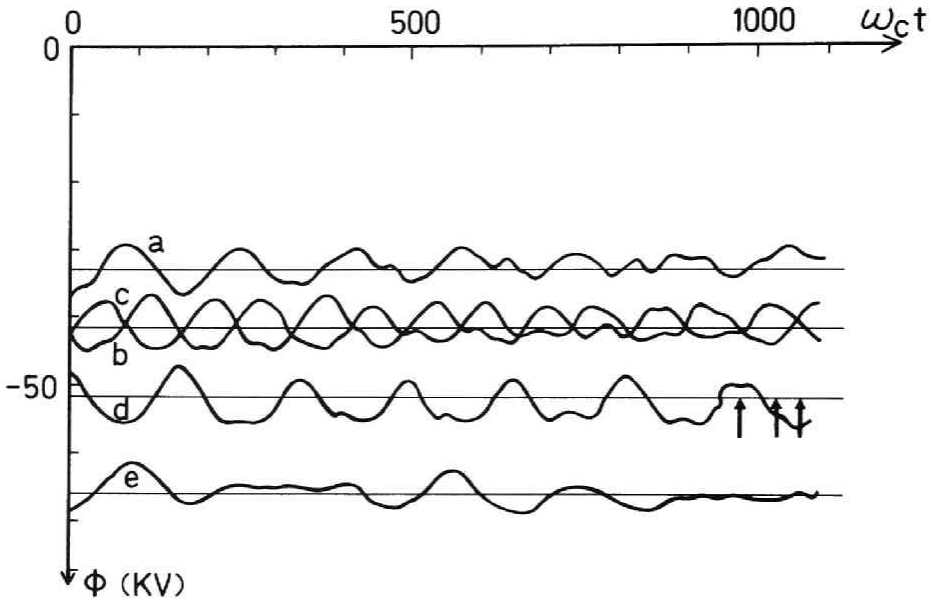

Fig. 4.4 Plots of the $l = 1$ dioctron mode. The electrostatic potential indicated by a symbol e is observed at $r = 0$ and those by a, b, c, and d are observed at $\theta = 0$, $\pi/2$, π, and $3/2 \cdot \pi$ on the circle of $r = 0.6a$. These smooth traces were obtained with a temporal average which eliminated the noises of high-frequency of the order of ω_c. The solid lines are values calculated from Eq. (4.7). (run 2)

at $\theta = 0$, $1/2 \cdot \pi$, π, and $3/2 \cdot \pi$ on the circles of $r = const.$ in the cross-sectional plane. They indicate that the $l = 1$ dioctron wave [6] is superposed on the theoretical value of the equilibrium. Its angular frequency ω_0 coincides with a value calculated from the average density and magnitude of the magnetic field within several percents. In other words, it is an evidence that the system is in the equilibrium with the stable oscillations. In a numerical study of Tokomak [18], also, it is reported that the motion has the general behavior of undamped almost-periodic oscillations about the equilibrium position if the initial state is close to the

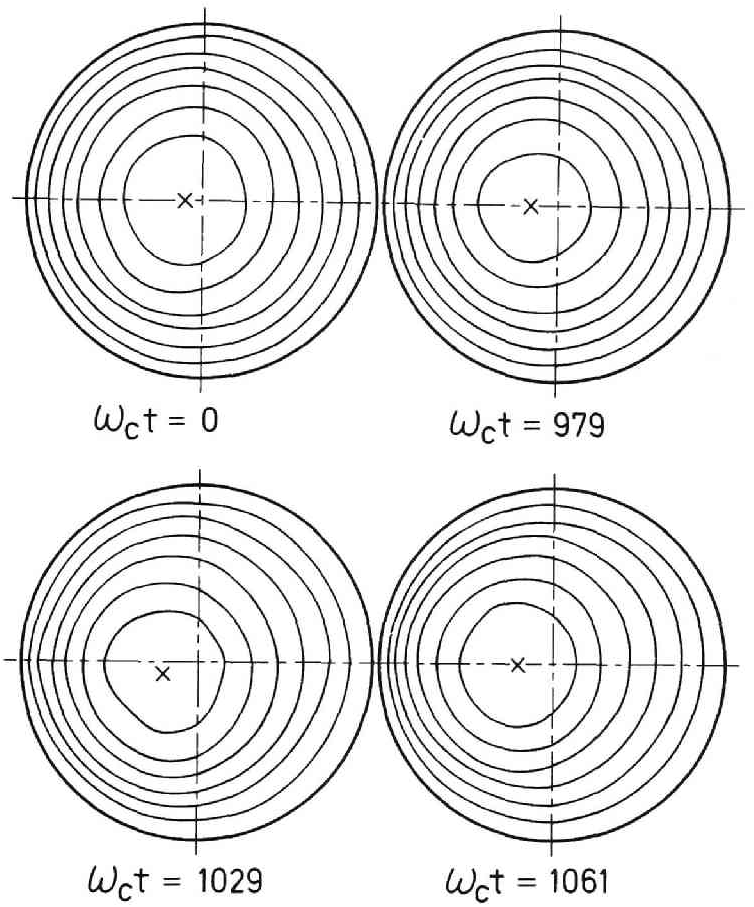

Fig. 4.5 Equipotential contours at the characteristic times of the $l = 1$ dioctron mode, which are indicated by arrows in Fig. 4.4. The contour intervals are 10^4 *V*. Cross points indicate the minimums of the electrostatic potentials. (run 2)

equilibrium. As shown in Fig. 4.5, the contours of the electrostatic potentials at the characteristic phases of the oscillation seem to be circles, of which centers do not coincide with the minor axis but are deviated to the major axis. The centers of these circles are rotated about the equilibrium positions due to the presence of the $l = 1$ dioctron mode. We present the potential profiles observed at $\theta = 0$ and $\theta = \pi$ in Fig. 4.6, selecting some of them at the

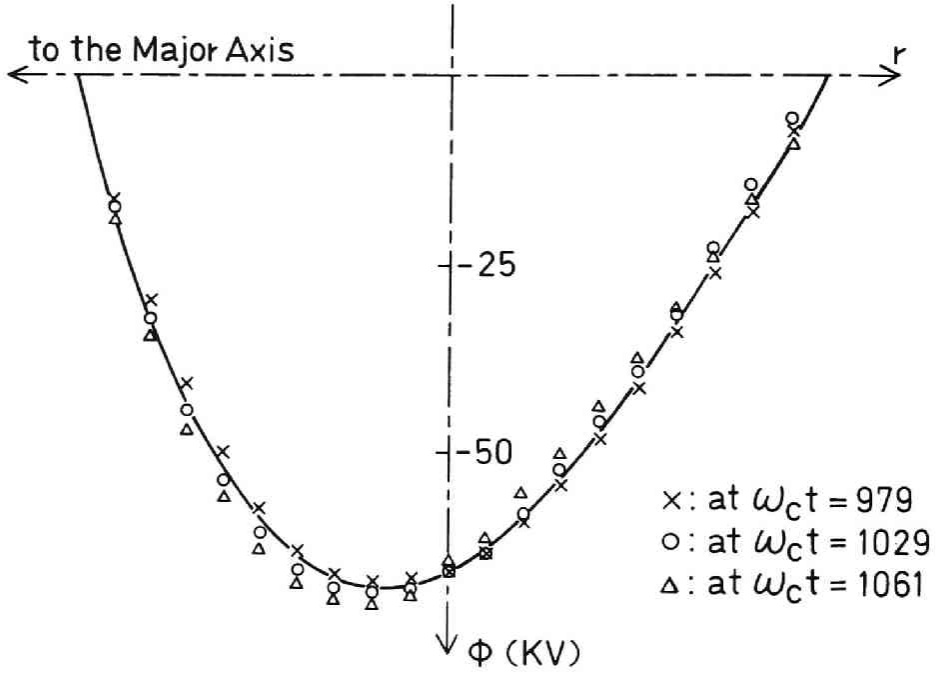

Fig. 4.6 Potential profiles observed at $\theta = 0$ and $\theta = \pi$. They are measured at times indicated by arrows in Fig. 4.4. The solid line is the value calculated from Eq. (4.7).

characteristic phases of the dioctron wave. They also suggest that the potentials are oscillated about the theoretical values of the equilibrium in $q = 0$ in spite of the run with the considerably large q.

Simple estimations such as the average perpendicular kinetic energy, the Larmor radius, and the guiding center orbit (Eqs. (4.8)–(4.13)) are satisfactory within the accuracy of this work. As an example, the observed values of the average kinetic energy of the electrons are compared with the estimated values of Eq. (4.11) in Fig. 4.7.

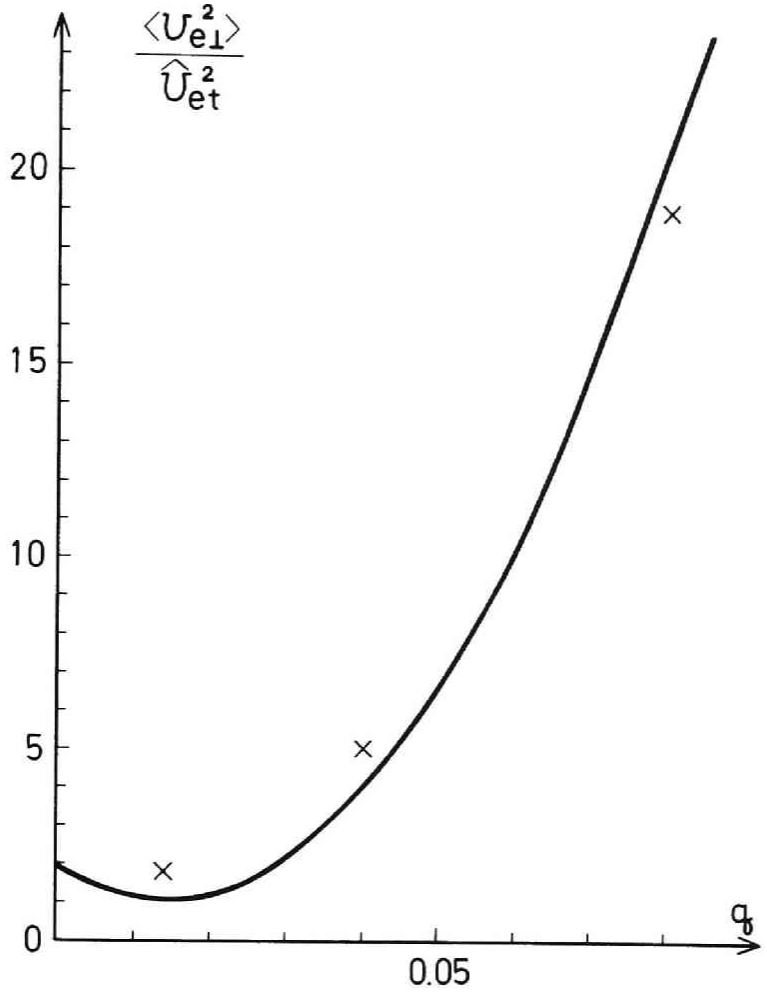

Fig. 4.7 The average of the square of the electron perpendicular velocities, $<v_{e\perp}^2>$ vs q. The solid line is the value calculated from Eq. (4.11), by setting ζ equal to 0.0075, which is shown in Table 4.1. The cross points show the values measured in runs 2, 3, and 4.

4.4–3 The quiescent equilibrium and behaviors of ion

Runs 7 and 8 with $\kappa = 2$ are set closer to the equilibrium than the other runs. Accodingly, their amplitudes of $l = 1$ dioctron mode are smaller by a factor of about 10 than in runs 2 and 3, respectively. Any sign of growth of an instability cannot be observed during

time of about *10* t_0 *(=* $2\pi / \omega_0$*)*. Accordingly, the maximum q of the quiescent equilibrium in the uniform density is concluded to be about 0.1, judging from run 7. This value is larger by a factor of 4 than in the experimental evidence [3].

Here we discuss the results associated with ion simply. The ion density would be too small for ions to affect the phenomena of the whole system. The kinetic energy and the ion density at the minor axis oscillate with the double of the frequency Ω (See Eq. (10) of Reference [8]) in accordance with the theory, because the ion thermal energy is negligible and the electrostatic potential profile is almost parabolic. Although the ratio of the total number of ions to that of electrons is only 0.02, the maximum ion density at the axis becomes about half of the electron density and then the mean ion kinetic energy reaches the maximum values of about 30 *Kev* in run 7.

4.4–4 Equilibrium diffusion of the electrons

In runs 2–8, the stable $l = 1$ dioctron modes are observed and the slow decreases of the electrons to the wall are measured. A principal origin of the electron decay is inferred to be concerned with the stable oscillations. Table 4.2 indicates that the decay time τ_d becomes shorter as the amplitude of the oscillations which can be controlled by the magnitude of κ are larger. In run 4, time-derivatives of the decay curves of the electrons and the electron kinetic temperature have components of the oscillations with a period of t_0, as shown in Fig. 4.8.

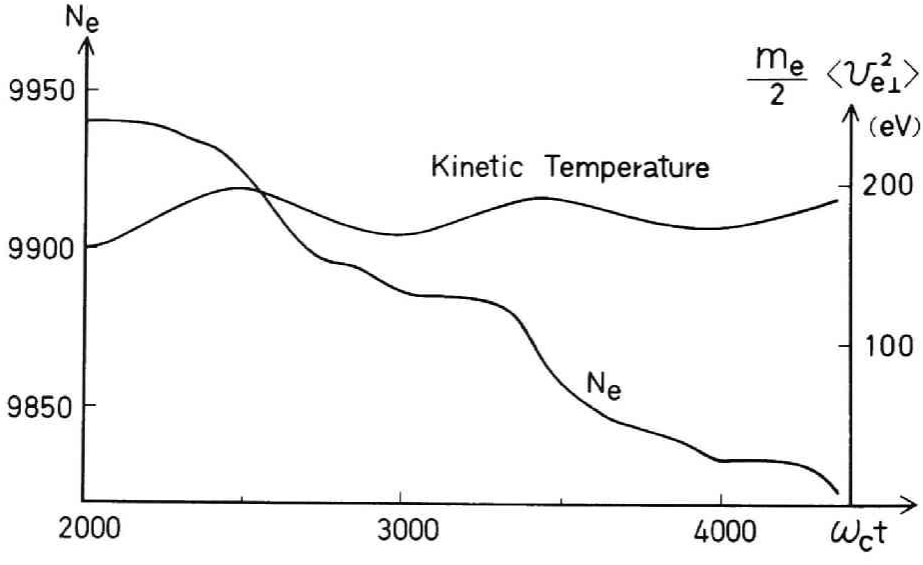

Fig. 4.8 Number of electrons in the container, N_e, vs time and the average perpendicular kinetic energy of electron vs time. (run 4)

Namely, the $E \times B$ drift velocity becomes larger (See Eq. (4.12)) and the electrons are lost to the wall, when the clustered electrons sustaining the oscillation rotate to reach the inner portion of the toroidal tube. This fact suggests that the electrons are lost in a phase of the $l = 1$ dioctron mode. Note that the oscillations of the kinetic temperatures are masked by a noise of high frequency of about ω_c and the decay curves are smoother as shown in Fig. 4.2, when q is set larger.

When the stable oscillations determine the electron loss or the electrons are lost in a phase of the oscillation, the decay time τ_d is proportional to t_0. Its proportional coefficient k_d, which is presented in Table 4.2, is inferred to depend on the amplitudes of the oscillations,

TABLE 4.2 Measured values in the equilibrium, where $\Delta\phi/\phi_0$ is measured at $r = 0.6a$ and $\theta = \pi$.

run No.	q	κ	ϵ	$\Delta\phi/\phi_0$	$\omega_c t_0$	$\omega_c \tau_d$	k_d τ_d/t_0
run 1	0.45	1.0	0.30				
run 2	0.08	1.0	0.30	6.7%	160	21000	130
run 3	0.04	1.0	0.30	8.2%	320	72000	230
run 4	0.014	1.0	0.30	8.5%	960	176000	370
run 5	0.08	1.0	0.15	4.2%	160	35000	270
run 6	0.04	1.0	0.15	4.7%	320	81000	250
run 7	0.08	2.0	0.30	0.8%	160	86000	540
run 8	0.04	2.0	0.30	1.1%	320	222000	700

the kinetic temperature, the aspect ratio, the magnitude of the magnetic field, the minor radius of the container, and so on. However, their dependences are too complex and the number of the simulation runs is too insufficient to discuss it. From a practical point of view, it is the most important to generate no oscillations when the plasma is produced in actual experiments. By its success, the long confinement can be expected.

4.5 DISCUSSIONS AND CONCLUSIONS

In these devices, which contain the electron clouds by the toroidal magnetic fields, the

upper limit of q is restricted by the equilibrium and stability conditions. In the computer simulations using the finite-sized particle model, however, we show an example of the quiescent equilibrium in the ratio q larger by a factor of 4 than in the experimental results [3]. Furthermore, we indicate the features of these systems obtained in this simulation:

(1) The $l = 1$ dioctron modes which are controlled by the initial condition in the simulation or are probably generated in plasma productions in actual experiments spoil the confinement time. If we can make this mode damp in a shorter time than in the required confinement time, we have little obstructions. In the inductive charging scheme, Daugherty *et al.* [3] obtained a quiescent equilibrium by the use of the stabilizing effect that a rising magnetic field has on a dioctron wave.

(2) A possibility of generation of the magnetron instability is suggested by Daugherty *et al.* [3], when q exceeds 0.05. In run with $q = 0.08$, however, the system is quiescent and stable.

(3) Electrons are lost to the wall at the inner portion of the toroidal vessel, as can be predicted from the guiding center orbit of the electron.

In a conclusion, we can expect a long confinement due to only classical losses in the considerable large q ($\lesssim 0.1$). In this simulation, however, the ion-electron two stream instability [7] is avoided since a ratio n_i/n_e is about 0.02; theoretical and experimental evidences indicate that the value of n_i/n_e greater than approximately 0.1 is required for this instability to be significant [3, 7]. Because the ideal conditions assumed in this simulation are difficult to realize in actual experiments, the influences of this instability on the confinement time will not be negligible. With the same code used here, we intend to investigate this instability in a future paper.

REFERENCES

1. G. S. Janes: Phys. Rev. Letters 15 (1965) 135.
2. G. S. Janes, R. H. Levy, H. A. Bethe, and B. T. Feld: Phys. Rev. 145 (1966) 925.
3. J. D. Daugherty, J. E. Eninger, and G. S. Janes: Phys. Fluids 12 (1969) 2677.

4. A. Mohri, M. Masuzak T. Tsuzuki, and K. Ikuta: Phys. Rev. Letters 34 (1975) 574.
5. J. D. Daugherty and R. H. Levy: Phys. Fluids 10 (1967) 155.
6. R. H. Levy: Phys. Fluids 8 (1965) 1288.
7. O. Buneman, R. H. Levy, and L. M. Linson: J. Appl. Phys. 37 (1966) 3203.
8. R. H. Levy, J. D. Daugherty, and O. Buneman: Phys. Fluids 12 (1969) 2616.
9. R. H. Levy and R. W. Hockney: Phys. Fluids 11 (1968) 766.
10. C. K. Birdsall and D. Fuss: J. Computational Phys. 3 (1969) 494.
11. A. A. Galeev and R. Z. Sagdeev: Zh. Eksp. Teor. Fiz. 53 (1967) 348 [Sov. Phys.-JETP 26 (1968) 233].
12. C. G. Smith and A. S. Bishop: in *"Conference on Plasma Physics and Controlled Thermonuclear Fusion Research"* CN-24/D-9, Novosibirsk (1968)
13. H. Abe, K. Kawai, T. Yamada, and R. Itatani: J. Phys. Soc. Japan 33 (1972) 216.
14. R. L. Morse: in *"Methods in Computational Physics"* edited by B. Alder, S. Fernbach, and M. Rotenberg, Vol.9, Academic, New York (1970).
15. A. B. Langdon and C. K. Birdsall: Phys. Fluids 13 (1970) 2115.
16. H. Okuda and C. K. Birdsall: Phys. Fluids 13 (1970) 2123.
17. H. Abe, J. Miyamoto, and R. Itatani: J. Computational Phys. 19 (1975) 134.
18. Yu. N. Dnestroskii, D. P. Kostomarov, and A. M. Popov: Sov. Phys.-Tech. Phys. 17 (1973) 1771.
19. T. Takizuka, H. Abe, H. Momota, and C. Namba: Plasma Phys. 17 (1975) 887.

CHAPTER 5

COMPUTER SIMULATION OF R. F. CONFINEMENT OF PLASMAS IN AN OPEN-ENDED TOROIDAL QUADRUPOLE

5.1 INTRODUCTION

Besides the various closed systems, an open-ended system such as a mirror or a cusp is still very interesting as a controlled thermonuclear fusion reactor, if it is realized to suppress the so-called "end loss" or to recover the lost energy. On this line, Miyake *et al.* [1] have attempted to reduce the end loss by applying the r. f. electric field to a cusped plasma. Until the present day, they have obtained some encouraging results as for the reduction of the plasma loss from the line end, although the problems are still unsolved about the loss from the spindle ends.

On the other hand, R. W. Moir [2] has proposed 'Open Ended Toroidal Quadrupole' as an open-ended system of a large mirror ratio, which has the possibility of suppressing both end losses and microinstabilities by applying a d. c. electric field.

In this Chapter, some properties of plasma contained in this field and the possibility of improvement as for the containment with the use of the r. f. electric field are discussed.

A technical method used in this Chapter is a numerical simulation which is based on the 'Collisionless PIC Method' developed by Morse and Nielson [4], and Smith and Bishop [5]. As explained in Section 1.4, the collisionless PIC method (PIC model) is computationally equivalent to the CIC model, although their origins are different. For convenience, we explain the method used in this Chapter on the conception of the collisionless PIC method. These are explained in the next section (Section 5. 2). Furthermore, we assume the following in this simulation :

(1) The physical quantities are azimuthally symmetric (so-called the "two-and-a-half

dimensional simulation").

(2) The effects of current in the plasma on the applied magnetic field are negligible (quasistatic approximation).

(3) Motion of the ion is described by the Lorentz equation and that of the electron by the drift equation.

The models which are actually used can be divided into two levels : model A and model B. Concerning the model A, we assume the following :

(A–1) Collisions, which can be sufficiently reduced in the collisionless PIC method, are introduced effectively for ions on the basis of a large angle scattering.

(A–2) The r. f. electric fields are introduced in a simplified way.

We improve the model A to make it approach the more realistic one and obtain the model B. Namely, instead of the assumptions A–1 and 2, we assume the following concerning the model B :

(B–1) The collisional effects are introduced for both ions and electrons. Namely, we devise a collision model, which represents the properties of the small angle scattering of the Coulomb collision by the use of a modification of the Langevin equation [10].

(B–2) The r. f. electric field is applied by the use of the condenser electrodes.

Sections 5.2 ~ 5.4 refer to the simulations using the model A; In Section 5.2, some explanations of the model are presented; In Section 5.3, the simulations indicate that both the particle decay time and the energy containment time are improved to a certain degree and the ion temperature rises drastically when the r. f. electric field is applied, and the improvement of the containment effect due to the application of the r. f. electric field can be typically understood by tracing the motion of some test particles; In Section 5.4, some discussions concerning runs done by the model A are presented and some problems relating to this model are pointed out.

Sections 5.5 ~ 5.7 refer to the simulation using the model B; In Section 5.6, the model B is explained simply and it is discussed to require the feedback control of the magnitude of the r. f. electric field; In Section 5.6, results concerning runs done by the model B are discussed;

In Section 5.7, the summary is presented.

5.2 MODEL A

5.2–1 Configuration of the magnetic field

The magnetic field considered here is composed of a toroidal magnetic field and a toroidal line-cusped magnetic field, and has the properties of an axisymmetric open system. Accordingly, the features of this magnetic configurations are the followings:

(1) The system for the plasma containment is axisymmetric. Therefore, a charged particle moves in this system conserving the angular momentum.

(2) On a cross-sectional plane of the toroidal vessel, magnetic isobars are approximately circular and the line of forces are cusped shapes. Therefore, the system has the property of *Min. B.*

The toroidal coordinates (x, y, z) are introduced in order to represent the system characteristically. They are related to the cylindrical coordinates (ρ, φ, z) by the equations:

$$\rho = R + x, \quad y = \zeta, \quad z = R\varphi, \tag{5.1}$$

where R is the major radius of the toroidal container as shown in Fig. 5.1. Let the cross section of the container be a square with side $2a$. The whole physical quantities can be expanded into powers of $\epsilon = a/R$ and are calculated to the accuracy of the first order of ϵ. Then the magnetic field can be described as

$$\left.\begin{aligned} B_x &= B_c\, y/a, \\ B_y &= B_c(x/a - 0.5\,\epsilon\,(y/a)^2), \\ B_z &= \gamma B_c\,(1 - \epsilon\,(x/a)), \end{aligned}\right\} \tag{5.2}$$

where B_c is the characteristic intensity of the cusp field and γ is the ratio of the magnitude of the toroidal field to that of the cusp field.

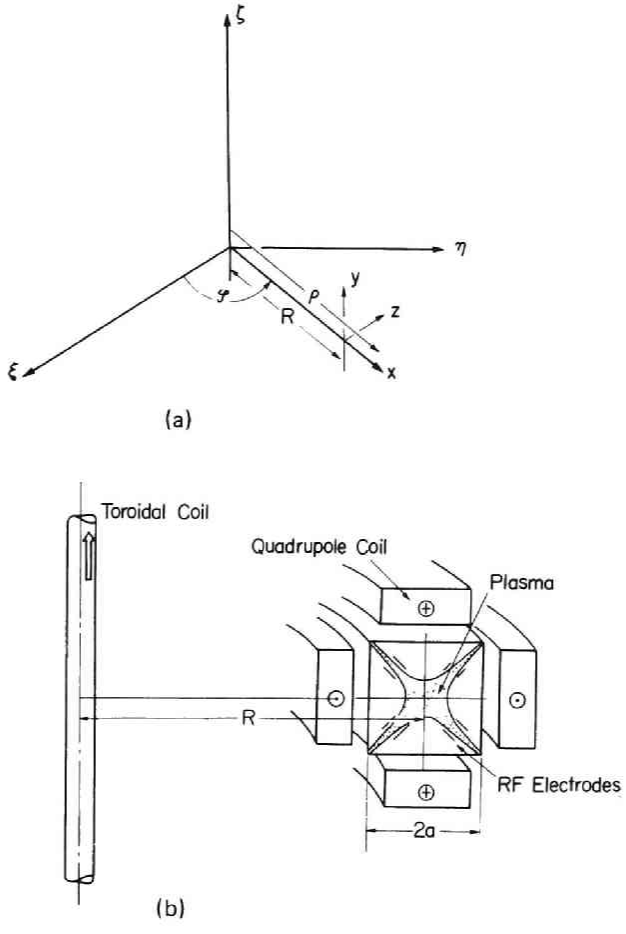

Fig. 5.1 Toroidal coordinates (a) and a schematic illustration of the device for plasma containment (an open-ended toroidal quadrupole) (b).

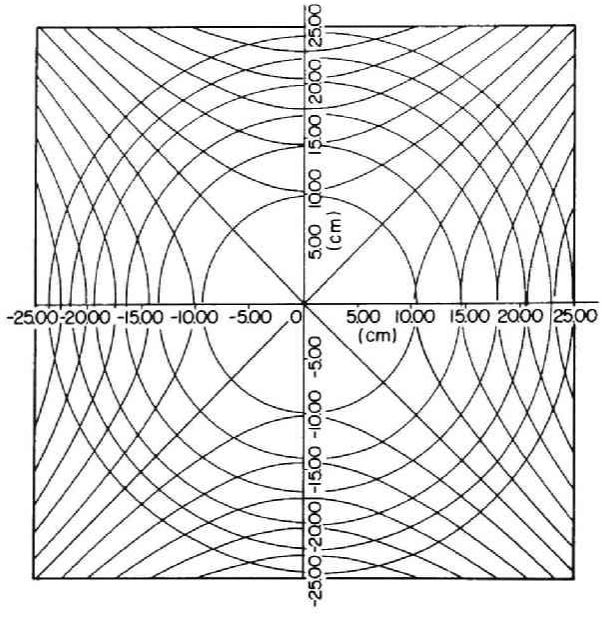

Fig. 5.2 A projection of lines of force and magnetic isobars of an open ended toroidal quadrupole on the cross-sectional plane.

5.2–2 The r. f. electric field in the model A

In the model A, the r. f. electric field is applied only in the domain D, which has the width 2Δ and is defined by the following equations:

$$D \equiv \{ (x, y) \}, \tag{5.3}$$

where x and y satisfy the equations:

$$\frac{(r_0 - \Delta)^2}{a^2} \leqq \left(\frac{x}{a} - \epsilon \gamma^2 \right)^2 + \left(\frac{y}{a} \right)^2 \leqq \frac{(r_0 + \Delta)^2}{a^2}.$$

In these domains, the r. f. electric field E_{ext} is assumed to be perpendicular to B on the cross-sectional plane of the torus;

$$E_{ext} = \begin{cases} E_0 \sin \omega_r t \left[\left\{ \frac{x}{a} - 0.5\epsilon \left(\frac{x}{a} \right)^2 \right\} \hat{x} - \frac{y}{a} \hat{y} \right], & (x, y) \in D; \\ 0, & (x, y) \notin D, \end{cases} \tag{5.4}$$

where E_0 is the magnitude of the r. f. electric field and the angular frequency ω_r is set equal to the ion cyclotron angular frequency at the magnetic isobar:

$$(x - \epsilon\gamma^2 a)^2 + y^2 = r_0^2 .$$

5.2–3 Motion of the charged particles

The motion of charged particles is assumed to be described by the Lorentz equation in which the self-consistent electric field of the plasma is taken into account. The charged particles are forced to interact with only the axisymmetric field on the assumption that the simulated plasma is fairly stabilized. Furthermore, the electric field of short wave length is neglected (Collisionless PIC method), because the physical phenomena at a quasi-equilibrium state are aimed to be studied in this simulation. Therefore, in order to simulate the decay processes of the confined plasmas, we need add the collisional effects to the motions of the charged particles by the use of the methods explained in Section 5.2–5, because the collisional effects essentially influence the decays of plasmas in the stabilized plasmas.

The approximation of the adiabatic invariance cannot be permitted concerning the ion motion, because the value of r_L/a (r_L is the Larmor radius) is not negligibly small and the value of ω_r/ω_c ($\omega_c = eB/M$) is of the order of unity. Accordingly we must adopt the Lorentz equation as an equation of the ion motion and can utilize the conservation law of the angular momentum in the axisymmetric system. On the otherhand, the invariance of the magnetic moment μ can be assumed for the electrons, since the Larmor radius of the electron is sufficiently small compared with the characteristic length of the spatial variation. Therefore, the equation of motion for the electrons is assumed to be approximated by the drift equation. Afterall, we have equations of motion for ions:

$$\left.\begin{aligned} M\frac{d^2 r}{dt^2} &= e(E + v \times B) , \\ \text{and} \qquad & \\ P_\varphi &= M\rho^2\frac{d\varphi}{dt} + e\rho A_\varphi \equiv Const , \end{aligned}\right\} \qquad (5.5)$$

where

$$A_\varphi = \frac{a}{2} B_c \left[\left\{ 1 - \frac{\epsilon}{3} \left(\frac{x}{a}\right) \right\} \left(\frac{x}{a}\right)^2 - \left(\frac{y}{a}\right)^2 \right] , \qquad (5.6)$$

and for electrons:

$$\left.\begin{aligned}
\frac{d\boldsymbol{r}}{dt} &= v_{\parallel}\frac{\boldsymbol{B}}{B} + \frac{\boldsymbol{E}\times\boldsymbol{B}}{B^2} - \frac{m}{eB^3}\left(\frac{\mu B}{m} + v_{\parallel}^2\right)\cdot \boldsymbol{B}\times\nabla B, \\
\frac{dv_{\parallel}}{dt} &= -\frac{1}{m}\frac{\boldsymbol{B}}{B}\cdot(\mu\nabla B + e\boldsymbol{E}) + \frac{v_{\parallel}(\boldsymbol{E}\times\boldsymbol{B})\cdot\nabla B}{B^3},
\end{aligned}\right\} \qquad (5.7)$$

and

$$\mu = \frac{m v_{\perp}^2}{2B} \equiv Const.$$

The Runge-Kutta method is utilized for the equations concerning the ion and Euler's predictor-corrector method (the point-slope method) [6] for the equations concerning the electron, as the integration schemes.

5.2–4 The selfconsistent electric field

The collisionless PIC method, which can reduce the superfluous fluctuations due to the use of the reduced number of particles each with a larger charge and mass than the laboratory plasmas, is introduced in this simulation in order to compute the internal electric field. The method is summarized in a case of the thin toroidal container with square cross-sections simply, as follows.

Firstly, the distributed space changes are sampled on the grid points which divide the container into $2M \times 2M$ grids. Then the method of the 'Area Weighting' [4] is utilized in order to smooth out the space charge. The effect caused by the toroidicity is corrected on the grid points. Then the charge density $\rho(x, y)$ is approximated by the Fourier series:

$$\rho(x, y) = \sum_{m,n=1}^{2M-1} \rho_{mn}\cdot\sin m\frac{\pi}{a}(x+a)\cdot\sin n\frac{\pi}{a}(y+a), \qquad (5.8)$$

where the coefficients are determined by the least square approximation.

Equation (5.8) indicates that the electric field with the wavelength $\lambda \leqq a/M$ is neglected automatically. Axisymmetric Poisson's equation is represented in terms of the toroidal coordinates:

$$\Delta^{(0)}\phi + \frac{\kappa}{1+\kappa x}\frac{\partial\phi}{\partial x} = -\frac{1}{\epsilon_0}\rho(x, y), \qquad (5.9)$$

where κ is the inverse of R and the operator $\Delta^{(0)}$ denotes $\partial^2/\partial x^2 + \partial^2/\partial y^2$. The scalar potential ϕ can be expanded into power series of κ, and can be calculated accurately to the first order of κ:

$$\left.\begin{aligned} &\phi = \phi_0 + \kappa\phi_1 , \\ &\Delta^{(0)}\phi_0 = -\rho/\epsilon_0 , \\ &\text{and} \\ &\Delta^{(0)}\phi_1 = -\partial\phi_0/\partial x . \end{aligned}\right\} \qquad (5.10)$$

The boundary condition for the scalar potential requires that it vanishes at the container wall ($x = \pm a$ or $y = \pm a$), if the container is assumed to be metallic. Then, ϕ_0 and ϕ_1 can be determined by the use of the Green function of $\Delta^{(0)}$

5.2–5 A Collision model used in the model A

In the stable plasmas confined in the open-ended systems, the particle losses are caused essentially by the collisional effects on ions, because the diffusion of the particles is ambipolar along the lines of force, as confirmed actually in our preliminary simulation results. Therefore, we do not suffer the fatal damage to the reliabilities of the simulations with which we study the effects of the suppression of the end losses associated with the applied r. f. electric field, even if we neglect the collisional effects on the electrons.

Taking into account that the velocity distribution is relaxed to the Maxwellian distribution after a collision time τ_c, we adopt the simple collision model of the large angle scattering. In the concrete, the procedure of realizing this model can be explained by the three steps as follows;

(1) Ions of $\Delta N = (k\Delta t/\tau_c) N_i$ (N_i is the total number of ions in the container) are selected at random at each time $k\Delta t$.

(2) The thermal velocity of ion is computed and the normally distributed random numbers of $3\Delta N$ whose r. m. s. corresponds to the estimated thermal velocity are generated.

(3) The velocities of ions selected at random are replaced by the generated ones.

5.3 SIMULATION RESULTS OBTAINED BY THE USE OF THE MODEL A

Physical quantities of the plasmas simulated by the use of the model A are listed up on the Tables 5.1 and 5.2. The initial plasmas are represented by 3000 particles (Ion: 1500 and Electron: 1500) and the cross-sectional plane of the toroidal container is divided into 16 X 16

TABLE 5.1 Device for plasma confinement.

$B_{max} = 7500$ Gauss,		$B_{min} = 2500$ Gauss,
$R = 250$ cm,		$a = 25$ cm,
$E_0 = 40$ V/cm,		$\omega_r = 4.15 \times 10^7$ Rad Hz,
$r_0 = 17.7$ cm,	and	$\Delta = 5.3$ cm.

TABLE 5.2

(a) Properties of simulated plasma:

$M = 1.67 \times 10^{-24}$ g (The hydrogen mass),

$M/m = 25$,

$\tau_{ic} = 8\,\mu$ sec, and

line density of particles = 1.7×10^7 /cm.

(b) Initial conditions:

Energy distributions: 300 eV Maxwellian for both ions and electrons.

Spatial distributions: Uniform torus-shaped plasma of the minor radius 4.5 cm composed of ions and electrons are laid at the center of the toroidal container.

grids ($M = 8$) as is mentioned in Section 5.2. In order to compare the effects of the r. f. electric field, simulations are carried out in two cases; The first case is that only the magnetic fields are excited and the second is that in addition to them the r. f. electric field is applied since $3\,\mu$ sec. The phenomena for the initial $3\,\mu$ sec are understood to exhibit the relaxation into the quasi-equilibrium state, in which the collisions only determine the plasma loss.

5.3–1 Particle decay time and energy containment time

The particle decay time τ_n in the usual open ended system is determined by the end loss. If the loss mechanism has property of the ambipolar diffusion and mainly owes to the collisions of the large angle scattering acting only ions (this is assumed in Section 5.2), the particle decay time τ_n can be approximated after simple calculations by

$$\tau_n = R_m \left(1 + \sqrt{1 - 1/R_m}\right) \tau_{ic}\,, \tag{5.11}$$

where R_m is the mirror ratio and τ_{ic} is the effective collision time of ions defined in Section 5.2. Equation (5.11) gives $\tau_n \simeq 43\ \mu$ sec corresponding to $\tau_{ic} = 8\,\mu$ sec which is selected as

a simulation parameter. This is consistent with $\tau_n \simeq 53\,\mu sec$ measured from the simulation result. When the r. f. electric field of $40\ V/cm$ is applied, τ_n takes the value of $62\,\mu sec$ which is 1.2 times larger than that in no r. f. electric field. The charge separation $(N_i - N_e)/N_i$ does not exceed 2% through the quasi-equilibrium states, although the mass ratio M/m is chosen to be 25 and the electron thermal velocity is 5 times larger than ion one. In other words, the computer simulation evidences that the particle loss is due to the ambipolar diffusion.

The energy containment time τ_E is considered to be the most important especially for the system considered in this text, into which the external energy flows. Namely, for ions which resonate with the r. f. electric field, the ion energy containment time τ_E is defined as follows;

$$\frac{dQ_i}{dt} = S - \frac{Q_i}{\tau_E}, \tag{5.12}$$

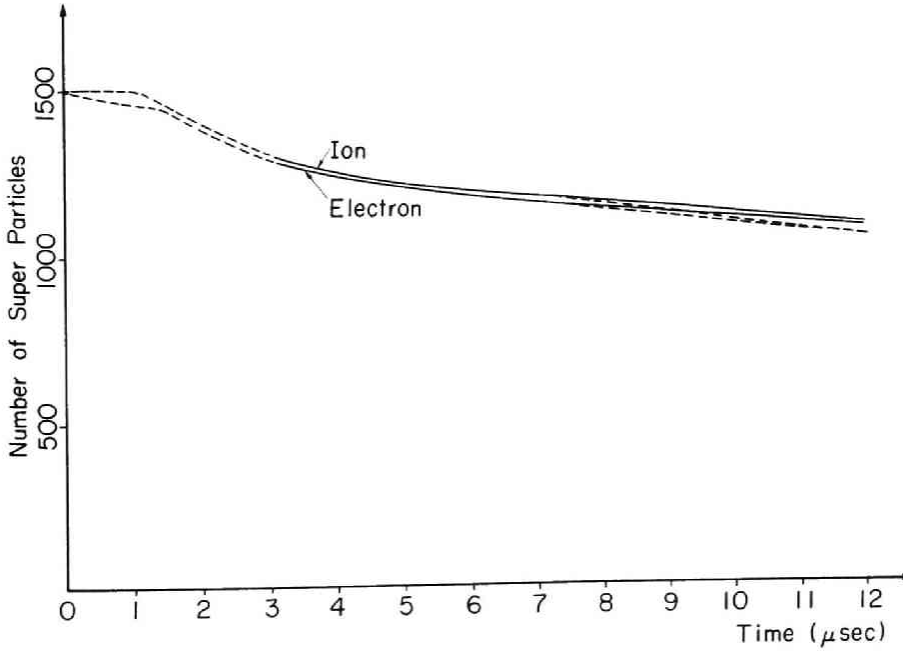

Fig. 5.3 Particle decay curves. Solid lines indicate the case that the r. f. electric field is turned on and broken lines correspond to the case of no r. f. electric field. For initial $3\,\mu sec$, the plasma is at a relaxation stage to an equilibrium state.

where $Q_i = N_i \kappa T_i$, and S is the input energy of the system. By observing the loss energy Q_{iW} of the ion to the wall, Eq. (5.12) can be approximated as follows;

$$\tau_E = Q_i / (\Delta Q_{iW} / \Delta t), \tag{5.13}$$

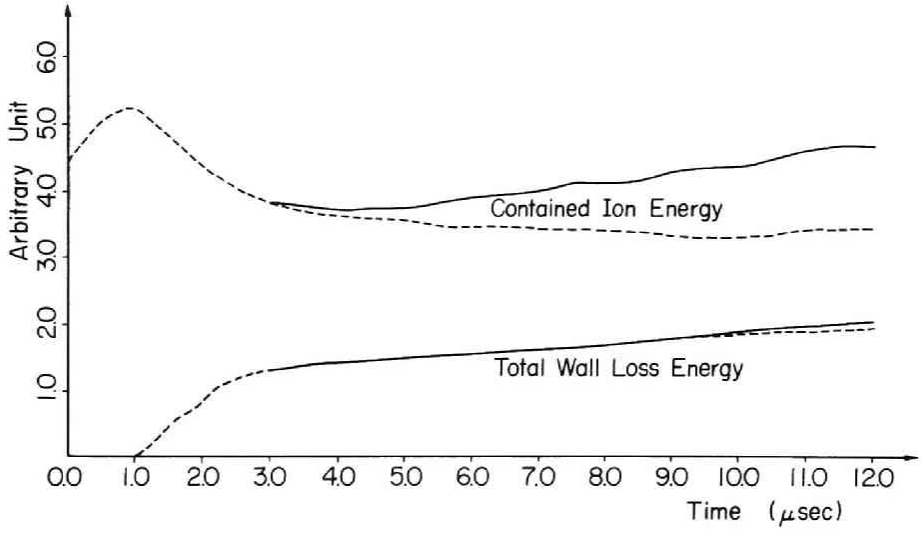

Fig. 5.4 Time variations of the contained ion energy Q_i and the wall loss energy Q_{iW}.

where ΔQ_{iW} is the decrement of Q_{iW} observed during the short time Δt through which S is assumed to be constant. The time variations of Q_i and Q_{iW} are shown in Fig. 5.4. When the r. f. electric field is turned on, Q_{iW} is not so much increased compared with the case of r. f. off, nevertheless Q_i is increased. Accordingly, τ_E is gradually increased to be *59 μ sec* by applying the r. f. electric field; for reference, τ_E is *49 μ sec* in the case of no r. f. electric field.

5.3–2 Ion and electron temperatures

The time evolutions of the ion and the electron temperatures are shown in Figs. 5.5 and 5.6. First, in the case of no r. f. electric field, the temperatures parallel to the lines of force are almost constant: $T_{i\parallel} \simeq 53\,eV$ and $T_{e\parallel} \simeq 27\,eV$, otherwise the perpendicular temperatures are slowly increased to be $T_{i\perp}/T_{i\parallel} \simeq 5$ and $T_{e\perp}/T_{e\parallel} \simeq 10$ at time *12 μ sec*. Next, when the r. f. electric field is turned on, $T_{i\perp}$ is increased drastically and so the total temperature T_i increases at the ratio of $\Delta T_i / \Delta t \simeq 15\,eV/\mu$sec.

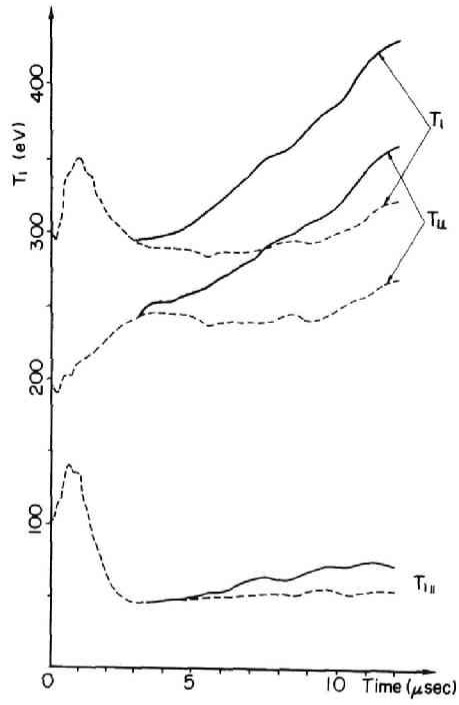

Fig. 5.5 Ion temperatures vs time.

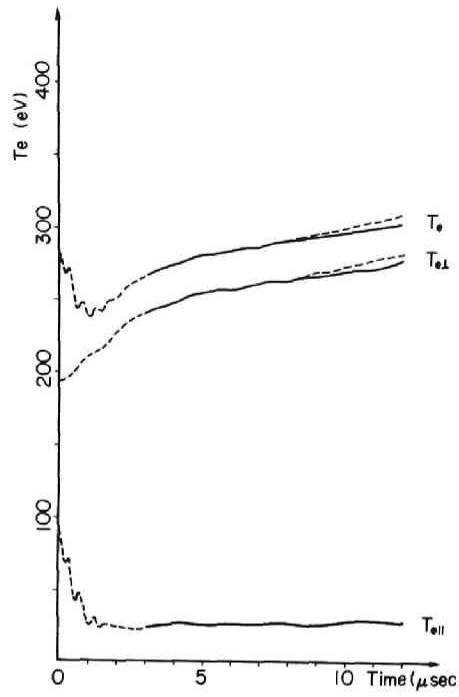

Fig. 5.6 Electron temperatures vs time.

5.3–3 Velocity distributions

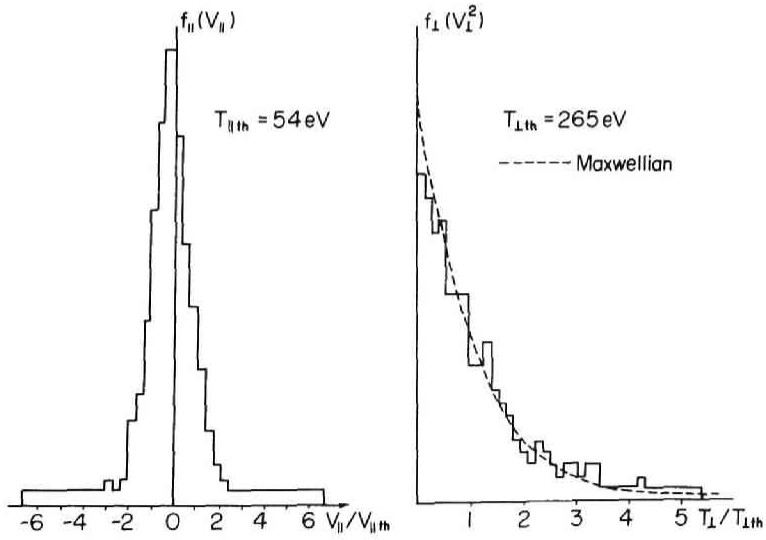

Fig. 5.7 Velocity distributions $f_{\parallel}(v_{\parallel})$ and $f_{\perp}(v_{\perp}^{2})$ at the time $12\,\mu sec$.

The velocity distribution appears to be stationary after the time $t = 6\,\mu\,sec$. The velocity distribution functions

$$f_{\parallel}(v_{\parallel}) = \int dr \int \pi dv_{\perp}^{2} f(v_{\perp}^{2}, v_{\parallel}, r),$$
$$f_{\perp}(v_{\perp}^{2}) = \int dr \int dv_{\parallel} f(v_{\perp}^{2}, v_{\parallel}, r), \tag{5.14}$$

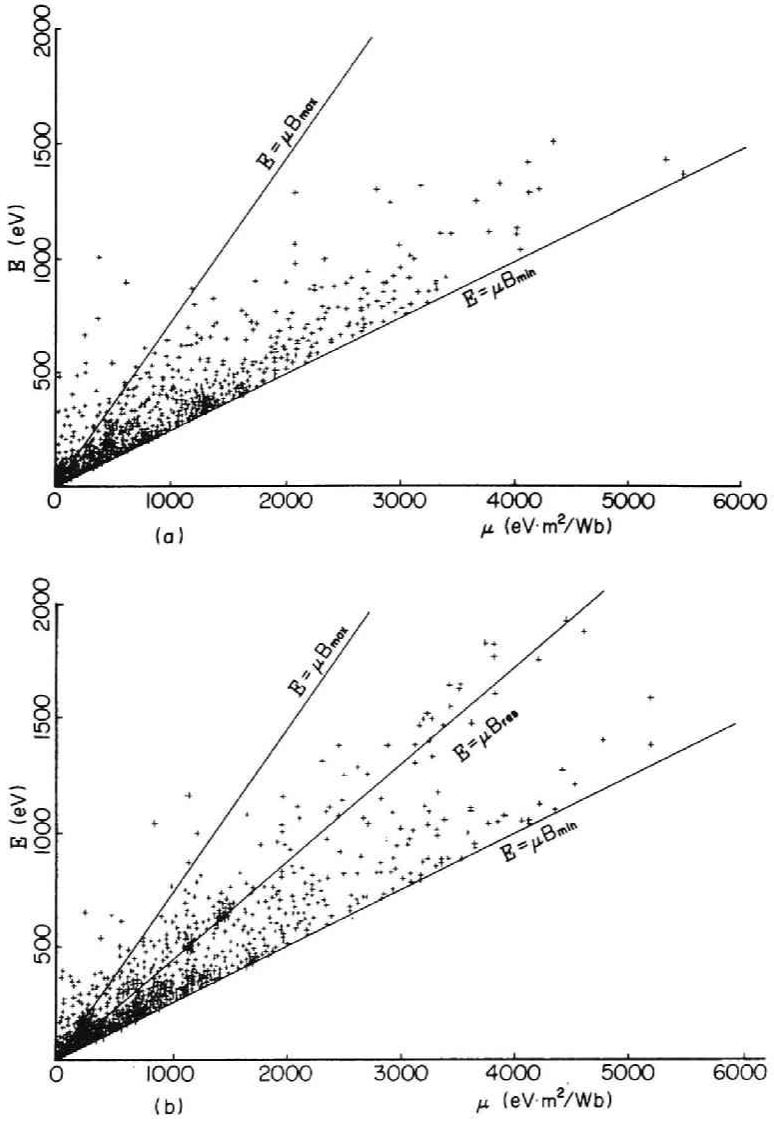

Fig. 5.8 Particle distributions in (ϵ, μ) space at the time $9\,\mu\,sec$ (a) : Without the r. f. electric field - - - Particles are found in a loss cone $(\epsilon \geqq \mu B_{res})$ as a result of collision (b) : With the r. f. electrif field - - - High energy particles are distributed along the resonance line $(\epsilon = \mu B_{res})$.

are shown in Fig. 5.7. In Fig. 5.8, the ion distribution in ($\epsilon = M(v_\perp^2 + v_\parallel^2)/2$, $\mu = Mv_\perp^2/2B$) space at the time $9\,\mu\,sec$ is illustrated by a sign +, showing that considerable number of ions exist even in the loss cone region in the quasi-equilibrium state. Moreover, the distribution function $f_\perp(v_\perp^2)$ does not show the negative gradient peculiar to the mirror systems. These are understood to be caused by the collision of the large angle scattering introduced effectively.

5.3–4 Density profiles and equipotentials

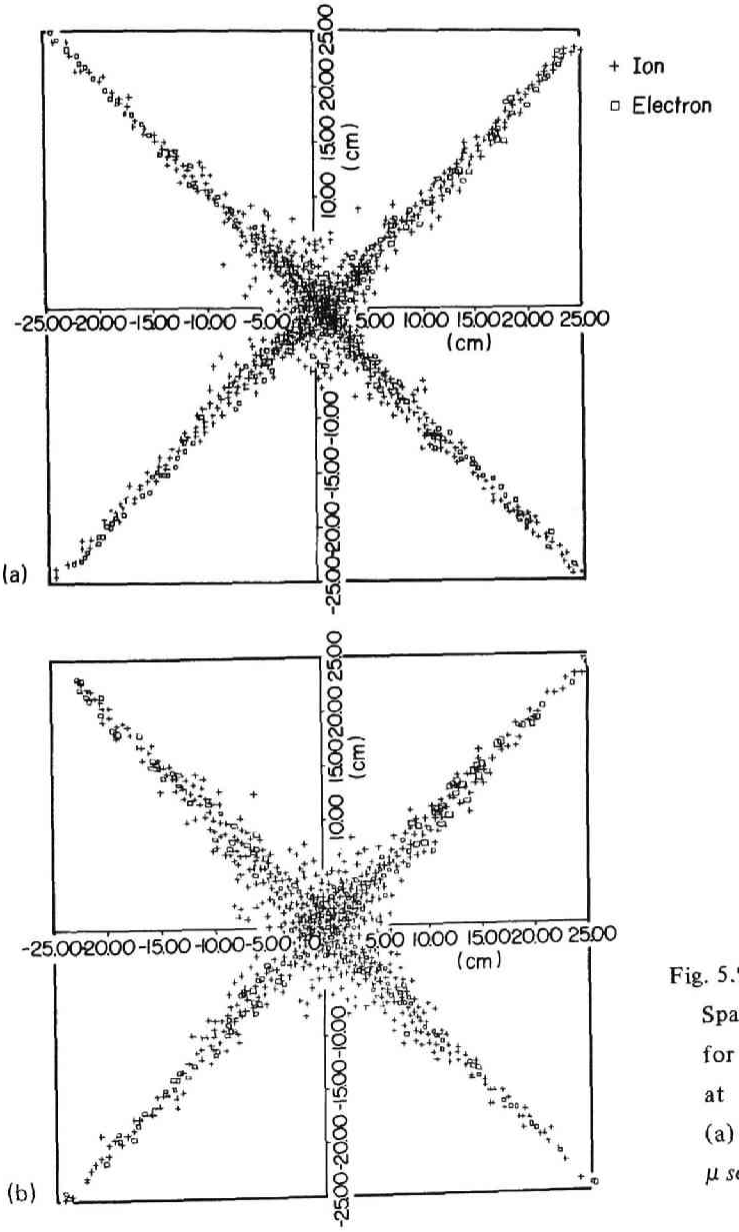

Fig. 5.9
Spatial distributions for ions and electrons at the time $3\,\mu\,sec$ (a) and the time $12\,\mu\,sec$ (b).

The space distribution of the particles at time $3\,\mu\,sec$ shows that the plasma diffuses along the lines of force and forms an equilibrium state. The numbers of ions and electrons are almost equal at each grid even near the wall. At the time $12\,\mu\,sec$, ions are diffused across the lines of force as is explained by the effects of the collisions, and the cloud of ion appears to surround the electron core. Corresponding to the cusp-shaped distribution of the

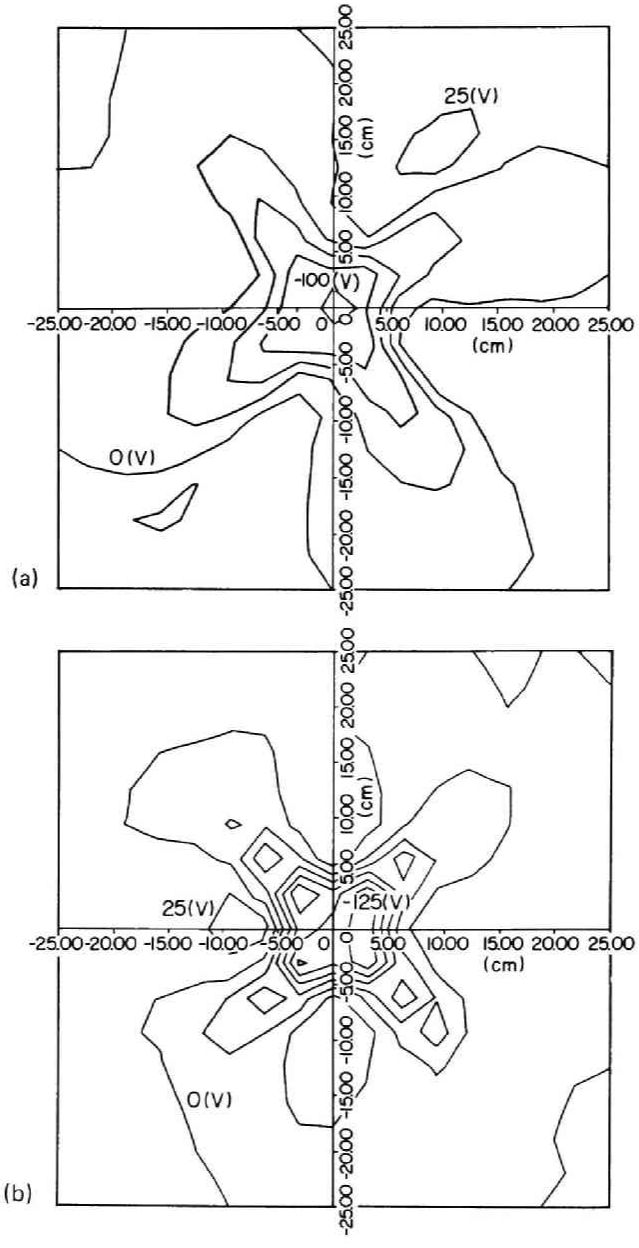

Fig. 5.10 Equipotential contours at the times (a) $3\,\mu\,sec$ and $12\,\mu\,sec$ (b).

plasma, equipotential surfaces enclose the minor axis of the toroidal container and at the time *12 μ sec* the deep valley of the potential grows due to the cross field diffusion, although ions remain more than electrons in the container. It must be emphasized here that the toroidal effects, which are important in usual toroidal closed systems, appear scarcely in these equipotential surfaces or density porfiles.

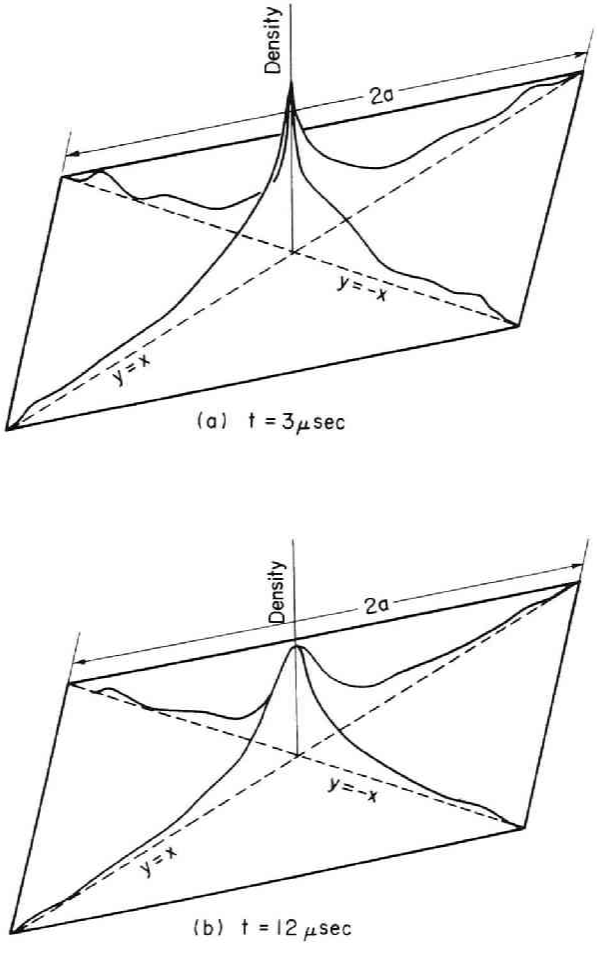

Fig. 5.11 Density profiles at the times *3 μ sec* (a) and *12 μ sec* (b).

5.3–5 Test particles

In order to understand properties of the plasma related to heating and the improvement of confinement especially by means of the r. f. electric field, it is useful to see typical behaviors of some test particles, selected from the simulated plasma.

Usually a particle falls into the loss cone by the collisions and is lost to the wall directly in the cases of the no r. f. electric fields or usual magnetic mirrors. In the case that the r. f. electric field is turned on, however, the situation is somewhat different.

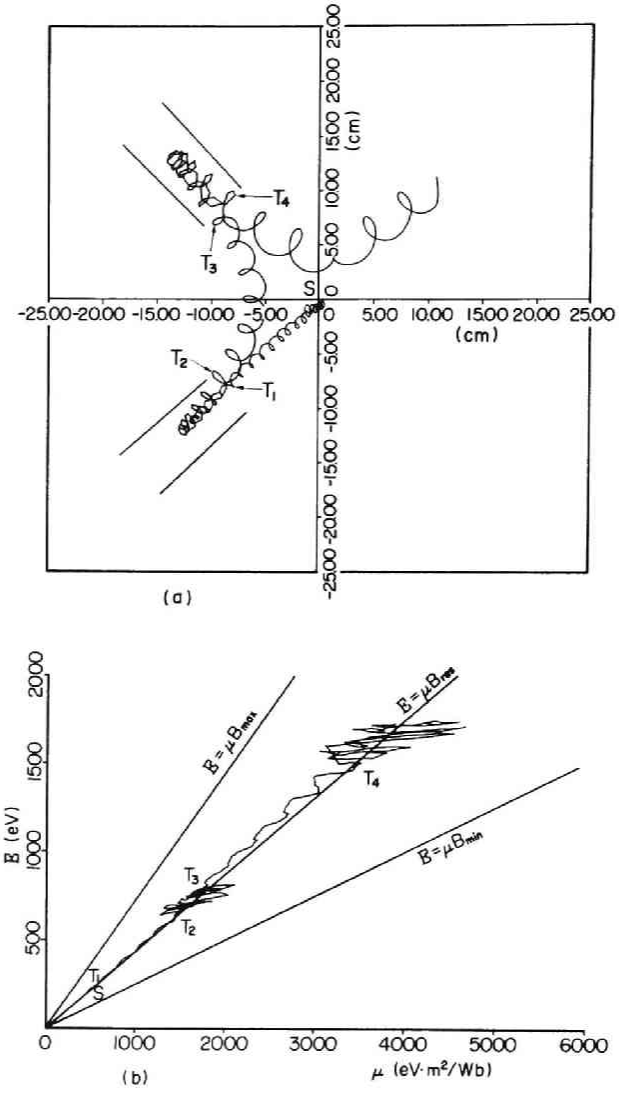

Fig. 5.12 Orbits of a test particle A in real space (a) and in (ϵ, μ) space (b). The point S is the starting point. The points T_1, T_2, T_3, and T_4 correspond to the time at which the particle enters or gets off the resonance zone.

These typical behaviors can be seen in the motions of the particles A and B. Particle A exists in the trapped region in (ϵ, μ) space and experiences the r. f. electric field on the way to and from its turning points in the mirror. Since the r. f. electric field is initially out of phase to the Larmor motion, the particle loses its energy and magnetic moment rapidly. Then the particle recovers its energy and magnetic moment before it escapes from the region,

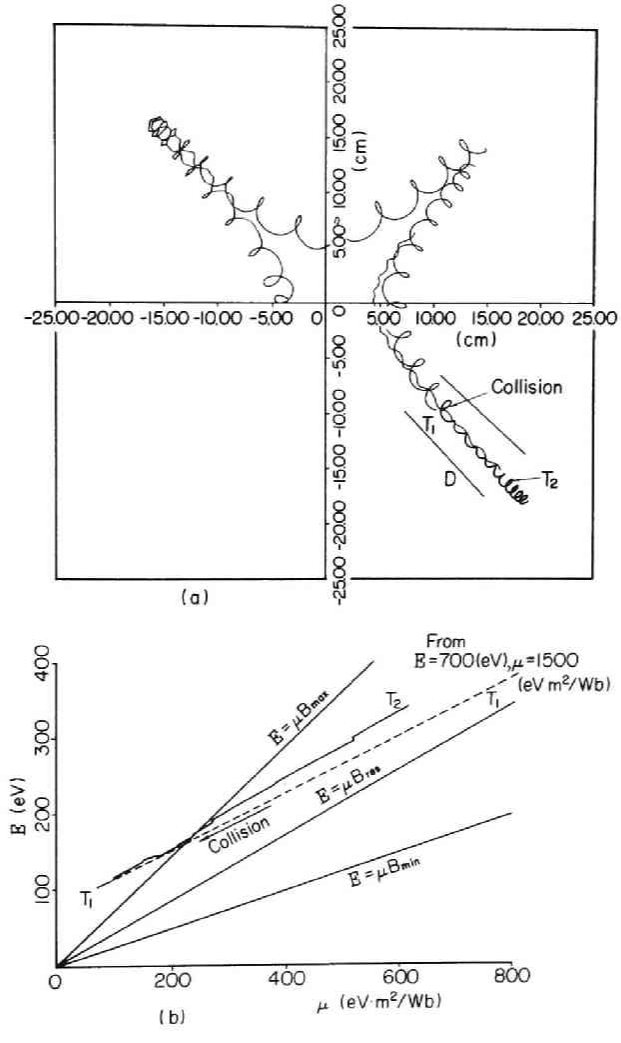

Fig. 5.13 Orbits of test particle B in real space (a) and in (ϵ, μ) space. At the time T_1, a collision takes place and the particle falls into the loss cone. Until the time T_2 at which the particle gets off the resonance region, it is accelerated along the resonance line and re-enters a trapped region.

where the r. f. electric field is applied. Even in the region of no r. f. electric field, it is observed that the magnetic moment is not necessarily conserved, because of the circumstance that the Larmor radius is not so small compared with the characteristic length of the magnetic field.

Test particle B falls into the loss cone by a collision as soon as it enters a region of the r. f. electric field. Then it increases its energy and magnetic moment so that, before it reaches the wall, it re-enters into the trapped region on the (ϵ, μ) space. This particle demonstrates the typical feature of improvement of the confinement associated with the application of the r. f. electric field. Namely, the physical mechanism of the improvement of the confinement is explained in the following: the increments of the energy $\Delta\epsilon$ and the magnetic moment $\Delta\mu$ due to the r. f. electric field are given by

$$\Delta\epsilon = \Delta\mu \cdot B_{res} , \tag{5.15}$$

where B_{res} is defined by $B = M\omega_r/e$, which has been predicted by an analysis [7]. If the value B_{res} is set smaller than B_{max}, the applied r. f. electric field forces the particle to go back to the trapped region.

5.4 DISCUSSIONS OF THE RESULTS OBTAINED BY THE USE OF THE MODEL A

In this section, we summarize the results of the runs simulated by the use of the model A and point out the some problems relating to this model.

The computer simulations related to the collisional diffusion of plasma in the 'Open Ended Toroidal Quadrupole' and the improvements of the plasma confinement by the r. f. electric field have been demonstrated, and its mechanism is clarified in Section 5.3. The diffusion of plasma can be understood as the ambipolar diffusion in a simple mirror device. Therefore, the decay time of the plasma is determined by the collisions acting on ions. The collision, which is introduced as a simple model in the model A, corresponds to the large angle scattering. This model can hold the essence of the collision for the ambipolar diffusions, especially in the case of no r. f. electric field. Accordingly, the results of the simulation show that the decay time of the plasma is consistent with the value calculated simply.

Next the effect of the r. f. electric field has been discussed with respect to the particle decay time and the energy containment time. They are impoved to a certain degree and the ion temperature is observed to rise drastically. The mechanism by which the r. f. electric field heats and confines the plasma efficiently is clarified by the traces of the phase space

orbits of the test particles.

The model A is very simple and convenient to see the effects of the collisions and the r. f. electric fields separately by the observations of the phase space orbits of the test particles. It can simulate the ambipolar diffusion in the mirror devices, also. Because the improvement of the energy containment time obtained by the use of the r. f. electric field is not so clear (the improvement of about 10 %), however, it is required to give evidence of improvement in the more elaborate model again.

5.5 IMPROVEMENTS OF THE MODEL

In this section, we simply explain the improvements of the model which are made in the model B.

5.5–1 A collision model on the basis of the Langevin equation

Concerning the collisions in the usual laboratory plasmas, the contributions of remote interactions are sufficiently large as compared with that due to near interactions, because of the long-range nature of the Coulomb force, which falls off approximately as r^{-2} (r : the separation of a pair of particles) [8, 9]. The nature of the small-angle scattering of the Coulomb collision can be approximated by the Langevin equation [10]. In order to conserve the total momentum and energy, we modify the Langevin equation and obtain an equation of motion. We call it the modified Langevin equation. Namely, the ith particle of species α is interacted with the particles of species j as follows;

$$\frac{dv_i}{dt} = -\sum_j \beta_{\alpha j}(v_i - \bar{v}_j) + \sum_j A_{i\alpha j}\,, \tag{5.16}$$

where $\bar{v}$ denotes the ensemble mean of v, $\beta_{\alpha j}$ is the friction coefficient, and $A_{i\alpha j}$ is the temporally-fluctuated random force whose ensemble mean vanishes.

The friction coefficient $\beta_{\alpha j}$ and the random force $A_{i\alpha j}$ are determined from the various plasma parameters such as the densities, temperatures, collision time, and so on, and the conservation laws of the total momentum and energy, as explained in Reference 11. Then, the distribution function f_α of species α which is governed by the modified Langevin equation satisfies the following Fokker-Planck equation,

$$\frac{\partial f_\alpha}{\partial t} = \frac{\partial}{\partial v}\left[-\sum_j \beta_{\alpha j}(v - \bar{v}_j) f_\alpha\right] + \frac{\partial^2}{\partial v^2}\left[D_\alpha f_\alpha\right]\,, \tag{5.17}$$

where

$$D = \begin{Bmatrix} D_{\perp} & 0 \\ 0 & D_{\parallel} \end{Bmatrix} = \frac{1}{2} \int_{-\infty}^{+\infty} \overline{A(t)\, A(t+\tau)}\, d\tau \,. \tag{5.18}$$

Namely, the modified Langevin equation (5.16) well represents the nature of the small-angle scattering of the Coulomb collision. Computationally, Eq. (5.16) is integrated by a difference equation [11].

5.5–2 A model of the r. f. electrode

The configurations of the r. f. electric field of the model A are rather artificial, although it is simple computationally. In the model B, we simulate the condenser electrodes, which are used actually in the laboratory experiments [1]. Namely, it is assumed that the charge $\pm\ Q \sin \omega_r t$ is supplied compulsorily at the positions which correspond to those of pairs of the r. f. electrodes, where ω_r is the ion cyclotron resonance frequency and Q is the charge required to produce the necessary r. f. electric field. Namely, it is equivalent to that the condenser electrodes are drived by the external circuits.

5.5–3 Feedback control of the r. f. electric field

The r. f. electric field is favourable to heat up the plasma and to suppress the end losses. If the r. f. electric field is set too strong, however, ions are ready to be separated into two groups; one consists of a few high energy ions and the other of the majority of ions with low energy [12]. When the Larmor radii of the high energy ions become too large for their adiabatic moments to be conserved, they escape the container easily. In addition, the energy associated with the relatively small number of high energy ions is comparable to that with the lower energy ions. This causes the spoilage of the energy containment time. On the contrary, the effect of the r. f. plugging cannot be expected if the r. f. electric field is too weak compared with the ion energy. Therefore, the optimum magnitude of the electric field for the r. f. plugging should depend on the ion energy. This fact suggests that we can reduce the total energy loss of the plasma, if we set the r. f. electric field stronger as the ion temperature rises (Feedback control of the r. f. electirc field).

Takizuka, Abe, Momota, and Namba [12] study this feedback control of the magnitude of the r. f. electric field empirically and theoretically, and propose the following:

$$E_0^2 = C \cdot < W_i >, \tag{5.19}$$

where E_0 is the magnitude of the r. f. electric field at the point of the ion cyclotron resonance point, C is a feedback coefficient, and $< W_i >$ is the mean ion kinetic energy.

5.6 SIMULATION RESULTS OBTAINED BY THE USE OF THE MODEL B

The parameters employed in the simulations using the model B are chosen on the basis of the results of Reference [12], and are listed in Table 5.3. The mirror ratio is taken to be 3 so that the adiabatic moment of ion is well conserved. The feedback is performed by choosing the feedback coefficient of Eq. (5.19) as $C = 1.5 \times 10^5\ (V/m)^2/eV$, and the choice of quantities for the computations is shown in Table 5.4.

TABLE 5.3

B_{max}	=	11250 Gauss
B_{min}	=	3750 Gauss
R	=	2.5 m
a	=	0.25 m
C	=	$1.5 \times 10^5\ (V/m)^2/eV$
ω_r	=	6.8×10^7 rad/sec
M	=	1.67×10^{-27} Kg
$T_{i \cdot ini}$	=	300 eV (Maxwellian)
$T_{e \cdot ini}$	=	300 eV (maxwellian)
initial density	=	$1.6 \times 10^{14}\ m^{-3}$
τ_{ic}	=	$12\ \mu$ sec

TABLE 5.4

line density of super particles	=	$1.7 \times 10^9\ m^{-1}$
mass ratio of an ion to an electron	=	25
initial number of super ions and electrons	=	1500, respectively

In order to avoid effects which may be due to the initialization of the charged particle system as is done in the simulations using the model A, the r. f. electric field is not applied for the first $3\,\mu sec$, and is then applied until the time $t = 18\,\mu sec$ (Experiment 1). For comparison of the results, other computer experiments have been carried out for two cases: in Experiment 2, the r. f. electric field is absent throughout the experiment, and in Experiment 3, the r. f. electric field is turned off at time $t = 12\,\mu sec$.

The improvement in the particle containment time is seen in Fig. 5.14. Between the time $t = 3\,\mu sec$ and $t = 12\,\mu sec$, the particle containment time in Experiment 2 is $\tau_{n2} = 35\,\mu sec$, while in Experiment 1 the r. f. electric field increases τ_{n1} to $39\,\mu sec$. Similarly, between the time $t = 12\,\mu sec$ and $t = 18\,\mu sec$, $\tau_{n1} = 35\,\mu sec$ should be compared with the containment time in Experiment 3, *i. e.*, τ_{n3} $31\,\mu sec$. Provided that the mirror ratio R_m is replaced by the effeictive one [13]:

$$R_{m\,eff} = R_m / (1 + e\bar{\phi} / < W_i >) . \tag{5.20}$$

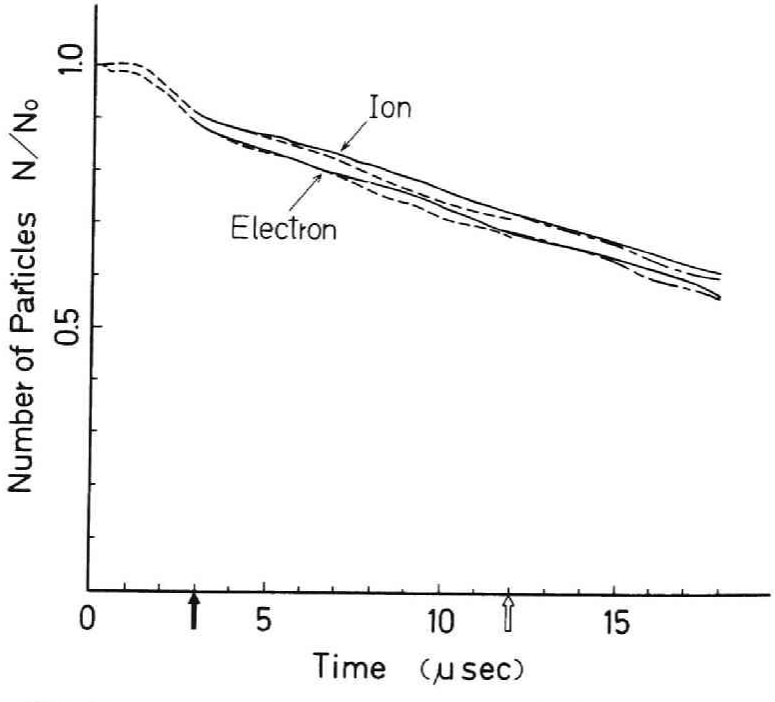

Fig. 5.14 Decay curves of ions and electrons. In Experiment 1 (solid curve), the r. f. electric field is applied from the time $t = 3\,\mu sec$ till the time $t = 18\,\mu sec$. In Experiment 2 (dashed curve), no r. f. electric field is applied, and in Experiment 3 (chained curve), the r. f. electric field is turned off at the time $t = 12\,\mu sec$.

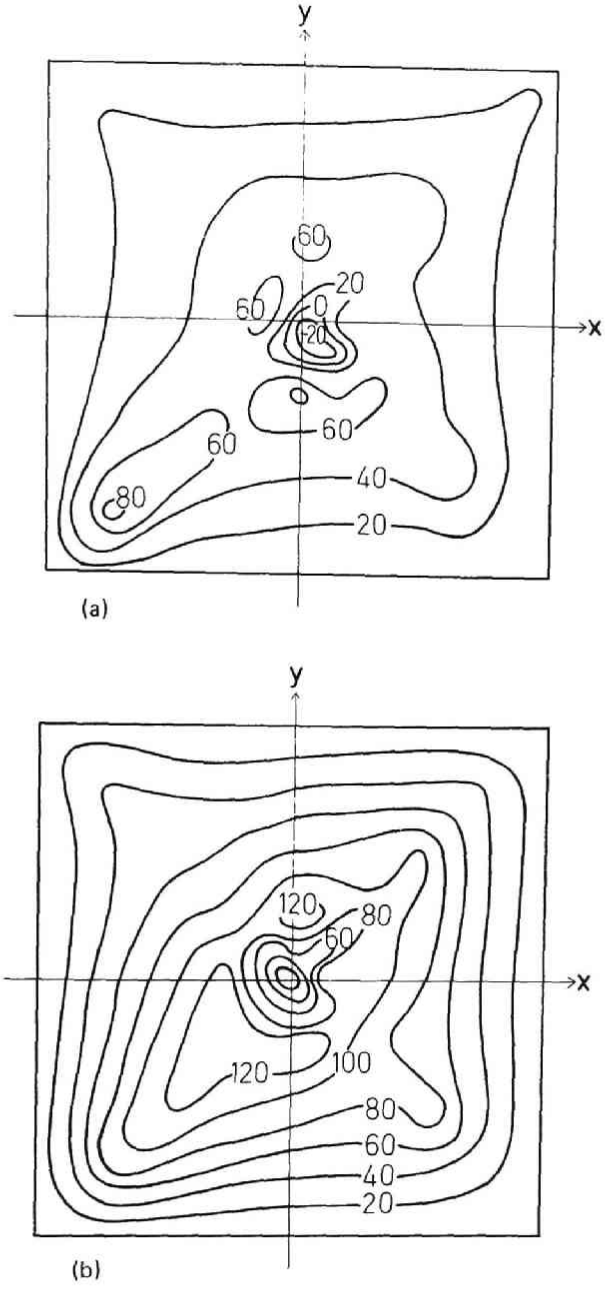

Fig. 5.15 Equipotential contours in Experiment 2 (a) and in Experiment 1 (b) at the time $t = 9\,\mu sec$. The outer square is the wall of the container, and the equipotential contours are drawn at intervals of $20\ V$.

where $\bar{\phi}$ represents the mean plasma potential, the values of τ_{n2} and τ_{n3} obtained in the computer simulations coincide with the value obtained in Reference [12]:

$$\tau_n \simeq \tau_{ic} \ln R_m + 2R_m \langle \tau_{it} \rangle , \tag{5.21}$$

where $\langle \tau_{it} \rangle$ is the mean transit time of ions. The spatial distributions of the plasma potential in Experiments 2 and 1 at the time $t = 9\,\mu sec$ are illustrated in Figs. 5.15 (a) and (b), respectively.

The evolution of the contained energy of the plasma and that of the lost energy are demonstrated in Fig. 5.16, where the contained energy consists of the kinetic energy and the potential energy of both ions and electrons.

As well as the particle confinement, a careful application of the r. f. electric field causes about a certain improvement in the energy confinement. In fact, the energy containment time τ_{E1} is $47\,\mu sec$ for the first $9\,\mu sec$ or $41\,\mu sec$ for the last $6\,\mu sec$, in Experiment 1. These values must be compared with $\tau_{E2} = 43\,\mu sec$ (Experiment 2) or $\tau_{E3} = 37\,\mu sec$ (Experiment 3), respectively. Therefore, in the case, the r. f. electric field improves the energy confinement by about 10 %.

The r. f. electric field may rise the ion energy. As is shown in Fig. 5.17 (a), the mean

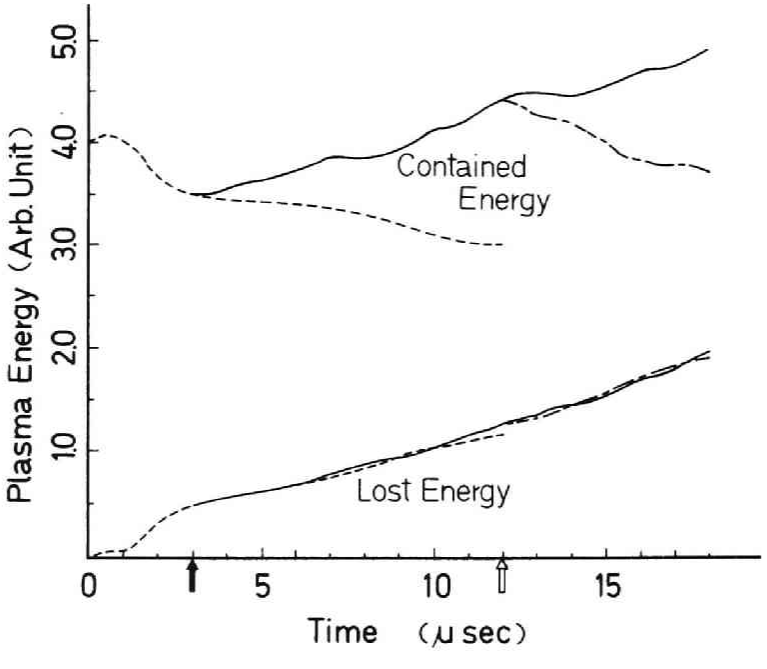

Fig. 5.16 Evolution of the contained plasma energy and the lost plasma energy in Experiments 1, 2, and 3.

ion energy increases by a factor 3 for a time interval of $15\,\mu sec$. The heating rate is observed to be $\tau_H^{-1} = 8.3 \times 10^4 /sec$ in the Experiment 1. On the contrary, the electron temperature is not affected by the r. f. electric field as shown in Fig. 5.17 (b).

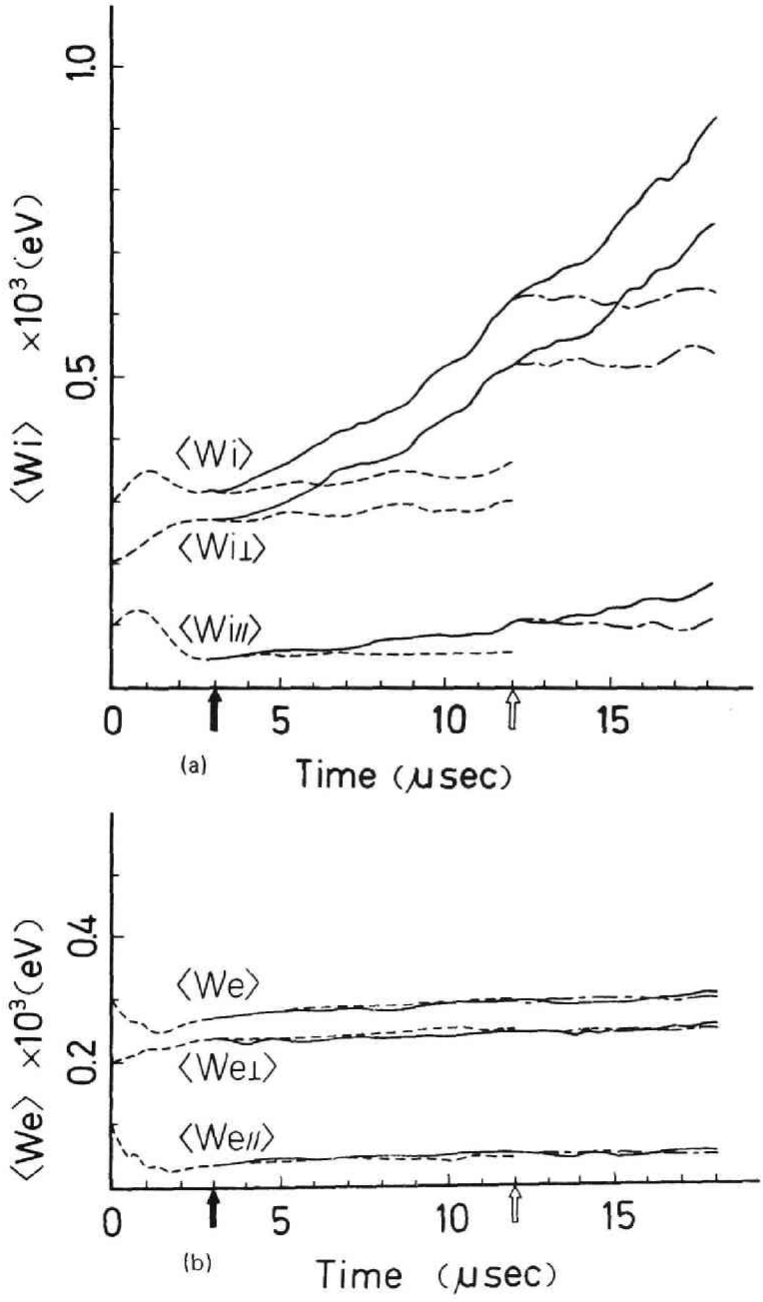

Fig. 5.17 Time evolutions of the mean ion energy (a) and the mean electron energy (b) in Experiments 1, 2, and 3.

5.7 CONCLUSIONS AND DISCUSSIONS CONCERNING THE RESULTS OBTAINED BY THE USE OF THE MODEL B

Computer experiments using the model B have been carried out with optimized parameters in the toroidal quadrupole. The plasma has been readily heated and an improvement in the energy containment time of 10 % is obtained.

In these computer experiments assuming the axis-symmetry, some instabilities have been inhibited, and the effective collision time has been restricted by computer time to a value only a few times greater than the mean transit time of ions. This situation has probably caused favourable results in the improvement in the energy confinement by the applied r. f. electric field. For instance, the absence of instabilities which may be associated with the r. f. electric field prevents anomalous losses, and a number of collisions may restrain ions from being separated into two groups by the r. f. electric field.

REFERENCES

1. S. Miyake, T. Sato, K. Takayama, T. Watari, S. Hiroe, T. Watanabe, and K. Husimi: J. Phys. Soc. Japan 31 (1971) 265.
2. R. W. Moir: Center d'Etude Nucleaires, Paris, Euratom Report EUR-CEA-FC 496 (1968).
3. R. W. Hockney: Phys. Fluids 9 (1966) 1826.
4. B. Alder, S. Fernbach, and M. Rotenberg: *"Methods in Computational Physics"* Academic Press, New York and London (1970).
5. C. G. Smith and A. S. Bishop: *"Conference on Plasma Physics and Controlled Thermonuclear Fusion Research"* Novosibirsk (1968) CN-24/D-9.
6. A. Ralston: *"A First Course in Numerical Analysis"* McGraw-Hill, New York and London (1965)
7. T. Kawamura, H. Momota, C. Namba and Y. Terashima: Nuclear Fusion 11 (1971) 339.
8. B. A. Trubnikov: in *"Reviews of Plasma Physics"* Vol. 1, edited by A. M. A. Leontvich, Consultant Bureau, New York (1965).
9. S. Ichimaru: in *"Basic Principles of Plasma Physics"* W. A. Benjamin, Inc., Massachusetts (1973).

10. S. Chandrasekhar: *"Reviews of Modern Physics"* Vol. 15, Dover, New York (1954).
11. T. Takizuka: Master thesis, University of Kyoto (in Japanese) (1972)
12. T. Takizuka, H. Abe, H. Momota, and C. Namba: Plasma Phys. 17 (1975) 887.
13. D. J. Ben Daniel: J. Nucl. Energy, Pt. C3 (1961) 235.

CHAPTER 6

CONCLUSION

In this thesis, we have studied the physical and computational properties of the finite-sized particle model in the plasma simulations both theoretically and experimentally, and on the basis of the acquired knowledge we have applied the finite-sized particle simulation to a couple of investigations concerning the devices for the plasma containment. We present a summarization of each chapter in the following.

In Chapter 2, we have analyzed the differences, of the collisional effects of the finite-sized particles (clouds) between the single-species plasma and two-species plasma by invoking the Balescu-Gurnsey-Lenard kinetic equation and modifying it to a form like the Landau equation. In order to velocity-dependent collisional effects on a test cloud, we have expressed them in terms of a quantity which is reduced to the Coulomb logarithm in the case of the usual point-particle plasma, and compared them with those of the electron cloud plasma. The calculation for the cloud with the radius equal to or larger than the Debye length has shown the following properties different from those of the electron cloud plasma: (1) the shielding effect of ion on the fluctuating electric field reduces the collisional effect for the test cloud with the velocity smaller than the ion thermal velocity and (2) the emission of the ion sound wave remarkably increases the collisional effect for the test cloud with the ion sound wave velocity in the moderately nonisothermal plasma.

In Chapter 3, we have examined the effects of spatial grids, of which use is inevitable from the computational point of view in the simulation using the present electronic digital computers, and estimated the error of the conserved quantities such as the total energy and the total momentum both theoretically and experimentally. We have analyzed the properties of the temporal fluctuation of total energy, K_g, in the usual models which calculate the total momentum conserved. The results have given an evidence that the fluctuation of total energy is characterized by two quantities: the standard deviation of K_g in t, $\sigma\{K_g\}$, and the correla-

tion time of $dK_g/K \cdot dt$, τ_c, about periodic one-dimensional systems, where K is the kinetic energy in the system. As for the former $\sigma\{K_g\}$, We have evalutated it by invoking the stochastic theory and obtained a scaling law:

$$\sigma\{K_g\}/K \simeq \sqrt{2/\pi} \cdot \eta \cdot \{\sqrt{2M}\, n_s \lambda_D\}^{-1} \sqrt{t\, \tau_c\, \omega_p^2}$$

where $2M$ is the number of the grids per one period, n_s is the electron density, λ_D is the Debye length, and ω_p is the plasma angular frequency. The coefficient η depends on the magnitude of the unphysical grid force of each model. Our simulations using the usual models (CIC-PIC, modified SUDS, and method 2/2) supported this scaling law. As for the latter or the correlation time τ_c, we have studied it empirically. It has been found that $\tau_c \simeq \Delta t$ if Δt is sufficiently large, and $\tau_c \simeq 1/4\ \Delta/v_{th}$ if $\Delta/(\Delta t \cdot v_{th}) > 3$, where Δt is the time step, Δ is the grid distance, and v_{th} is the thermal velocity of the electron.

In Chapter 4, we performed the simulation of the HIPAC as an application of the particle simulation. Namely, the quiescent confinement of non-neutral electron clouds in a toroidal magnetic field was confirmed by the computer simulation using the finite-sized particle model. In the uniform density, we obtained 0.08 as the maximum of the ratio $q\,(\omega_p^2/\omega_c^2)$. This value is larger by a factor of 4 than that achieved in the experiments and reasonable, judging from the theoretical and experimental evidences. The stable dioctron modes, of which amplitudes could be controlled by the initial conditions, were observed to spoil the confinement time. Various physical quantities such as electrostatic potentials, decay times, and kinetic temperatures, which were not measured in the experiments, have been calculated and compared with the equilibrium theory.

In Chapter 5, Collisional diffusions of plasma contained in an open-ended toroidal quadrupole magnetic field and improvement of an energy confinement with the aid of applying the r. f. electric field were simulated by the use of the PIC model equivalent to the CIC model. The plasma decreased at the rate which was estimated from the magnitude of the collisions acting on the ion. The improvement of an energy confinement time by applying the r. f. electric fields has been suggested especially by the observation of the phase-space orbits of some test particles which are difficult to observe in experiments. A typical result of the run with optimized parameters has indicated that the plasma can be heated easily and an improvement in the energy confinement time of about 10% can be achieved.

Next, we mention the problems left in this thesis and the future developments of author's investigations in the following:

As pointed out in Chapter 2, it is a problem that the velocity dependences of the finite-sized particles are different from those of the point particles. In the simulations in which the collisional effects influence the phenomena, we need use a collision model such as the Monte-Carlo method from the computational point of view rather than rely upon the collisional effects inherent in the finite-sized particle model. As one of these models, the collisional model which was governed by the Langevin equation was used in Chapter 5. This model can express the collisional effects peculiar to the Coulomb collision or the small angle scattering, and not only so-called "like-particle collision" but the interspecies collision. Although this model was satisfactory concerning the problems of Chapter 5, however, this model had a defect that the pitch angle scattering was independent of the velocity of the particle. Therefore, the author and his coworker have attempted to improve the collision model and almost achieved a complete model, which can express the whole properties of the Coulomb collision.

In the analyses concerning the accuracy of the conservation of total energy which are presented in Chapter 3, we have treated the simplest case or the periodic, one-dimensional electrostatic case as a test problem. In the 2- or 3-dimensional case, however, the straightforward extensions of the one dimensional case are applicable. Our basic considerations and mathematical techniques which we have applied to the simplest case would be applicable even to the more complex case or the electromagnetic case, in which the full Maxwell equation is solved.

We assumed the axis-symmetry and restricted the variation of the electrostatic field to two-dimensional one in the circular and rectangular cross-sectional toroidal vessels used in Chapters 4 and 5, respectively. The reason was that the CPU time and memory size of the computers which could be used in these works had been severely limited. From the computational point of view, the extensions to the 3-dimensional cases are straightforward. When we can use a large-scale computer which can afford to supply a sufficient memory and CPU time, we will apply the 3-dimensional programs to the various physical problems, for example, anomalous heating by the waves, anomalous diffusions by the spontaneously fluctuations in the closed confinement systems of plasmas, and so on.

ACKNOWLEDGEMENT

The author wishes to express his appreciation to Professor Ryohei Itatani of Kyoto University for his advice and encouragement during the course of this research, and for his constructive criticism during the preparation of this manuscript.

Detailed discussions with Dr. Hiromu Momota of Kyoto University and his valuable suggestions in the study summarized in Chapter 5 are gratefully acknowledged.

It is a pleasure to thank Mr. Tomonori Takizuka of Japan Atomic Energy Research Institute, Mr. Chusei Namba of Institute of Plasma Physics in Nagoya University, Mr. Hiroshi Naitou of Institute of Plasma Physics in Nagoya University, Mr. Junichi Miyamoto of Toshiba Co., Ltd., Mr. Kazuhiro Kawai of Mitsubishi Co., Ltd., and Mr. Teruhiko Yamada of Nippon Electric Co., Ltd. for their cooperations in the work.

The author also wishes to thank his colleagues, especially to Mr. Osamu Fukumasa, Mr. Yasuyoshi Yasaka, Mr. Makoto Kubo, Mr. Yukihiro Tomita, Mr. Tetsuya Akitsu, and Mr. Atsushi Fukuyama for their discussions on the computer simulation, plasma physics, and the controlled thermonuclear fusion research.

Use has been made of the electronic computers FACOM 230-75 at Kyoto University and HITAC 8500 at Institute of Plasma Physics in Nagoya University.

PUBLICATIONS CONCERNING THIS THESIS

CHAPTER 2

"The Properties of Collision in the Plasma Composed of the Finite-Sized Particles of 2-Species", H. Abe, H. Naitou, and R. Itatani; to be published in J. Phys. Soc. Japan.

CHAPTER 3

"Grid Effects on the Plasma Simulation by the Finite-Sized Particle", H. Abe, J. Miyamoto, and R. Itatani; J. Computational Phys. 19 (1975) 134–149.

CHAPTER 4

"Computer Simulation of Containment of Electron Clouds in a Toroidal Magnetic Field", H. Abe; to be published in Plasma Phys.

CHAPTER 5

"Computer Simulation of RF-Confinement of Plasmas in an Open-Ended Toroidal Quadrupole", H. Abe, K. Kawai, T. Yamada, and R. Itatani; J. Phys. Soc. Japan 33 (1972) 216–224.

"Ion Cyclotron Heating and Energy Confinement of Plasma in a Toroidal Quadrupole", T. Takizuka, H. Abe, H. Momota, and C. Namba; Plasma Phys. 17 (1975) 887–904.